The Impact of Galaxy Cluster Growth on Ram Pressure Stripping

Ana Carolina Costa Lourenço

Supervisor: Dr. Patrícia Arévalo (UV)
Co-supervisor: Dr. Yara Lorena Jaffé Ribbi (UV/USM)
Internal reviewer: Dr. Patricia Arévalo (UV)
External reviewer: Dr. Emanuela Pompei (ESO)

Tesis para optar al grado de Doctor en Astrofísica
Instituto de Física y Astronomía
Facultad de Ciencias
Universidad de Valparaíso

August 2024
Valparaíso, Chile.

To my family, friends, teachers, professors, and greedy galaxy clusters that keep merging and growing until the present day.

The eternal beauty

Beauty belongs to no one,
Renews itself with generations.
Results from an eternal sum,
Comes and goes on all the stations.

And the true eternity
Is not limited to an eternal being.
It's a lineage of fraternal feeling,
That renews in maternity.

Even the unicellular entity,
Inhabitant of abyssal dark.
With another idea of good and evil's mark,
Continues to perpetuate silently.

And so beauty revives,
Helically in genetics.
Synaptically in memetics,
Not in the body I once carved.

Even galaxies age,
They evaporate. They are strangled.
They are harassed, and they are mangled,
Blue spirals turn into a reddened cage.

The worm that will eat me one day,
Will fertilize the land where it will lie.
The sun that stars in the evening sky,
Marks the day of all's decay.

So without glory, I am content,
Like the sun reflected in the stream.
Piercing it without a dream,
Just like the wind's attacks at this moment.

Ana C. C. Lourenço

This thesis is solely my own composition,
except where specifically indicated in the text.

Ana Carolina Costa Lourenço
August 2024
Valparaíso, Chile.

Acknowledgements

First and foremost, I would like to express my sincere gratitude to my supervisor, Dr. Yara Jaffé, for her patient guidance and thoughtful dedication. I also want to give my deepest appreciation to Dr. Emanuela Pompei for her guidance during my ESO studentship and for constantly pushing me to follow my academic aspirations. Equally important, I would like to thank all the professors who were part of my academic path in João Pessoa, Winnipeg, Rio de Janeiro and Valparaíso.

I thank Agencia Nacional de Investigación y Desarollo (ANID), the European Southern Observatory (ESO), and Centro de Astrofísica e Tecnologias Afines (CATA) for their financial support. Thank the GASP collaboration for their valuable contribution to my PhD thesis. A special thanks to Dr. Bianca Poggianti for being so welcoming and partially funding a three-month science visit to INAF-Padova. Also, thanks to Dr. Benedetta Vulcani for all the feedback she gave to my work and for sharing her office with me. Many thanks to Alessandro Ignesti for all the help with the X-ray data reduction and to Ariel Werle for sheltering me in my first two weeks in Padova. I want to highlight some truly exceptional people from our Valpo jellyfish group. A thousand thanks to Jacob Crosset, Kshitja Kelkar, Lawrence Bilton, and Diego Pallero for their precious input on my work and time spent with board games and beers. Also, thanks to Franco and Vicente for sharing interesting plots and codes with me.

In addition, I would like to mention Mona and Mohsen Fathi for their valuable friendship and for introducing me to Persian cuisine and culture. I would also like to extend my thanks to all my former colleagues from Valpo who spent many hours studying for exams with me late at the university and sometimes even on the weekends: Greco Peña, Martin Solar, Santiago Bernal, and Elena Lopez. I also thank the ones who used to go to Roma with me during happy hour: Alejandra, Ramsés, Alex, Javier, and Nicolas.

I want to thank my ESO-Vitacura friends, who were essential to making 2023 the happiest year of my PhD. Special thanks to the two Saras, Yiqing, Akriti, Lea, Eloise, Ksenia, Coté, Timo, Amelia, Elizabeth, Aish, Johanna, Jaime, Ben, Fred, Bibi, Camilo,

Micha, Carla, Leslie, Chiara and Enrico.

I would like to thank my family (especially my mother and father) and everybody who was like a family to me during my stay in Chile. I would like to highlight Fran and my Brazilian friends in Chile: Douglas, Larissa, Thallis, Ana, Pedro, Círia, Priscila, and Dani. Finally, but most importantly, Waldo and his family, Myriam, Carmen, and Alejandro Carvajal. Thank you for all your support and for coping with me in the final part of my doctorate.

Abstract

In a hierarchical Universe, galaxy clusters continue to grow with cosmic time, and thus, many of them are disturbed by the accretion of groups or major collisions with other clusters. Hydrodynamical simulations and a few observational works show that ram-pressure stripping can be boosted up in merging clusters, providing an alternative way of forming jellyfish galaxies. In this work, we classify the dynamical state of the WINGS and OmegaWINGS X-ray selected cluster samples at $z \sim 0.05$ using different proxies from the most diverse wavelengths to investigate how the fractions of ram-pressure stripped galaxies among the spiral population correlate with the cluster "messiness". Our findings show no significant correlation between a cluster's dynamical state or mass and the fraction of jellyfish galaxies. We tentatively create a dynamical state classification system considering dynamic state classification parameters at different wavelengths. When analyzing the results, we found a possible enhancement in interacting clusters. The results regarding the cluster mass are intriguing since, in massive clusters, the higher relative velocity between the ICM and the galaxies in messy environments is also expected to enhance ram pressure. Ram pressure stripping beyond the analysed cluster radius or pre-processing in galaxy groups could impact this result. Our results show that cluster mergers possibly accelerate galaxy evolution through ram pressure enhancement. The amount of recently accreted galaxy groups is not linked to this enhancement since, in substructures, we found a suppressed fraction of galaxies undergoing ram pressure stripping.

Contents

CHAPTER 1

Introduction

Galaxy clusters are over-densities of galaxies that contain dozens to hundreds of galaxies moving in a common gravitational potential well filled with hot gas. Their gravitational field keeps attracting isolated galaxies, galaxy groups, and even other clusters with similar sizes. Collisions between galaxy clusters are thought to be an efficient way of accelerating galaxy evolution. However, conflicting results also show the opposite trend. There is a lack of studies on this topic performed with large samples in a homogeneous way. This thesis aims to reduce this knowledge gap.

The first specific goal of this research is to robustly classify the state of the interaction of a large sample of galaxy clusters with the most diverse techniques in different wavelengths. This sample can be used as a reference for future classification of the interaction level in clusters of galaxies. We then aim to evaluate how the fractions of ram pressure stripping (RPS) candidates vary in clusters with different degrees of interaction. Finally, we aim to understand the importance of RPS in galaxy pre-processing before entering the cluster, in galaxy groups, and in filaments of galaxies that just entered the cluster.

This chapter will introduce the study of galaxy evolution by giving some historical context and then discussing cluster growth and galaxy evolution in dense environments and galaxy cluster substructures. In summary, the impact of cluster growth in ram pressure stripping. We will show the gaps in the current understanding of this problem and our contribution to addressing them robustly.

1.1 From comets to galaxies: The unexpected birth of extragalactic astronomy.

One of the most exciting characteristics of science is serendipity. Important discoveries were often made when scientists were trying to solve other problems not related to their findings. These discoveries, made by chance, often gave notoriety to those who made them. It seems counter-intuitive that science, although strictly following logic and the scientific method, still leaves so much space for luck to act. However, many of these fantastic discoveries would have gone unnoticed if scientists were not critically trained.

In 1730, Charles Messier was born in Badonviller, a small town in the interior of France. When he was 13, he observed "the great comet of 1744". This spectacular object was registered as having six tails in its perihelion and being bright enough to be observed during the daytime. It is a widespread belief that comets bring bad omens. Cheseaux comet, with its beauty, sealed the fate of the young Messier, who would become one of the most excellent comet hunters who had ever lived (Stoyan, 2015; Moore, 2015).

Most comets are not as luminous as the Cheseaux comet. In general, the observation of this type of object depends on instruments such as telescopes and binoculars. Using a 200 mm reflector telescope, Messier discovered 13 comets, co-discovered seven, and observed 44 of the 50 known comets from 1758 to 1805 (Gregersen, 2017; Jakiel, 2019). He often came across objects like clouds that never moved in his observations. Such objects hindered his search for comets, as comets could often be confused with them. Messier then decided to catalogue these irritating objects and similar objects that his contemporaries had already observed. That way, he would not waste more time on fake comets while hunting for real ones.

Messier, serendipitously, discovered nebulae, star clusters, galaxies and even galaxy clusters. His scientific training led him to rigorously catalogue these objects and allow other scientists to study them in greater detail. Unaware of what he was doing, Messier observed 32 extragalactic nebulae in his catalogue and opened countless possibilities for understanding the universe on a large scale (Messier, 1781; Messier & Niles, 1981). Later, John Louis Emil Dreyer created the New General Catalog (NGC) of Nebulae and Clusters of Stars, which contains 7840 objects. It included observations made by the Herschel family (William, Caroline, and John Herschel) and James Dunlop. Two supplements to the NGC, known as the Index Catalogues (IC), were

also published by Dreyer, containing more than 5386 astronomical objects (gen, 1864; Dreyer, 1908; Herschel & Dreyer, 2018; Voller, 2021).

Later, the nebulae in the Messier, NGC, and IC catalogues would attract other astronomers' curiosity. Edwin Hubble worked with a 100-inch Hooker Telescope at Mount Wilson Observatory. He investigated whether the spiral nebulae were inside or outside the Milky Way (Sharov & Novikov, 1993). At that time, there was a fierce debate between Harlow Shapley and Heber Curtis, "the great debate" about the scale of the Universe. Curtis defended the Milky Way as just one ordinary galaxy among many other spiral nebulae that composed the Universe. Shapley was more conservative and believed the spiral nebulae were nearby gas clouds in the Milky Way (Shapley & Curtis, 1921). In 1923, Hubble discovered Cepheid stars, a kind of variable star, in the Andromeda Nebula. A well-defined relation between the period of the fluctuations and the luminosity (Leavitt & Pickering, 1912) of these stars allowed Hubble to determine the distance to these stars and, consequently, to Andromeda. Hubble estimated Andromeda to be around 900,000 light-years away. It is currently known that Andromeda is even further away from us (Hubble, 1926) [1]. This distance was far beyond the proposed borders of the Milky Way at that time. Andromeda was, therefore, a galaxy, not a cluster of stars within the Milky Way. Later, Georges Lemaître, a french catholic priest, caused another paradigm shift when he discovered, through observations, a linear relation between galaxies distances and recession velocities. He was the first to estimate a value to the constant of expansion of the Universe, today known as the Hubble constant (Lemaître, 1927). Alexander Friedmann had already predicted an expanding Universe by solving general relativity equations (Friedmann, 1922). Lemaître went further and proposed that the Universe began with a primordial atom that exploded (Lemaître, 1931). This idea was refined and got contributions from many subsequent cosmologists, and it is currently known as the Big Bang theory. From that moment on, the borders of the known Universe expanded faster and faster in people's minds.

1.2 Galaxy distribution in the large scale

In nature, it is ubiquitous for objects to orbit around each other. The moon orbits around the Earth, and the Earth and the other Solar system planets orbit around the

[1] Hubble mixed different types of Cepheid stars, which led to an underestimation of the distances. (Schneider, 2007)

Sun, which orbits around the galaxy centre with many other stars. When the number of catalogued galaxies expanded, a natural thought would be to wonder if galaxies are also organised by rotating around something else. Alternatively, would galaxies be randomly distributed in the Universe?

Charles Messier and William Herschel already conceived that there are clusters of nebulae (galaxies). They had already noticed an excess of galaxies in the direction of the Virgo constellation and Coma Berenice. Later, George Abell, Fritz Zwicky and other astronomers would catalogue thousands of galaxy clusters (Schneider, 2007).

Massive clusters interconnected by filaments compose the cosmic web. At the centre of these clusters reside the brightest cluster galaxy (BCG), a supermassive elliptical galaxy that grows together with the cluster, merging with smaller galaxies that flow into the cluster through the main filaments (Chu et al., 2021). In Fig. 1.1, we see the large-scale structure composed of the brightest galaxies in the Sloan Digital Sky Survey (SDSS-DR12; Alam et al., 2015), we find the richest clusters in the intersections of the interconnecting galaxy filaments. Between the filaments, there are large voids of up to $\sim 150\,\mathrm{Mpc}$ (di Nella & Sylos Labini, 1997). These regions have a very low galaxy density and account for $\sim 77\%$ of the total volume of the large-scale structure (Cautun et al., 2014). Nearly all galaxies occupy 10% of the volume on large scales (Fraknoi et al., 2016). Satellite galaxies orbit the cluster centre of mass. They come from the most diverse environments. Almost 50% of these galaxies come from the filaments that interconnect the clusters, some of which come in pairs, triplets, or groups of less than 50 members (Cautun et al., 2014; Benavides et al., 2020; Kuchner et al., 2022). Others come from the large voids in the neighbourhood of the clusters. A cluster can also accrete hundreds to thousands of galaxies simultaneously in a major merger event with another cluster (e.g. Stroe et al., 2014).

1.2.1 Galaxy Clusters

Galaxy clusters are the largest systems in the Universe that are gravitationally bound. Hundreds to thousands of galaxies orbit them, tied to their gravitational potential well while evolving due to several physical processes. The velocity dispersion of the cluster galaxies ranges from 500 to 1000 km/s, and their respective masses range from $10^{14} - 10^{15}\,\mathrm{M}_{\odot}$. Moreover, they extend over vast regions of the cosmos, with sizes (radii) between $\sim 2 - 3\,\mathrm{h}^{-1}\,\mathrm{Mpc}$.

The mass of a galaxy cluster is typically expressed within an overdensity radius r_{Δ}

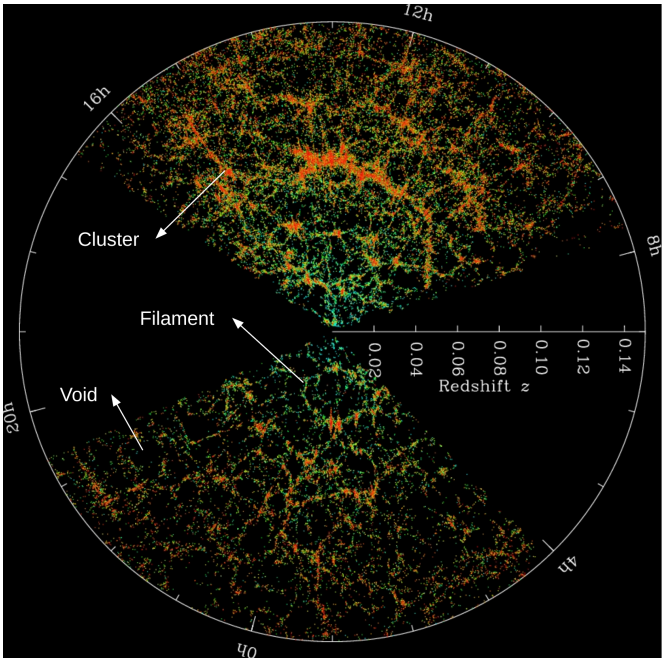

Figure 1.1: The SDSS's map of the Universe. Each dot is a galaxy; the colour is the $g - r$ colour of that galaxy. Image Credit: M. Blanton and SDSS.

as

$$M_\Delta \equiv \frac{4\pi}{3}\Delta\rho_{\rm crit}(z)r_\Delta^3,$$

where $\rho_{\rm crit}(z)$ is the critical density of the universe at the cluster's redshift, and r_Δ is the radius where the mean enclosed density is $\Delta \times \rho_{\rm crit}(z)$. A value of $\Delta = 500$ corresponds to the radius within which *Chandra* and *XMM-Newton* observations can reliably measure the gas density and temperature profiles of the intracluster medium (ICM). The approximate ratio between different radius definitions is $r_{500} : r_{200} = 1 : 1.4$.

The most commonly referenced radius in studies of cluster outskirts is r_{200}, often called the virial radius. The designation of r_{200} as the virial radius comes from early models of a collapsing spherical perturbation. Initially, the perturbation expands with the universe, but gravitational forces slow its expansion, causing it to decouple from the universe's expansion and eventually collapse. The collapsing perturbation reaches virial equilibrium at a radius equal to half the turnaround radius. In an Einstein-de Sitter universe ($\Omega_m = 1$), this virial radius is $r_{18\pi^2} \approx r_{178}$, which is simplified to r_{200}. In a ΛCDM universe ($\Omega_m = 0.3$, $\Omega_\Lambda = 0.7$), the virial radius from this model is actually $r_{100} = 1.36r_{200}$. However, the term r_{200} remains widely used in the literature to refer to the virial radius at low redshifts.

Dark matter is the dominant component in a galaxy cluster. It corresponds to $\sim$ 80% of the cluster composition. This was first discovered by Fritz Zwicky in 1933. He compared the Coma cluster mass estimated using the luminosity of galaxies with their dynamical mass obtained through the virial theorem. The dynamical mass was about 400 times the luminous mass [2]. Dark matter (DM) is primarily responsible for maintaining the satellite galaxies gravitationally bound to the clusters. Other techniques, such as X-ray mass calculations, later confirmed this invisible matter. DM is also responsible for the gravitational lensing effect of galaxy clusters that, out of curiosity, Fritz Zwicky predicted for galaxy clusters (Schneider, 2007).

The second more massive component of clusters is the diffuse plasma that accounts for $\sim$ 15% of the total mass. The intracluster medium (ICM) is composed of ionised gas where electrons have been stripped from atoms. This hot gas emits in the X-rays, providing additional means to study galaxy clusters. The emission mechanism for this gas is thermal bremsstrahlung. When the electron passes close to the proton, its trajectory is deflected and loses energy, emitting a photon in X-ray. The plasma temperature varies between $10^7 - 10^8\,\mathrm{K}$ ($2 - 10\,\mathrm{keV}$). The ICM is very diffuse. Its density varies from $10^{-2} - 10^{-3}\,\mathrm{cm}^{-3}$. The typical emission power or X-ray luminosity is $L_X = 10^{45}\,\mathrm{erg\,s}^{-1}$, making clusters shine and having their X-ray emission detected at large distances (Arnaud et al., 2011).

Galaxies account for only $\sim$ 5% of the cluster's total mass. Besides stars and dark matter, galaxies have an interstellar medium (ISM) composed of atomic, ionised, and molecular gas, as well as dust, cosmic rays and a magnetic field. Atomic hydrogen is the main component of the interstellar medium.

Galaxy clusters exhibit self-similarity, meaning their fundamental characteristics remain consistent regardless of variations in size or mass. This includes properties of the intracluster gas, cluster dynamics, and the spatial distribution of galaxies. Scaling relations link observable quantities such as X-ray luminosity, temperature, size, total mass, gas mass, and the velocity dispersion of member galaxies. The mass-temperature relation, for example, states that the hotter a galaxy cluster's intracluster gas, the more massive it tends to be. We can also find a relationship between galaxies' velocity dispersion and the ICM's temperature. Both reflect the depth of the gravita-

[2] Zwicky assumed the stars in the cluster galaxies have an average mass-to-light ratio (M/L) similar to that of our Sun; we would conclude $M = (M_\odot/L_\odot)L$. However, stars in early-type galaxies are, on average, slightly less massive than the Sun and thus have a slightly higher M/L. Thus, the above mass estimate needs to be increased by a factor of 10.

tional potential well. Therefore, the galaxy "gas" kinetic energy must be proportional to some property of the ICM. The X-ray luminosity and X-ray temperature are proportional to the velocity dispersion of member galaxies. Cool core clusters show a significantly higher normalization in the $L_X - T_X$ and $L_X - M_X$ relations (Chen et al., 2007).

1.3 Galaxy evolution

In the local Universe, galaxies display a wide range of morphologies. These different galaxy types motivated Edwin Hubble to propose a morphological classification sorting galaxies into ellipticals, lenticulars, barred- and unbarred-spirals (Hubble, 1936). Red passive elliptical and gas-deficient galaxies dominate the dense core of galaxy clusters, while blue star-forming and gas-rich spirals prefer lower-density environments (e.g. Vulcani et al., 2010; Kennicutt, 1983; Giovanelli & Haynes, 1985; Dressler, 1980). This observed dichotomy triggered the search for the physical mechanisms responsible for causing it. Galaxy clusters are ideal for studying galaxy evolution as they provide various galaxy and ICM densities. Analyzing the spiral galaxies in clusters, we can learn if they were formed locally, resisted the destructive cluster environment, or were newcomers that had no time to be transformed yet. Their stellar and gaseous disks are delicate, which makes them useful environmental probes.

1.3.1 Evolutionary physical processes

Understanding quenching mechanisms is crucial for comprehending galactic evolution. The quenching process involves a galaxy losing cool gas, which significantly inhibits the birth of new stars. Evolutionary physical processes can be categorized into two main types: **internal** and **environmental**. Internal mechanisms are processes that affect all the galaxies independently of the environment in which they are located. These include injecting energy and matter back into the ISM through stellar (e.g. Walch et al., 2012) or AGN (e.g. Fabian, 2012) feedback and the phenomenon of stellar bulge stabilizing molecular clouds in the disk against collapse via morphological quenching (e.g. Martig et al., 2009).

There is a plethora of gravitational and hydrodynamical mechanisms related to the environment that can shape galaxy evolution (see Boselli & Gavazzi, 2006, for a review). Among the gravitational processes are galaxy harassment (accumulation of

successive fast encounters within clusters, Moore et al., 1996), galaxy-galaxy interactions (Spitzer & Baade, 1951), and galaxy-cluster interactions (Byrd & Valtonen, 1990). These mechanisms act on all galactic components: gas, stars, and dark matter. Different from the gravitational processes, hydrodynamical processes such as thermal evaporation (hot gas eliminates cold gas by a combination of thermal conduction and ablation, Cowie & Songaila, 1977), viscous stripping (galaxy gas removal through the viscosity momentum transfer between the outer layers and the ICM, Nulsen, 1982), and ram-pressure stripping (RPS, galaxy gas removal through the pressure due to the ICM, Gunn & Gott, 1972) affect directly only the gas component. In dense environments, it is possible to have more than one mechanism affecting galaxies simultaneously: starvation (interruption in galaxy gas accretion due to several processes, Larson et al., 1980) and pre-processing in galaxy groups (Zabludoff et al., 1996; Fujita & Goto, 2004; Lopes et al., 2024) and post-processing in cluster-cluster mergers (see Sec. 1.3.5) combine gravitational and hydrodynamical processes. We describe the environmental physical properties below:

Galaxy-galaxy interaction

Galaxy-galaxy interactions are remarkably efficient at removing matter from the galaxy halo (e.g. Puglisi et al., 2021). However, it's crucial to note that the H I gas, which is more extensive and weakly bound than the central H_2, is particularly susceptible to being removed during tidal interactions (e.g. Valluri & Jog, 1990). These interactions can also lead to a significant increase in nuclear star formation in galaxies (e.g. Keel et al., 1985; Kennicutt et al., 1987). Compared to clusters, mergers are more common in groups due to the lower relative velocities between satellite galaxies (e.g. Vijayaraghavan & Ricker, 2013). In galaxy clusters, the high-relative velocities of galaxies act as an impediment to strong perturbations (e.g. Mihos, 2004). The formation of the elliptical galaxies observed in clusters can be due to major mergers of two spirals, but the fractions of lenticular galaxies cannot be accurately obtained by simply including mergers in the simulations (e.g. Okamoto & Nagashima, 2001).

Galaxy-cluster gravitational interaction

Massive galaxy clusters exert significant influence on galaxies within them, causing various effects such as gas inflow, bar formation, nuclear activity, and potentially triggering star formation in the disk (e.g. Merritt, 1984; Miller, 1986; Byrd & Valtonen,

1990). Depending on the orientation relative to the cluster's orbital plane, galaxies may exhibit a spiral pattern, where the disk aligns parallel to the orbital plane, or develop a bulge when the disk is perpendicular or inclined (e.g. Valluri, 1993). This perturbation effect can be quantified by the perturbation parameter (P_{gc}), calculated as the ratio of cluster mass to galaxy mass divided by the cube ratio of cluster-centric distance to galaxy radius. When P_{gc} exceeds a critical threshold of approximately $0.006 - 0.1$, gas within the galaxy's disk is driven towards its centre over timescales of $2 - 3 \times 10^8$ years, triggering nuclear activity (e.g. Byrd & Valtonen, 1990). Rarely does the gravitational interaction with the galaxy cluster directly remove gas from a galaxy.

Galaxy harassment

Galaxy harassment depends on the frequency and strength of individual collisions, the cluster's tidal field and the distribution of potential within galaxies, which has profound consequences for galactic dynamics and morphology (e.g. Moore et al., 1996, 1998, 1999). This process heats the stellar component, elevating its velocity dispersion while reducing angular momentum. Consequently, gas within galaxies is drawn towards their centres, enhancing star formation (Fujita, 1998). Simulation studies indicate that the collision rate among galaxies escalates by $10\% - 50\%$ in the presence of substructure within galaxy clusters, accentuating the impact of harassment on galactic evolution (Gnedin, 2003). Understanding and mitigating the bias these effects can cause in a study is crucial for our comprehension of galactic evolution.

Thermal evaporation

Thermal evaporation occurs when the temperature of the Intracluster Medium (ICM) significantly exceeds galaxies' velocity dispersion, leading to the evaporation of gas not held by gravity. A relationship governs this process: the mass loss is equal to a constant multiplied by the galaxy radius, ICM density, mean free path of the ions in the hot gas and sound speed in the ICM (Nulsen, 1982). The extent of thermal evaporation is influenced by the temperature of the ICM and the presence of a magnetic field (Cowie & Songaila, 1977). However, quantifying its effects on galaxies' structural properties and star formation rate is challenging. The complexity of the interactions involved, including the spatial distribution of the ICM and the magnetic field strength, necessitates further research to understand these effects fully.

Ram pressure stripping

As a galaxy infalls into the ICM, it can suffer gas loss due to the pressure exerted by the ICM. RPS is proportional to the density of the ICM, $\rho_{\rm ICM}$, and the square of the relative velocity between the galaxy and the medium, v^2 (Gunn & Gott, 1972). The condition for a galaxy infalling face-on to undergo RPS is the following:

$$\rho_{\rm ICM} v^2 > 2\pi G \Sigma_{\rm Gas} \Sigma_{\rm Stars} \tag{1.1}$$

where $\Sigma_{\rm Gas}$ and $\Sigma_{\rm Stars}$ are the surface densities of the interstellar gas and the stars within the disk of the galaxy, respectively. This equation means that for RPS to occur, the ram pressure (left side) has to be greater than the disk's gravitational restoring force per unit area (right side). Long tails of stripped material trailing after infalling galaxies (e.g. Sun et al., 2006; Poggianti et al., 2017b) and truncated outer margins of galaxy disks (e.g. Koopmann & Kenney, 2004) causing outside-in quenching (e.g. Quilis et al., 2000) are some of the common RPS characteristics. The most notorious cases of galaxies undergoing RPS are known as the jellyfish galaxies. In Fig. 1.2, we see JW100, a galaxy with jellyfish features infalling in the direction of the BCG in Abell 2626 cluster. Its long tails exhibits star formation and can be seen in the optical as colimated blue trails of stripped debris and impressive Hα filaments that are longer than the stellar body. Recent studies have found interesting RPS effects, such as the unwinding of the spiral arms (Bellhouse et al., 2021) and AGN triggering (Poggianti et al., 2017a).

Viscous stripping

Viscous stripping removes gas via viscosity-mediated momentum transfer between a galaxy's outer layers and the intracluster medium (ICM). The mass-loss rate depends on whether the flow is turbulent or laminar. Higher ICM densities and galaxy velocity in both cases lead to a higher mass-loss rate. This quantity is also proportional to the galaxy radius, but in the laminar case, the radius dependency is linear, whereas in the turbulent case, it is quadratic. Viscous stripping signatures are asymmetrical and more often on the leading side of the galaxy. The impact on galaxy star formation, kinematics, and molecular gas content is similar to what RPS causes (Nulsen, 1982).

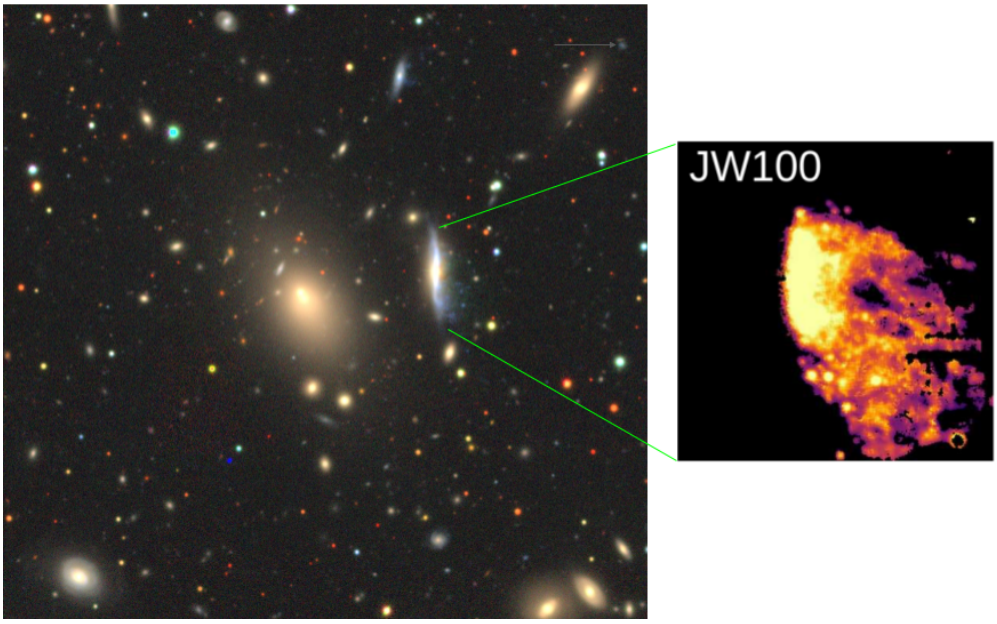

Figure 1.2: Jellyfish galaxy JW100 infalling in A2626. JW100 travels toward the BCG and leaves bright tails of stripped debris behind while it crosses the ICM. In the zoomed panel, we see JW100 Hα image obtained with MUSE by the GASP survey.

Starvation

Starvation stems from halo removal processes such as RPS, which destroy a galaxy's gas supply. As a galaxy's halo diminishes, its ability to continue accreting gas decreases, leading to the cessation of star formation. This phenomenon induces morphological changes, with spirals becoming less prominent and galaxies transitioning into anaemic, disk-dominated lenticular forms (Larson et al., 1980).

Pre-processing

Pre-processing of galaxies in groups before their infall into a cluster encompasses various physical processes such as galaxy-galaxy interactions, RPS, starvation, and evaporation. These interactions within the group induce subsequent galactic evolution upon entering the cluster environment. Notably, mergers within these groups can lead to the formation of lenticular galaxies observed within clusters. Additionally, pre-processing contributes to the suppression of star formation rates (SFR) at elevated cluster-centric distances. Since pre-processing is one of the central topics of this thesis, we expand on this subject in Sec. 1.3.3.

1.3.2 Relative importance of physical processes

Physical processes occur at different rates depending on the cluster-centric distance of the galaxy. In the central regions of the cluster, interactions between galaxies and the ICM, such as RPS, viscous stripping, and also starvation are particularly efficient at removing the outer disk gas and quench star formation. Conversely, in the outskirts of the cluster, interactions related to lower galaxy velocities, such as galaxy-galaxy interactions and pre-processing, play more significant roles. This kind of interaction can produce a significant morphological change and transform spirals into lenticulars.

Galaxies take $\sim 10^{10}$ yr to relax after a tidal interaction. Ram-pressure stripping is a much faster process, and it takes around a crossing time ($\sim 10^{9}$ yr) to finish. Thermal evaporation and viscous stripping are even faster processes and can be completed in less than ($\sim 10^{8}$ yr).

Among all of those mentioned physical processes, RPS has been proven to be one of the most efficient for impacting galaxy evolution inside clusters (Boselli et al., 2021; Cortese et al., 2021). In particular, it has been shown that significant gas removal occurs on the first infall and that RPS is more efficient in massive clusters where it can start stripping galaxies at larger cluster-centric radii (Jaffé et al., 2015, 2018; Oman et al., 2021). Also, RPS can temporarily enhance star formation (SF) for the galaxies, as seen on the SF main sequence (Bekki, 2009; Vulcani et al., 2018) and produce optically bright tails of stripped material, which give rise to jellyfish-like features (Smith et al., 2010; Ebeling et al., 2014; Fumagalli et al., 2014; Poggianti et al., 2017b).

1.3.3 Pre-processing in galaxy cluster substructures

RPS depends on the density of the intracluster medium (ICM) and the relative velocity between galaxies and ICM (Gunn & Gott, 1972). Therefore, RPS is expected to be stronger near the cluster core, where galaxy velocity and ICM density are higher than in the outskirts. However, RPS candidates have been found beyond the virial radii (e.g. Jaffé et al., 2018). Many studies have also found quenched galaxies in the cluster outskirts (e.g. Wetzel et al., 2013). This excess of quenching in the infall region can be partially explained by backsplash galaxies that have already entered the cluster and passed through the core. Even so, an excess in the quenching fraction has been found beyond the backsplash radius (Haines et al., 2015; Jaffé et al., 2015; Lopes et al., 2024). The idea that galaxies are pre-processed in galaxy groups and filaments before entering the galaxy clusters is gaining momentum as large photometric and spectroscopic

surveys are imaging a crescent number of systems out to the infall region.

Many techniques are used to identify the presence of substructures in clusters with X-ray (e.g. Mohr et al., 1993; Poole et al., 2006; Laganá et al., 2010, 2019), microwave (e.g. Andrade-Santos et al., 2017; Cialone et al., 2018), gravitational lensing (e.g. Monteiro-Oliveira et al., 2017a,b, 2020), and the analysis of optical data (e.g. Einasto et al., 2010; Ribeiro et al., 2013a; Cohen et al., 2014; Jaffé et al., 2016). Most optical diagnoses use galaxy position and/or redshifts to identify the substructures. One-dimensional substructure techniques test if the velocity distribution deviates from the Gaussian (e.g. Ribeiro et al., 2013b; Morell et al., 2020). Two-dimensional substructure techniques comprise density-based algorithms (e.g. density contours, `DEDICA`, `DBscan`, and `CALSAGOS`, Geller & Beers, 1982; Ramella et al., 2007; Olave-Rojas et al., 2023), and symmetry tests (e.g. β test, West et al., 1988). These diagnostics are helpful when spectroscopic data are insufficient, although the projection effect of foreground and background galaxies can affect them.

In the three-dimensional category, there are methods using both galaxy positions and redshifts. The Dressler-Shectman (`DS`, Dressler & Shectman, 1988) method is the most employed in astronomy. Other methods in this category include the three-dimensional (3D) wavelet transforms (Flin & Krywult, 2006), the 3D version of the adaptive-kernel `DEDICA` code (Pisani, 1993), 3D Gaussian mixture models such as `mclust` (Scrucca et al., 2016), and hierarchical algorithms such as `S-tree`, the `h-method`, the σ`-plateau` method (Diaferio, 1999), `Blooming Tree` (Yu et al., 2018). A limited number of methods enable the identification of galaxies belonging to substructures within galaxy clusters. These methods include `DEDICA`, hierarchical techniques and `mclust`.

Recently, Biviano et al. (2017, B17 hereafter) developed an improved version of the `DS` test capable of retrieving the substructure members. Benavides et al. (2023, B23 hereafter) showed that `DS+` could identify approximately ~ 80 per cent of galaxies from real groups as members of substructures. Additionally, it successfully assigns at least ~ 60 per cent of the galaxies identified as part of substructures to real groups within galaxy clusters. Therefore, `DS+` is a powerful tool to identify substructures in galaxy groups, allowing us to robustly investigate galaxy pre-processing in groups.

1.3.4 Pre-processing in intracluster filaments

In addition to groups, filaments of galaxies that feed the galaxy clusters play an important role in galaxy pre-processing. Galaxies in filaments are also found to be redder (Chen et al., 2017; Luber et al., 2019), more quiescent (Martínez et al., 2016; Kuutma et al., 2017), more elliptical (Kuutma et al., 2017), and have higher stellar masses (Alpaslan et al., 2016; Chen et al., 2017) than field galaxies. However, identifying filaments from a set of discrete locations provided by a galaxy survey poses a big challenge. Photometric and spectroscopic surveys face numerous obstacles, such as biases, insufficient sky coverage, projection effects, and observational errors. Various approaches have been developed to tackle this problem (see Libeskind et al., 2018). Many studies show that galaxies are preferentially distributed along the major axis of the brightest cluster galaxy (BCG, Binggeli, 1982; Niederste-Ostholt et al., 2010; Chu et al., 2021, 2022). Smith et al. (2023) suggest that clusters and their associated BCGs exhibit accretion tendencies aligned with the filaments within which they are situated. This conclusion is supported by the alignment of BCGs with both cluster members and cosmic filaments. This correlation between the directional growth patterns of the cluster and BCG could be a simple alternative to identifying the main filament axis. However, this approach does not consider that clusters can have more than one significant filament axis.

Lately, more studies have gradually shown a modulation of the quenching fractions around the BCG major axis. Martín-Navarro et al. (2021) showed higher quenching fractions in the BCG major axis direction. Their data was based on an optical catalogue from the Sloan Digital Sky Survey (SDSS, Ahn et al., 2014) of $\sim$ 30000 dark-matter halos in the local universe ($z < 0.08$). After finding a similar trend in the IllustrisTNG (Nelson et al., 2019) cosmological simulations, they claimed that the origin of the anisotropic quenching was related to the central supermassive black hole (SMBH) activity. The SMBH feedback preferentially happens in the direction of the BCG minor axis, creating cavities where the ICM is less dense. Infalling galaxies from that direction would face less RPS and be less quenched. However, a recent theoretical work that did not include black hole feedback in their simulations also found an anisotropic quenching signal in the same direction (Samuel et al., 2023). Furthermore, Karp et al. (2023) revised Martín-Navarro et al. (2021) using cosmological simulations and showed that satellite galaxies along the major axis of the dark matter halo tend to have been accreted at earlier cosmic times and are hosted by subhalos of larger peak

halo masses, resulting in a higher quenched fraction in the major axis direction. Stott (2022) used 13 massive clusters from The Cluster Lensing and Supernova Survey with Hubble (CLASH, Postman et al., 2012) at $z = 0.5$ and showed that rest-frame colours were redder in the BCG major axis direction in agreement with the studies above. They explain that the source of this phenomenon is the oblate shape of the ICM. Galaxies entering the cluster from the minor axis direction face a smaller amount of ICM gas than in the major axis, suffering less RPS. Lastly, Ando et al. (2023) extended this work to $z = 1$ with a large optically-selected cluster catalogue constructed from the Hyper Suprime-Cam (HSC, Furusawa et al., 2018; Komiyama et al., 2018; Miyazaki et al., 2018), finding a similar modulation in the quenching signal.

While pre-processing in galaxy groups impacts galaxy evolution, many aspects remain unknown. The efficiency of quenching in groups is still unclear. The leading cause of quenching in clusters beyond the turnaround radius needs to be determined, and quantification of the importance of pre-processing in quenching is also required (Hou et al., 2014). The physical processes acting in these environments remain unclear. In galaxy groups, mechanisms such as strangulation are efficient in quenching galaxies (De Lucia et al., 2012; Peng et al., 2015). Also, mergers are an essential mechanism of gas removal and morphological change, and they are twice more frequent in groups than in clusters (Vijayaraghavan & Ricker, 2013). Recent works using HI content suggest that the intragroup medium can shield galaxies from strong ram pressure effects while infalling in a cluster (Hess et al., 2022).

1.3.5 Post processing due to galaxy cluster mergers

Models of RPS often assume simplified virialised and symmetric clusters. However, in the hierarchical scenario, clusters of galaxies continue to grow from the accretion of small groups and even from collisions with structures of comparable size (Press & Schechter, 1974). Cosmological simulations indeed show that massive clusters ($\sim 10^{15} h^{-1} \mathrm{M}_{\odot}$) in the local Universe have accreted $\sim$40 per cent of their galaxies through groups more massive than $10^{13} h^{-1} \mathrm{M}_{\odot}$ (McGee et al., 2009). In addition, observations suggest that 10–20 per cent of clusters at $z < 0.3$ are undergoing mergers with other clusters (Katayama et al., 2003; Sanderson et al., 2009; Hudson et al., 2010). Major cluster-cluster mergers are one of the most energetic phenomena since the big bang and can release $\gtrsim 10^{64}$ ergs of energy during one crossing time (~ 1 Gyr) (Sarazin, 2002). These collisions result in perturbations in the galaxy's orbits and the plasma fill-

Figure 1.3: *Chandra*'s X-ray observations reveal clumps of hot gas (pink), containing most baryonic matter in two galaxy clusters, with one cluster's gas passing through the other and being slowed down during the collision. Gravitational lensing in optical images confirms that two non-collisional dark matter clumps pass through each other, unaffected by drag forces, and are the most dominant component in the bullet cluster system. X-ray: NASA/CXC/CfA/M. Markevitch, Optical and lensing map: NASA/STScI, Magellan/U.Arizona/D. Clowe, Lensing map: ESO WFI

ing the space between the clusters' members. In a collision of clusters, the ICM and dark matter behave in different ways, providing information about their natures. In Fig. 1.3, we see the iconic bullet cluster system, showcasing the collision of the two massive galaxy clusters. The image shows how the dark matter [3](purple) and galaxies (orange) move across the other cluster without colliding while the ICM (pink) collide and get stuck in the middle of the two clusters. This cluster is a good illustrative example of the behaviour of the different cluster components during a major collision.

The idea that highly energetic phenomena, such as the accretion of large galaxy groups or collisions between galaxy clusters, exert a significant impact on the galaxy evolution has been referred to as "post-processing" (Vijayaraghavan & Ricker, 2013). This idea has been supported by observational studies that found quenching of the SF (Fujita & Nagashima, 1999; Domainko et al., 2006; Kapferer et al., 2009), enhanced SF in galaxies near shock regions of the intracluster medium (ICM) (Stroe et al., 2014, 2015), both quenching and enhancement of the SF (Hwang & Lee, 2009; Ma et al., 2010; Stroe et al., 2014; Kelkar et al., 2020), and enhancement of RPS in dynamically disturbed clusters (Owers et al., 2012; Rawle et al., 2014; McPartland et al., 2016; Ebeling & Kalita, 2019; Roman-Oliveira et al., 2019; Ruggiero et al., 2019). Similarly, hydrodynamical simulations show that cluster mergers can increase the RPS through higher

[3]The dark matter distribution in this image was inferred through gravitational lensing analysis.

ICM densities or relative velocities between the galaxies and the ICM (Vijayaraghavan & Ricker, 2013; McPartland et al., 2016; Ruggiero et al., 2019). These apparently contradictory results show that the impact of cluster growth on galaxy evolution is not fully understood.

1.4 This thesis

The main objective of this thesis is to understand the physical mechanisms involved in galaxy pre and post-processing. The post-processing side is inspired by the findings of a few focused observational works that suggest an enhancement of ram-pressure-stripped galaxies in disturbed environments. We addressed this hypothesis using a statistical sample of ram pressure stripping candidates and galaxy clusters in different dynamical states to quantify the fractions of galaxies undergoing ram pressure in the different states. The pre-processing chapters in this thesis were motivated by the existing knowledge gap about which physical mechanisms dominate in infalling galaxy groups and what the importance of RPS is in this environment. The samples used in this thesis are described in Chapter 2. The third and fourth chapters are based on the first paper we published in this PhD, Lourenço et al. (2023, , hereafter Paper I); Chapter 3 describes the several methods we used to classify the dynamical states of the clusters in our sample. We used techniques based on optical, X-ray, and radio wavelengths. In Chapter 4, we described the methods and results of the ram pressure stripping fractions using cluster members obtained with a photometric approach and members obtained with spectroscopy. Chapter 5 presents the preliminary results of a paper in preparation by Lourenco et al. (in prep., hereafter Paper II). While Paper I is related to post-processing in galaxy clusters, in paper II, we study pre-processing in galaxy groups and filaments that feed the galaxy clusters, focusing on ram pressure. Chapter 6 synthesises our interpretation of the impact of cluster growth on the enhancement of ram pressure stripping according to our results and discusses possible complementary research to clarify further the questions presented in this essay.

CHAPTER 2

Data and samples

Since this study attempts to statistically address the incidence of RPS candidates in evolving clusters, groups, and filaments, we based our analysis on the largest and most homogeneous sample of optically selected RPS candidates at low redshift known to date from Poggianti et al. (2016, P16 hereafter). P16, described in Sec. 2.2.1 is the largest sample of stripped galaxies and it is ideal, as it is hosted by a wide variety of clusters with homogeneous optical data from the WIde-field Nearby Galaxy Cluster Survey (WINGS) and OmegaWINGS (Sec. 2.1), some of which are also covered by archival *Chandra* and *XMM-Newton* X-ray data and radio observations (Sec. 2.1.2 and 3.4), as described in the following. The importance of RPS in local clusters was recently investigated in Vulcani et al. (2022, V22 hereafter), by characterising the fraction of galaxies with optical ram-pressure features using the same data-set.

2.1 Cluster sample

WINGS (Fasano et al., 2006) is a multi-wavelength imaging survey primarily in B and V bands (Varela et al., 2009) of 77 X-ray selected clusters of galaxies in the local Universe (Ebeling et al., 1996, 1998, 2000) limited only on the distance from the galactic plane ($b \geqslant 20^{\circ}$) and in redshift ($z = 0.04 - 0.07$). A multi-object spectroscopic follow-up obtained data for galaxies in 48 of those clusters (Cava et al., 2009; Moretti et al., 2014). The WINGS sample covers a wide range of masses M_{200} ($\sim 5 \times 10^{13}$ to $> 10^{15}$

$M_\odot$), X-ray luminosities ($\log L_X$ = 43.2 – 44.7, measured in the 0.1 – 2.4 keV energy band). Each sample cluster was imaged with a field of view (FOV) of $34' \times 34'$. When observed with good seeing, most clusters reached a magnitude $V \sim 22.0$ mag or even fainter than this. The OmegaWINGS survey extended the coverage area to $1^\circ \times 1^\circ$ of each cluster, for 46 clusters (Gullieuszik et al., 2015) from which 33 also had spectroscopic follow-up (Moretti et al., 2017).

The physical radius R_{200} is taken from Biviano et al. (2017) when available; if not, they were obtained by following the method used in Durret et al., (2021; see also Kolcu et al. 2022), inserting the observed line of sight velocity dispersion in $\sigma_{cl} = 1090 \times [h(z) \times M_{200}]^{1/3}$, Eq. 1 from Munari et al. (2013) and the relation

$$R_{200} = \left(\frac{G\, M_{200}}{100\, H_z^2} \right)^{1/3}, \tag{2.1}$$

where the Hubble constant at z is $H^2(z) = H_0^2[\Omega_0(1+z)^3 + \Omega_R(1+z)^2 + \Omega_\Lambda]$ and $h(z) = H(z)/100\,\mathrm{km\,s^{-1}\,Mpc^{-1}}$ (Peebles, 1993). M_{200} is expressed in units of $10^{15}\ M_\odot$, and σ_{cl} is the uni-dimensional velocity dispersion in units of km/s.

In total, WINGS and OmegaWINGS have obtained 24122 galaxy redshifts. After a recent systematic search for additional redshifts in the photometric sample, V22 and references therein increased the spectroscopic sample to 46700. The additional redshifts were considered for assigning cluster membership and for the substructure analysis (see Sec. 3.2.1). The cluster members were identified based on a 3σ clipping method as described in Paccagnella et al. (2017).

2.1.1 P16 cluster sample

The parent cluster sample comprises 72 WINGS clusters from P16 (41 are also in OmegaWINGS), which presented the first sizeable systematic search for RPS candidates at low redshift. Details about the galaxies in this sample can be found in Sec. 2.2

The spatial coverage of the clusters in the WINGS/OmegaWINGS surveys varies as a result of the different cluster sizes and redshifts and the different FOV of the surveys. To obtain a physical radius that maximised the size of our cluster sample and its radial extent, we calculated the maximum radii for which each cluster is fully covered by the FOV of the WINGS and/or OmegaWINGS surveys, finding a range from 0.3 R_{200} to 2.1 R_{200}. Ideally, we would like to study galaxies well beyond R_{200} to understand how the different dynamical states impact the incidence of RPS candidates in the infalling region. However, this is not always possible, and limiting the analysis

to clusters that satisfy this criterion would limit the sample significantly. We found that 75 per cent of the sample have spatial coverage reaching $0.7\,R_{200}$ or beyond. This radial cut limits our sample to 52 clusters from P16 in the different dynamical states without penalising the sample size significantly. We, therefore, use these 52 clusters in our analysis.

2.1.2 X-ray sample

We cross-matched the P16 sample with a catalogue of 964 galaxy clusters from *Chandra* with X-ray morphological parameters computed by Yuan & Han (2020, Y20 hereafter). Subsequently, we replicated the aforementioned process with the sample of a complementary study for 1308 clusters from *XMM-Newton* performed by Yuan et al. (2022, Y22 hereafter). Analysing the correlation between these parameters helps to build the widely used dynamical state diagnostics presented in Sec. 3. We found 35 *Chandra* and 36 *XMM-Newton* clusters that have complete photometric coverage at $0.7\,R_{200}$ and are in common with P16, for a total of 45 distinct objects.

As a sanity check, we compared the X-ray morphological parameters obtained in YH20 with the ones obtained in Y22 for the 26 objects in common between the two data-sets. Overall, we found a small departure from the reference 1:1 line and a high Spearman correlation coefficient ($\geq$ 0.7) for the centroid shift, concentration, and power ratio, which agrees with Y22, who run a similar comparison with a larger cluster sample of 351 clusters. Therefore, we decided to merge both catalogues. We preferentially used the *Chandra* data since their spatial resolution is better than the *XMM-Newton*. This is very important to identify some sharp features that we consider for the dynamical state classification of the cluster sample.

2.1.3 Spectroscopically complete sample

Out of 52 P16 clusters that reached $0.7\,R_{200}$, 49 have spectroscopic completeness $>$ 50 per cent at a total magnitude brighter than $V = 17.77$ mag. We refer to these clusters as the spectroscopically complete sample. This magnitude limit comes from the photometric analysis performed in Sec. 4.2, where we correct the RPS candidate fractions for the field contamination. It was necessary to use this limit so that we could fairly compare both photometric and spectroscopic samples.

Figure 2.1 shows the halo mass distribution of the different samples used in this paper, including the P16, X-ray, and spectroscopically complete samples mentioned

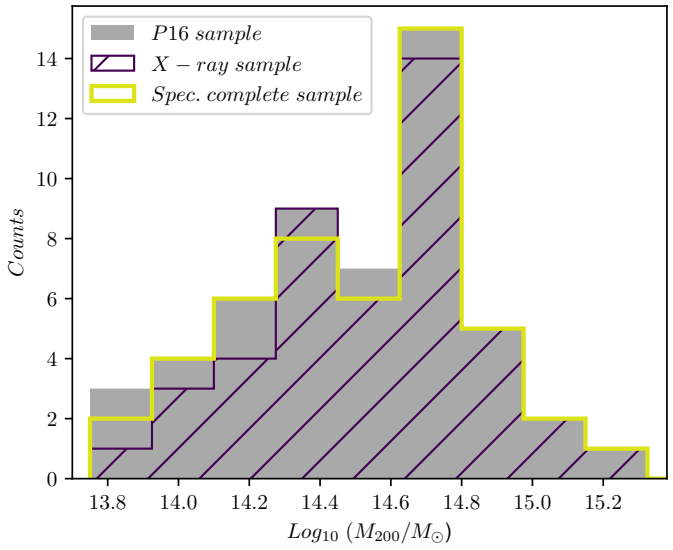

Figure 2.1: Mass distribution of the different cluster samples used in this paper. Masses were retrieved from Biviano et al. (2017). The parent sample is from P16 (52 clusters), followed by the cluster samples with available X-ray data (45 clusters), and the spectroscopically complete cluster sample (49 clusters). Only clusters that have complete photometric coverage at 0.7 R_{200} are included in those samples.

in this section. These masses were computed in Biviano et al. (2017). In Tab. A.1, we specify to which sample(s) each cluster belongs.

2.2 Galaxy sample

WINGS and OmegaWINGS provide valuable information for their galaxy samples, such as galaxy colour and morphology, as well as spectroscopic quantities, permitting the study of galaxy evolution in the local Universe in an unprecedented way with a large sample.

The total absolute magnitudes for the member galaxies, M_B and M_V, were derived from the total (SExtractor AUTO) observed B and V magnitudes (Moretti et al., 2014; Gullieuszik et al., 2015), corrected for distance modulus, foreground Galaxy extinction, and k-corrected using tabulated morphology dependant values from Poggianti (1997). Morphologies were obtained by MORPHOT (Fasano et al., 2012), an automated, non-parametric tool for the morphological-type estimate of large galaxy samples.

In our photometric and spectroscopic analysis, we only use galaxies with $M_V < -19.5$, which is the magnitude limit used in MORPHOT classifications. Similar to Fasano et al. (2012), we consider late-type galaxies, the ones with MORPHOT classifications within $0.5 \leq Morphological\ Type \leq 10.5$. This revised Hubble type range encompasses S0/a, Sa, Sab, Sb, Sbc, Sc, Scd, Sd, Sdm, Sm, Im, and compact irregular galaxies (cI).

The BCGs used in this work are primarily those identified in Fasano et al. (2010). Because in this paper we use BCGs to define the cluster centre (when possible, see Sec. 3.7), we revised case by case using the optical and X-ray data in hand and found that in a few cases, their BCGs were not the bright galaxy closest to the X-ray emission peak. We describe these cases in the appendix A.1.

2.2.1 Ram-pressure stripping candidates

In P16, the identification and classification of the RPS candidates were made by a few human classifiers with no information about the galaxy environment, cluster centre or memberships. The P16 cluster sample only included clusters with B and/or V-band seeing ≤ 1.2 arcsec to visually search for the RPS candidates. Galaxies with tails, gas disturbance, asymmetrical star formation, and bow shock features were selected as RPS candidates. The classifiers assigned a classification (Jclass) from 1 to 5 according to how confident they were that the galaxy was undergoing RPS. Jclass 1 has the lowest confidence, and Jclass 5 has the highest confidence. We excluded all the P16 candidates that were flagged with possible gravitational interaction (with comments such as "tidal", "merger", or "harassed"), getting a final sample of 53 blue late-type RPS candidates in 52 P16 clusters. We stress that clusters with no candidates within $0.7\,R_{200}$ are also included in our analysis.

As discussed in P16, most RPS candidates have low Jclass. In our sample, only ~ 28 per cent of the RPS candidates have a Jclass value of 3 or higher. While it is true that lower Jclass values indicate more uncertain cases of RPS, based on GASP[1] data of a subset of the P16 RPS candidates, Poggianti et al. (in prep) show that the "success rate" of identifying ram-pressure stripped galaxies (across all Jclass values) through broad-band optical imaging in local clusters is approximate ~ 86 per cent. In other words, the vast majority of the RPS candidates used in our study are expected to be

[1]GAs Stripping Phenomena in galaxies with MUSE (GASP) is an integral-field spectroscopic survey with MUSE at the VLT aimed at studying gas removal processes in galaxies (Poggianti et al., 2017b).

"real" cases of ram-pressure stripping at play.

Later, V22 repeated the search for RPS candidates in the WINGS/OmegaWINGS cluster sample. Unlike in P16, in V22, the search was only performed among cluster members. In Chapter 5, as we use only spectroscopic members, we include V22 sample. We excluded the candidates from V22 with unwinding spiral arms. There is evidence that unwinding spiral arms are associated with RPS (Bellhouse et al., 2021), but because there is no estimate of the confirmation rate of the unwinding RPS candidates, we decided not to include them in our analysis.

CHAPTER 3

Dynamical state classification of galaxy clusters

In this chapter, we delve into the complex world of cluster dynamics, using many diverse proxies commonly found in the literature. As discussed in the introduction, it is challenging to reliably quantify cluster dynamical state using a single proxy due to observational limitations and biases. The challenges we encountered include different relaxation timescales when dealing with different wavelengths. Our approach is multifaceted, incorporating techniques based on the X-ray morphology of the ICM, optical methods such as the fractions of members in substructures, the magnitude gap between first and second-ranked galaxies, and the fraction of members in the largest substructures. We also include radio information, such as radio halos and relics, to characterise a class of very disturbed clusters. Our ultimate goal is to create a comprehensive classification scheme that considers all the information in hand, attempting to mimic the time sequence of their state of interaction.

3.1 Proxies for understanding galaxy cluster dynamical states

A relaxed cluster, with no recent interactions, is characterised by a round and symmetrical gas distribution, similar to an ellipsoid; depending on the angle concerning the observer, it can be seen like a ball. Their member galaxies follow a symmetrical distribution around a single and unquestionable BCG. In relaxed clusters, both galaxy and gas densities are higher towards the cluster centre. Cluster mergers, significant events in the life of a cluster, can disturb galaxies and gas distributions. The past interactions can be observed by features in the optical, radio and X-rays.

One of the main difficulties in galaxy evolution studies in disturbed clusters is defining, robustly, the dynamical state of large samples of clusters in a way that the time sequence and magnitude of the disturbances are portrayed. There are many substructure diagnostics for galaxy clusters at different wavelengths, each reflecting a different aspect of a cluster's dynamical state. For instance, the X-ray emission from the ICM has been widely used to study merger-induced shocks (Markevitch & Vikhlinin, 2007; Botteon et al., 2018; Ha et al., 2018) and cold fronts (CF, Owers et al., 2009; Ascasibar & Markevitch, 2006). CF are isobaric surface brightness discontinuities where the denser regions are colder than the rarefied ones and provide evidence of gas motion even in clusters that suffered minor mergers (Ghizzardi et al., 2010; Birnboim et al., 2010; Hallman et al., 2010).

On the other hand, if we look at clusters in the optical, we can often find substructures traced by the cluster galaxies themselves, which can share common positions and velocities. Substructures detected in the optical are indeed recently accreted halos that can lose 25–45 per cent of their mass per pericentric passage (Taylor & Babul, 2004), getting mostly disrupted within 1–3 Gyr after infall (Choque-Challapa et al., 2019; Benavides et al., 2020).

Because of the collisional nature of the ICM, the X-ray performs better than the optical in tracing interactions for longer. Poole et al. (2006) showed, using a simulated *Chandra* image of a cluster system, that X-ray morphological parameters and offset between the X-ray peak and centre of mass can be identified up to the second pericentric passage at $z = 0.1$, and significant temperature fluctuations can persist even after the system reaches virialisation. The X-ray signatures of moderate and massive mergers last for 4.5–5.5 Gyr, while the ones of the minor mergers last for up to ~ 2 Gyr longer in their simulations. The intrinsic characteristics of each dynamical state method, such

as the timescale of relaxation, require that more than one diagnostics be used in order to obtain a robust classification of a large sample.

3.2 Optical proxies

We used substructure identification techniques derived from optical photometry (magnitude gap) and spectroscopy (fractions of members in substructures). Here, we described these techniques in detail.

3.2.1 Dressler-Shectman analysis

The Dressler-Schectman (DS) test (Dressler & Shectman, 1988) estimates the presence of substructures, groups recently accreted, within a cluster by identifying the nearest neighbours $N_{\rm nn}$ of each galaxy (confirmed spectroscopic member) and comparing the difference of their kinematics with the global kinematics of that cluster. More precisely, the test computes the differences between the velocity of each galaxy $\overline{v}_{\rm local}$[1], and velocity dispersion $\overline{\sigma}_{\rm local}$ and the cluster mean velocity and velocity dispersion, $\overline{v}_{\rm cl}$ and $\overline{\sigma}_{\rm cl}$. The following equation gives the deviations of the individual galaxies to the global kinematic parameters of the cluster:

$$\delta_i^2 = \left(\frac{N_{\rm nn}+1}{\sigma_{\rm cl}^2}\right)\left[(\overline{v}^i_{\rm local}-\overline{v}_{\rm cl})^2+(\sigma^i_{\rm local}-\sigma_{\rm cl})^2\right] \tag{3.1}$$

This test can be evaluated in two different ways. i) If the sum of deltas divided by the number of members exceeds 1, the cluster is said to have substructures. ii) The result obtained in i) can be further investigated by using Monte Carlo re-sampling of the local velocity values to obtain the probability that the cluster has a substructure (e.g. Jaffé et al., 2013). However, these methods do not identify which galaxies are members of the substructures.

[1]For each galaxy in the cluster, its N nearest neighbors are identified. The value of N is often chosen to be approximately the square root of the total number of galaxies in the cluster, i.e., $N \approx \sqrt{N_{\rm total}}$. Following, the Local Mean Velocity is computed by letting v_i be the velocity of the i-th galaxy and v_{ij} be the velocities of its N nearest neighbors.Then, the local mean velocity $\overline{v}_{\rm local}$ is calculated for the galaxy and its neighbors:

$$\overline{v}_{\rm local} = \frac{1}{N+1}\left(v_i + \sum_{j=1}^{N} v_{ij}\right)$$

Biviano et al. (2017) introduced an improved version of the DS test that is capable of identifying which galaxies belong to a substructure, the DS+ technique. This method is fully described in Biviano et al. (2017) and tested with numerical simulations in Benavides et al. (2023). Here, we briefly summarise it. DS+ does not restrict Nnn to a fixed number. Instead, it considers any possible multiplicity of neighbouring galaxies and checks for differences in their kinematics from that of the cluster as a whole. After assigning a significance to each detected group using Monte Carlo re-sampling, the groups that share one or more galaxies with a more significant group are disregarded to avoid overlapping. Groups that are close enough in distance and velocity are merged to avoid fragmentation (see eq. (3) of Benavides et al., 2023). In addition, the DS+ method differs from the DS method in that it considers the deviations in the first and second moments of the velocity distributions separately. Since real groups are not expected to have velocity dispersion larger than clusters, DS+ does not consider as significant positive deviations of the velocity dispersion of the type $\sigma^i_{\rm local} > \sigma_{\rm cl}$. Moreover, DS+ encompasses $\sigma_{\rm cl}(R)$, i.e. the cluster velocity dispersion profile (VDP), and not the whole cluster velocity dispersion, as reference. Two choices are possible for the VDP: one is obtained by smoothing the observed cluster VDP with the LOWESS (LWS) technique (Gebhardt et al., 1994), and the other is based on the Navarro Frenk White (NFW) mass profile (Navarro et al., 1997), as described in Biviano et al. (2017).

We evaluate two global substructure indicators based on preliminary work where the authors applied DS+ on simulated data (Benavides et al., 2023). One is $f_{\rm sub}$, the fraction of members that belong to sub-clusters, $N_{\rm sub}$, with respect to the number of members in the whole cluster, $N_{\rm mem}$. The other is $f_{\rm max}$, the fraction of members that belong to the richest sub-cluster, $N_{\rm max}$, with respect to $N_{\rm mem}$. We have values for each of $f_{\rm sub} = \frac{N_{\rm sub}}{N_{\rm mem}}$ and $f_{\rm max} = \frac{N_{\rm max}}{N_{\rm mem}}$.

We chose to present in this work only the results obtained with the LWS VDP since using this profile $f_{\rm sub}$ and $f_{\rm max}$ correlate slightly better than when using the Navarro et al. (1997) mass profile. NFW assumes a virialized symmetric cluster potential. Real galaxy clusters often have more complex shapes and may be triaxial or contain elongated structures. This discrepancy can lead to inaccuracies in identifying and characterizing substructures. Furthermore, the NFW profile predicts a cuspy density distribution towards the center of the halo. This high central density can dominate the signal, making it harder to detect substructures that are near the core of the galaxy cluster.

Note that in (Benavides et al., 2023) there is an overlapping mode and a non-overalapping mode. We use the latter, which, as opposed to the overlapping mode, associates a unique substructure to the cluster galaxies. The DS+ tests on simulations show that in the non-overlapping mode, the completeness (C) of the substructures identified by DS+ is around 50 per cent. C slightly increases with richness and group distance from the cluster centre. There has also been a minor dependence of C on time since infall, which allows galaxies to maintain consistent velocities even after pericenter passage and enables them to be identified as substructure members. Purity (P) is consistently above 60 per cent and slightly decreases with increasing group richness. P significantly increases with the projected distance from the cluster centre, reaching almost 100 per cent beyond the virial radius, suggesting lower contamination in regions with lower cluster density. B23 concluded with some disclaimers that the DS+ and Blooming Tree[2] test (considered the most efficient substructure finder up to now) reaches similar performances in the detection of substructures.

3.2.2 Magnitude Gap

During the growth of a halo, the central galaxy undergoes several mergers, cannibalising the satellite galaxies (e.g. Contreras-Santos et al., 2022). Over time, the difference between the mass of the central and satellite galaxies increases, which also expresses itself in a more significant difference in magnitude. The time a halo was formed is linked to its dynamical state. Dynamically evolved clusters tend to have a large magnitude gap between their first and second-ranked galaxies. Hence, the magnitude gap has been widely used in the literature to segregate between dynamical states (e.g. Dariush et al., 2007; Gozaliasl et al., 2014; Raouf et al., 2019). In particular, a magnitude gap ≥ 2 has traditionally been used to distinguish a particular class of very passive systems where no significant interaction happened in their recent history. These systems are known as fossil groups (Jones et al., 2003). Fig. 3.1 left panel shows an example of a relaxed cluster from our sample with a high magnitude gap (1.76) between the BCG and the second-ranked galaxy. In contrast, in the right panel, we have an example of a disturbed cluster with a low-magnitude gap (0.122).

Following the method described by Dariush et al. (2007), we searched for the two

[2]The blooming Tree algorithm (Yu et al., 2018) arranges galaxies based on their gravitational binding energy forming a binary tree. The algorithm identifies significant substructures by identifying local gravitational potential minima (buds) on the binary tree branches.

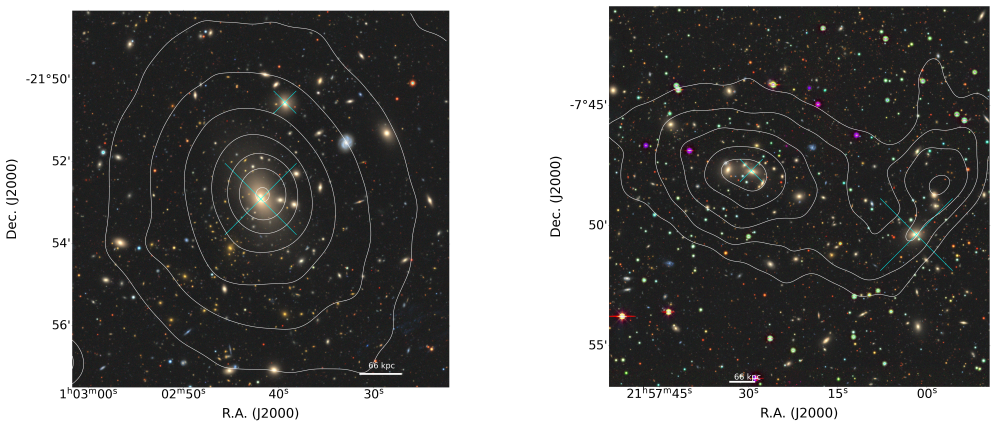

Figure 3.1: Left panel: A relaxed cluster from our sample, Abell 133. The larger cyan cross shows the BCG, and the smaller cross shows the second-ranked galaxy. The magnitude gap between the BCG and second-ranked galaxy is high (1.76). White contours show the fairly relaxed X-ray emission from *Chandra* data. Right panel: A disturbed cluster system, Abell 2399. The magnitude gap between the first and second-ranked galaxies is small (0.122). White contours show the very asymmetrical X-ray emission from XMM-Newton data.

brightest galaxies in the absolute V magnitude within a radius of $0.5\,R_{200}$ around the brightest galaxies of each cluster identified in Fasano et al. (2010). Late-type galaxies and non-members (based on available spectroscopic redshifts, when available) were excluded from this search. The magnitude gap $\Delta M_{1,2}$ is obtained with the following equation,

$$\Delta M_{1,2} = V_{\mathrm{rank2}} - V_{\mathrm{rank1}} \tag{3.2}$$

where V_{rank1} and V_{rank2} are the absolute V magnitudes of the first and second-ranked galaxies, respectively.

3.3 X-ray proxies

Here, we present several X-ray morphological parameters for the ICM computed in YH20 that have been extensively used in the literature to classify a cluster's dynamical state (e.g. Cassano et al., 2010; Rasia et al., 2013). These parameters are inspired by the traditional optical concentration, asymmetry, and smoothness (CAS) parameters (Conselice, 2003).

3.3.1 Concentration

Relaxed clusters are often so concentrated that their ICM central cooling timescales are substantially smaller than the Hubble time, causing a temperature drop in the core, being classified then as a cool-core cluster (e.g. Molendi & Pizzolato, 2001). Traditionally, the concentration ratio is measured by dividing the integrated X-ray observed flux inside two concentric apertures. In Yuan & Han (2020), they compute the concentration, c, in two circular concentric regions with the internal radius R of 100 kpc and the outer radius of 500 kpc following Cassano et al. (2010, 2013).

$$c = \frac{\sum\limits_{R<100\,\mathrm{kpc}} f_{\mathrm{obs}}(x_i, y_i)}{\sum\limits_{R<500\,\mathrm{kpc}} f_{\mathrm{obs}}(x_i, y_i)}, \tag{3.3}$$

where $f_{\mathrm{obs}}(x_i, y_i)$ is the observed flux at a pixel.

3.3.2 Centroid shift

In relaxed clusters, the X-ray emission peak tends to coincide with the flux-weighted X-ray centroid, while those can be significantly shifted in merging clusters. The centroid shift, ω, measures how much the X-ray flux-weighted centroid moves while gradually varying the aperture. Unless their distribution is very symmetrical, the presence of multiple bright X-ray clumps can influence the centroid shift. To compute ω, Yuan & Han (2020) measured the separation of the centroids Δ_i in a series of circular apertures centred in the X-ray surface brightness peak n times from $0.05R_{\mathrm{ap}}$ to R_{ap}, where R_{ap} is 500 kpc. Finally they computed the summation of the differences between Δ_i and $\langle\Delta\rangle$ as shown in the following equation:

$$\omega = [\frac{1}{n-1}\sum_i (\Delta_i - \langle\Delta\rangle)^2]^{\frac{1}{2}} \times \frac{1}{R_{\mathrm{ap}}}. \tag{3.4}$$

3.3.3 Asymmetry

Disturbed clusters are more asymmetric than relaxed ones. The asymmetry α is usually computed as the normalised difference between the surface brightness map and another one rotated by 180°.

$$\alpha = \frac{\sum\limits_{x_i,y_i} [f_{\mathrm{obs}}(x_i, y_i) - f_{\mathrm{obs}}(x_i', y_i')]^2}{\sum\limits_{x_i,y_i} f_{\mathrm{obs}}^2(x_i, y_i)} \times 100\,\% \tag{3.5}$$

3.3.4 Power ratio

Disturbed clusters usually have a non-uniform mass distribution. The halo mass fluctuations can be inferred by applying a multi-pole decomposition to the X-ray surface brightness maps, known as power ratio (Buote & Tsai, 1995). The m-order power ratio ($m > 0$) is defined by the following equation:

$$P_m = \frac{1}{2m^2 R_{\rm ap}^{2m}} (a_m^2 + b_m^2) \tag{3.6}$$

The generic moments a_m and b_m in polar coordinates are given by :

$$a_m = \int_{r \leq R_{\rm ap}} f_{\rm obs}(x_i, y_i)\, (r)^m \cos(m\theta)\, {\rm dx_i}\, {\rm dy_i} \tag{3.7}$$

$$b_m = \int_{r \leq R_{\rm ap}} f_{\rm obs}(x_i, y_i)\, (r)^m sin(m\theta)\, {\rm dx_i}\, {\rm dy_i}, \tag{3.8}$$

where θ is the position angle of the cluster. The zeroth moment is given by:

$$P_0 = [a_0 \ln R_{\rm ap}]^2 \tag{3.9}$$

and is the total intensity within $R_{\rm ap}$.

In Yuan & Han (2020), the authors compute P_3/P_0. P_3 gives information about bimodality in the surface brightness distribution and is the most appropriate moment to measure asymmetries or the presence of substructures in the ICM (Rasia et al., 2013).

3.3.5 Cold fronts

Chandra sub-arcsecond angular resolution enabled the first observations of cold fronts (Markevitch et al., 2000). CFs are sharp discontinuities observed in the X-ray surface brightness maps (see Markevitch & Vikhlinin, 2007, for a review), where the denser side of the front is colder than the rarified region. The pressure remains nearly constant in a CF. Across the CF, a jump in gas metallicity has been seen in multiple instances, possibly due to enriched low entropy gas being stripped by ram-pressure from satellite galaxies in the rich environment (Markevitch et al., 2000; Simionescu et al., 2010; Ghizzardi et al., 2013). CFs are mainly grouped into two classes according to their formation mechanism: merger-remnant cold fronts (MCF) and sloshing cold fronts (SCF). The collision of two shocks or gas streams can provide an alternative way of forming a cold front (Zinger et al., 2018). MCFs form at the leading edge of the substructure due to ram-pressure confinement of the infalling substructure when a

cold and dense substructure dives through a hotter and more diffuse medium (Markevitch et al., 2000; Vikhlinin et al., 2001). SCFs occur when an off-axis minor merger disturbs the cool core of the main cluster. The disturber inserts angular momentum into the main cluster while crossing it, causing its internal configuration to "slosh" sub-sonically around the gravitational potential. This disturbance creates spiral-like patterns around the cluster core, extending to large radii (Tittley & Henriksen, 2005; Ascasibar & Markevitch, 2006; Laganá et al., 2010; Roediger et al., 2011; ZuHone, 2011; Vaezzadeh et al., 2022). CFs play a significant part in the overall ICM dynamics because of the variety of formation methods and their widespread nature in the ICM. We searched for evidence of CF in the literature when available, as shown in Tab. A.1.

3.4 Radio proxies

The shock waves and turbulence induced by mergers in the ICM often manifest as diffuse radio emissions such as radio relics and halos. These emissions serve as crucial diagnostic tools, providing further insights into the dynamical state of the cluster (for a review see Brunetti & Jones, 2014; van Weeren et al., 2019). Radio relics are megaparsec-sized radio emissions. The shocks travelling through the ICM re-accelerate the cosmic rays (CR) in the ICM. The synchrotron emission observed in radio relics is produced by re-accelerated CRe (electrons). The turbulence injected by the merger often produces large-scale, unpolarised radio sources, known as radio halos, in the cluster centre.

Some clusters in our sample have information in the literature about the presence of radio relics and halos. However, it is important to note that not all the clusters were observed at radio wavelengths and that the observations were carried out at different frequencies and sensitivities. Although recently, relics were observed in pre-merger clusters (Gu et al., 2019; Sarkar et al., 2022), typically, radio halos and relics are evidence of post-merger events. We list the references for the clusters with radio relics and halos in Tab. A.1.

3.5 Combined wavelength proxies

Several studies have shown that the gas disturbance can be inferred by the projected offset between the X-ray peak and the BCG, $\Delta X_{\rm BCG}$ (Sanderson et al., 2009; Katayama et al., 2003; Hudson et al., 2010; Lopes et al., 2018; Zenteno et al., 2020), since major

mergers can cause offsets of dozens of kilo-parsecs ($\sim 939\,h_{71}^{-1}$ kpc for A3376, Hudson et al., 2010), also see Fig. 3.1 as examples. Similarly, other authors have used the separation between the X-ray centroid and the BCG to infer the dynamical state of the clusters. The distance to the X-ray peak was more effective for segregating major mergers since only major mergers can cause the X-ray peak to dissociate considerably from the BCG (De Luca et al., 2021). On the other hand, according to Mann & Ebeling (2012), using the X-ray centroid/peak does not change the results significantly. Rasia et al. (2013) and De Luca et al. (2021) found that a combination of X-ray morphology with dynamical parameters gives a better inference of the cluster's dynamical state. $\Delta X_{\rm BCG}$ suffers from projection effects and is most sensitive to plane-of-the-sky mergers, while dynamical proxies are best for line-of-sight (LOS) interactions.

3.6 Correlation between dynamical state proxies

In Fig. 3.2, we present the Spearman correlation matrix of the main (optical and X-ray) dynamical state diagnostics used in this work and the fractions of infalling galaxies (blue late-type) undergoing RPS within a $0.7\,R_{200}$ aperture (which will be discussed in Sec. 4). The correlations between each pair of diagnostics are given on the top of the matrix diagonal. We see the bi-variate scatter plots at the bottom of the diagonal with the linear model fitted lines. The distribution of each variable is shown on the diagonal as density plots. After running a Gaussian mixture model for the dynamical state parameters, we found that except for $f_{\rm max}$ and the offset between $\Delta X_{\rm BCG}$, which are bi-modal, the dynamical state proxies of our sample of clusters are uni-modal. This agrees with the results from Campitiello et al. (2022) for the distribution of the X-ray morphological parameters of 118 clusters observed with *XMM-Newton*. Overall, most of the clusters present intermediate values for the different diagnostics. Only a few clusters are very relaxed or very disturbed. Perfect correlations or anti-correlations are those close to 1 or -1, respectively. The values close to zero do not correlate. We coloured the strongest correlation (blue) and anti-correlation coefficients (red).

According to the results shown in Fig. 3.2, the parameters that better correlate are the concentration (c) and the centroid shift (ω) (-0.80), followed by the concentration and the asymmetry (α) (-0.71), and the concentration and power ratio (P_3) (-0.68), all of which are derived from X-ray.

The optical parameters do not have strong correlations between them. $f_{\rm sub}$ weakly anti-correlates with $\Delta M_{1,2}$ (-0.24) and exhibits a marginally stronger correlation with

$f_{\rm max}$ (0.36). An outlier drives this apparent correlation, however. Roberts et al. (2018) compared X-ray morphology parameters (asymmetry and centroid shift) with optical dynamical state diagnostics (Anderson-Darling statistic, stellar mass gap between the first and second most massive galaxies, and offset between the most massive cluster galaxy and the luminosity-weighted centre). They found a strong correlation between the centroid shift and the stellar mass gap in their cluster sample. We can compare our results to theirs by assuming that the magnitude gap can be used as a proxy for the mass gap. Their results are at odds with ours since we found a very weak anti-correlation between centroid shift and magnitude gap (-0.14). This can be due to the fact that their sample has a significant amount of clusters ($\sim$ 50%) in a redshift range higher than ours ($>$ 0.07) and these parameters evolve with the redshift. Gozaliasl et al. (2014) found a larger fraction of high-magnitude gap groups at lower redshifts. Furthermore Jeltema et al. (2008) found a significant increase in the average centroid shifts with redshift.

There are many obstacles in identifying dynamical states using the most diverse techniques presented here. The in-homogeneity in clusters that have good quality data in the same X-ray telescope, such as *Chandra* and *XMM-Newton*, considerably reduces the sub-sample of clusters for which we can make the comparison shown in Fig. 3.2. Other factors that impacted the size of this sub-sample were the lack of photometric and mainly spectroscopic coverage for large fractions of a cluster's R_{200} and the spectroscopic completeness.

3.7 Defining a dynamical state sequence

In the previous section, we saw how different diagnostics for cluster dynamical states could yield different results, with the X-ray proxies being more consistent for this sample. In this section, we take a closer look at all the available data for the X-ray sample to define a discrete combined classification of the clusters that tentatively reflects the time sequence of the interaction and/or its intensity. At the same time, we use this classification to define, for each case, the centre to consider in our analysis (Sec. 4). To this end, we constructed a flowchart, shown in Fig. 3.3, which yields the five possibilities for the cluster's dynamical states and centres described below. We show examples of the X-ray maps of each of these dynamical states in Fig. 3.4. The centre choice is done by comparing the positions of the BCG with the X-ray peak and checking whether there are secondary X-ray peaks and if radio relics are seen. If mul-

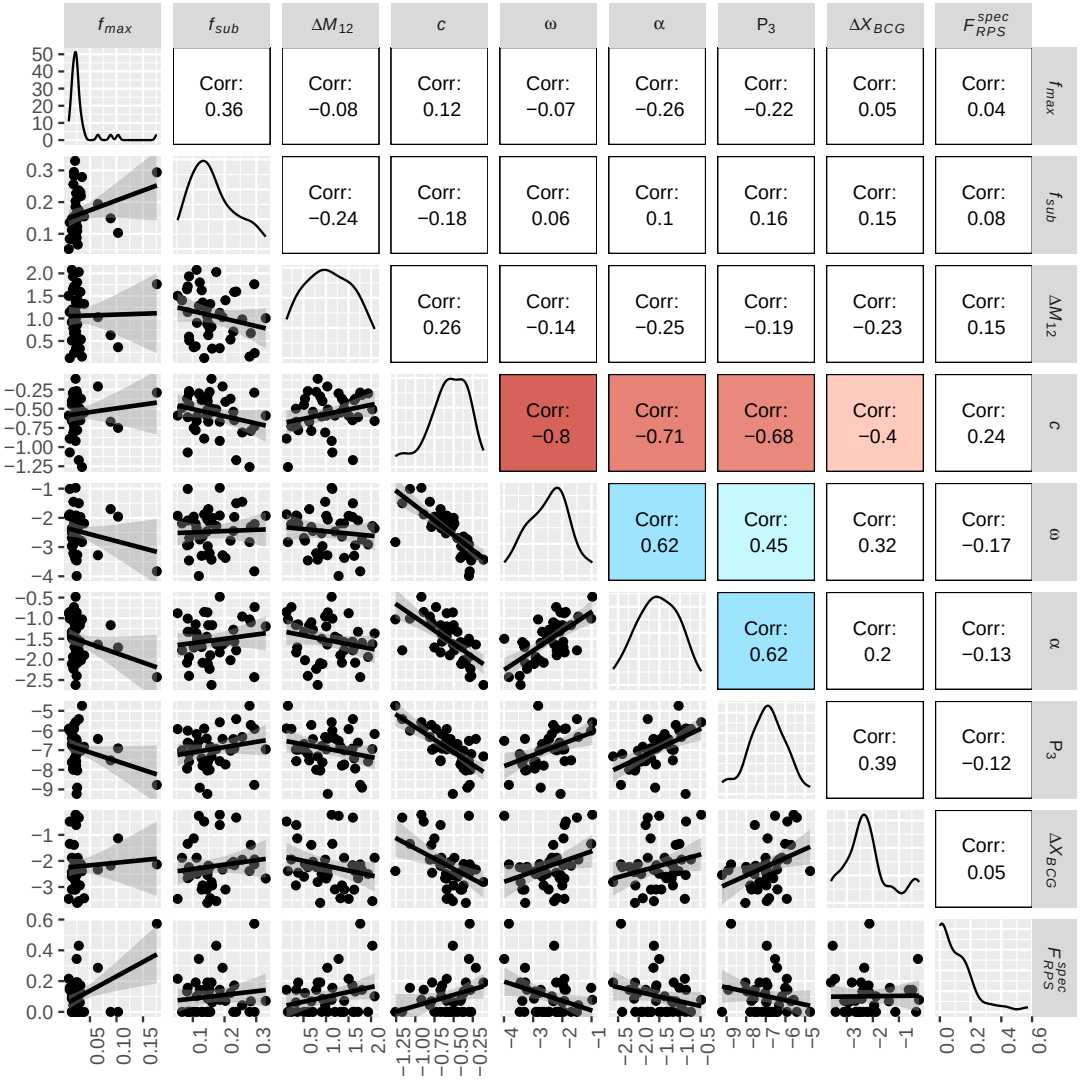

Figure 3.2: Correlation matrix of the main dynamical state diagnostics used in this work and the fractions of ram-pressure candidates within a $0.7\,R_{200}$ radius. The different proxies are explained in Sec. 3, and the last column is discussed in Sec. 4.2. The panels on the top of the diagonal show the Spearman correlation coefficient. The coloured panels show the most significant correlations (blue) and anti-correlation (red). The Spearman correlation varies from -1 to 1. A strong correlation is close to 1, a strong anti-correlation is close to -1, and values around 0 do not correlate. The panels on the diagonal show the distributions of each proxy, while the ones on the bottom of the diagonal show the bi-variate scatter plots (grey dots show each cluster in our sample) with linear fits (black lines). There is no clear separation between relaxed and disturbed clusters. RPS fractions do not correlate with the dynamical state proxies used in this work.

tiple X-ray structures are visible, the brightest galaxy in each structure is considered a BCG, leading to multiple "BCGs" in a single cluster.

Pre-merger: This class of clusters has multiple and comparable size X-ray clumps, each with a matching BCG (within $1'$). We based the choice of this radius on the fact that only four BCGs in our sample have an effective radius greater than $1'$. In our pre-merger classification, the X-ray clumps are separated by less than R_{200} and $3\sigma_{cl}$ in velocities (using the most massive cluster radius and velocity dispersion as reference). Usually, these pre-merging clusters do not present diffuse radio emissions. However, radio shocks have been observed in the pre-merger state of the cluster pair 1E 2216.0-0401/1E 2215.7-0404 (Gu et al., 2019) and recently in Abell 98 (Sarkar et al., 2022). The motivation for separating these clusters from the other interacting clusters comes from the fact that we are interested in investigating whether pre-merging environments can enhance RPS candidate fractions. We use the midpoint between the two BCGs as the centre of the pre-merger systems in our analysis as an attempt to measure the enhancement caused by the ICM compression between two clumps.

Relaxed: The X-ray surface brightness map is concentrated, single-peaked, and regular, and the X-ray peak coincides with the BCG (within $1'$). In this case, we use the BCG as the centre. There is a second case of relaxed clusters where the BCG and the X-ray peak coincide within the $1'$ criteria, but the X-ray morphology shows more than one clump of comparable sizes, with BCGs separated by more than R_{200} and/or velocity differences larger than $3\sigma_{cl}$. In these cases, we treat them as two separate relaxed structures and use each one's BCG as its centre.

Mildly-interacting: The X-ray surface brightness morphology of the cluster is still concentrated, but there is a mild amount of optical and/or X-ray substructures (subclumps) or disturbances (such as an X-ray spiral/sloshing pattern in the core). Since the interactions are usually small in those cases, the BCG and main X-ray peak are within $1'$ of separation, and we use the BCG as the centre.

Interacting: When the X-ray emission of the cluster is extended, distorted or multi-peaked (but clumps do not have a clear separation), we classify the cluster as interacting and use the BCG as the centre. When a cluster has multiple comparable X-ray clumps and no matching BCGs (within $1'$ of the X-ray peak) for those clumps, we classify it as interacting and use the central bright galaxy near the main peak as the centre.

Post-merger: If the cluster is undergoing a significant merger and also shows the presence of X-ray shocks or diffuse radio emission (relics or halo), we consider it a

post-merger. In this case, we use the midpoint between the BCGs as the centre, similar to what was done for the post-merger system Abell 3376 by Kelkar et al. (2020). The last panel of Fig. 3.4 shows an example of a cluster with radio relics.

We classified three clusters as pre-mergers, twelve as relaxed, nineteen as mildly interacting, five as interacting, and five as post-merger.

In Fig. 3.5, we plot the X-ray (left) and optical (right) dynamical state diagnostics with the best correlation coefficients, colour-coded by the visual dynamical state sequence performed in this section. Clusters with literature information (see Tab. A.1) for radio relics, halos, sloshing, and merger cold fronts are highlighted. Note that in the right-hand panel (optical proxies), there are more clusters than in Fig. 3.2, where we could only use clusters that were simultaneously in the X-ray and spectroscopically complete samples to be able to directly compare against X-ray proxies[3]. Overall, Fig. 3.5 shows that our flowchart dynamical state sequence best agrees with the X-ray diagnostics. This is expected since the flowchart was mainly based on some X-ray-dependent criteria, but it also adds optical information to this kind of diagnostic, making explicit, for example, that the cluster A3716, an outlier in the X-ray diagnostics plot, is a pre-merger cluster.

The most disturbed clusters should be naturally found in the upper right corner of the left-hand plot of Fig. 3.5, with high X-ray centroid shift and lower concentration. In fact, Rasia et al. (2013) found that radio relics/halos tend to be located in this quadrant, which our sample also shows. Another interesting feature is that clusters with SCF fall in this plot's lower-left "relaxed" quadrant. This is unsurprising, considering that SCFs are caused by minor interactions relative to a cluster merger. In the right-hand panel of Fig. 3.5, the situation is less clear, as the optical proxies for cluster dynamical states are not as well correlated with each other nor the flowchart dynamical state sequence. Clusters with radio relics prefer regions with smaller magnitude gaps (expected in cluster mergers), and those with SCF are more scattered but with a predominant presence towards the relaxed region, as defined by the line of Raouf et al. (2019).

[3]Note that adding the missing clusters in Fig. 3.2 only causes a minor change in the distribution shape and correlation coefficients for the optical proxies.

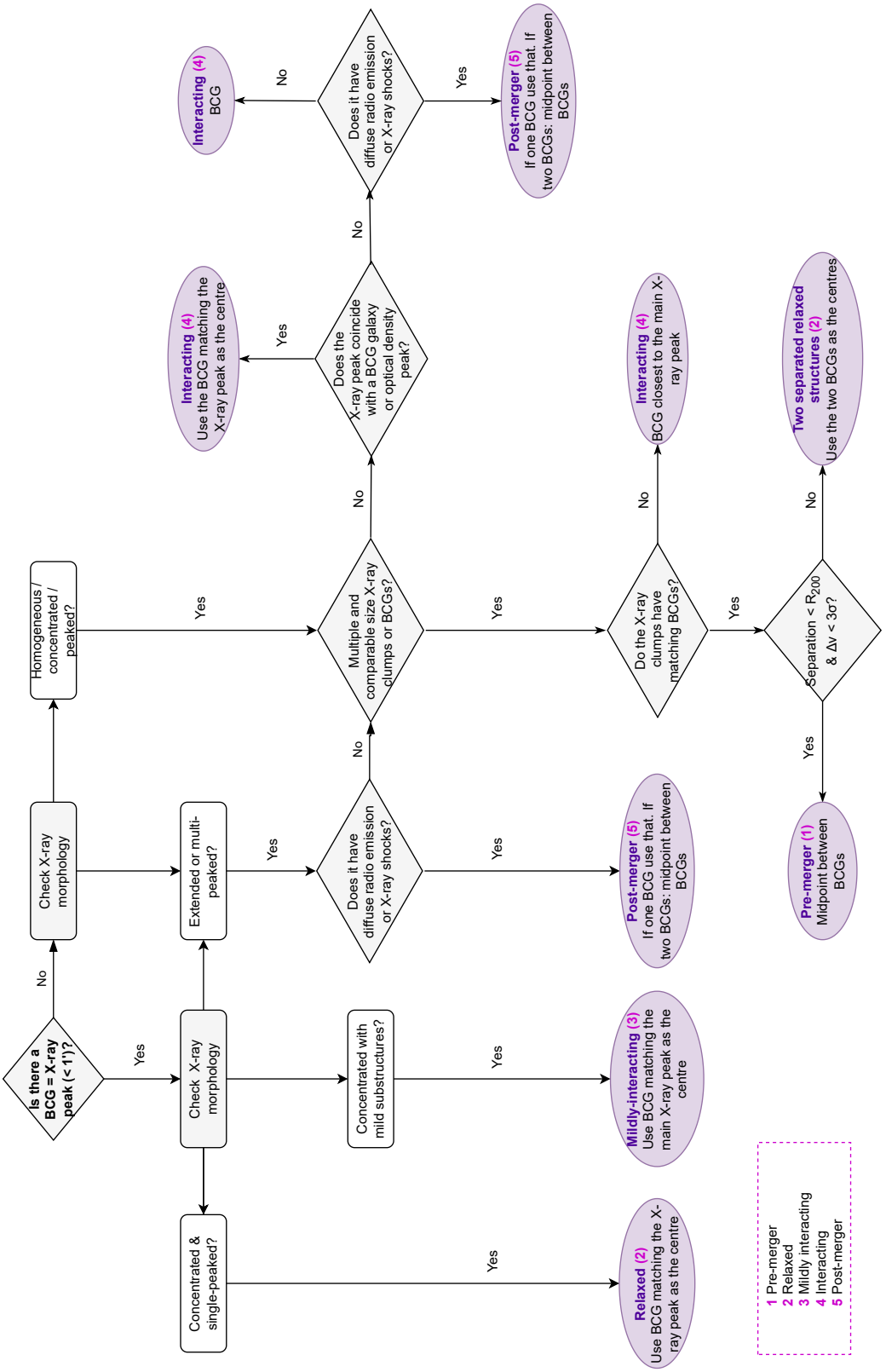

Figure 3.3: Flowchart used to classify the dynamical state sequence and define cluster centres tentatively. This classification was only done for clusters with X-ray data.

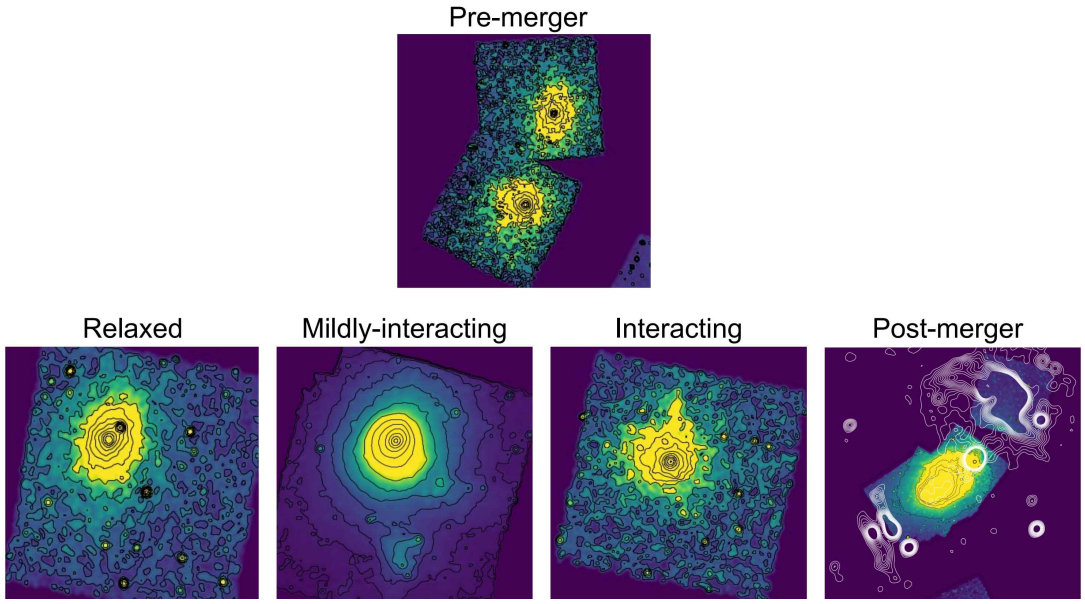

Figure 3.4: X-ray emission of clusters of different dynamical states. The pre-merger class is a particular case since it cannot be placed appropriately for the dynamical state sequence. In the lower panels, clusters are ordered from the most relaxed class to the most disturbed and the post-mergers. Radio relics are shown in white contours.

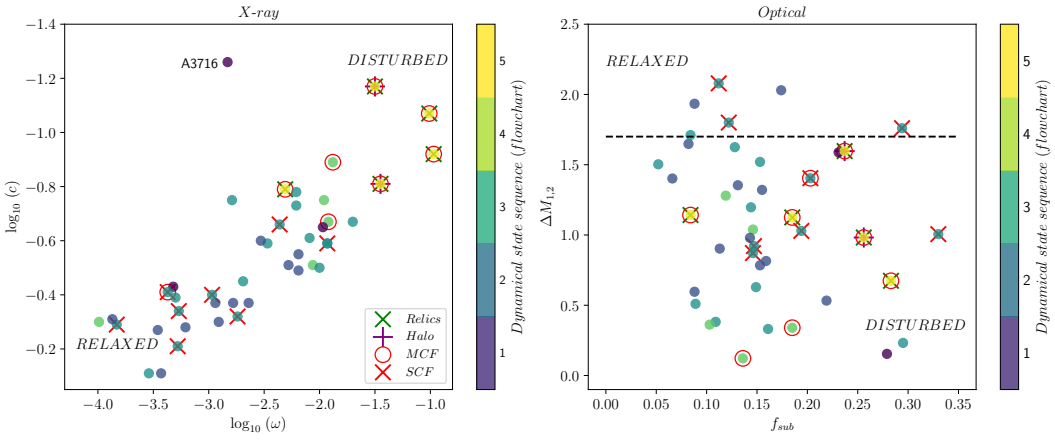

Figure 3.5: Left: Concentration vs. centroid shift of clusters in the X-ray sample coloured by our dynamical state sequence defined in the flowchart. Disturbed clusters have large centroid shifts and small concentrations. The disturbance of the clusters increases from the bottom left quadrant to the top right quadrant. Right: Magnitude gap vs. $f_{\rm sub}$ coloured according to the dynamical state sequence from the flowchart. The black dashed line is the Raouf et al. (2019) criteria to segregate the relaxed clusters above it. Disturbed clusters have a small magnitude gap and large $f_{\rm sub}$. The green and red "X" show radio relics and SCFs, respectively. Purple crosses show the radio halo clusters. The red open circles show the MCFs clusters.

CHAPTER 4

The effect of cluster dynamical state on ram pressure stripping

In this chapter we are able to understand how a cluster's dynamical state influences RPS. We compute the incidence of stripped candidates in the P16 sample by measuring the fraction of galaxies undergoing RPS relative to the infalling population, which we characterise as blue late-type galaxies. These gas-rich galaxies are likely the most susceptible to RPS. Also, they were previously used in V22 to obtain similar RPS fractions. Furthermore, we computed the RPS candidate fractions considering two samples. We first considered the (larger) photometric galaxy sample, and to account for the fact that we do not have cluster memberships for the whole photometric sample, we performed a correction for field contamination (Sec. 4.2). Then, to test if the lack of cluster memberships was biasing our results, we re-did the analysis considering the (smaller) spectroscopic galaxy sample, where we can select cluster members with confidence and exclude all the non-members in the computation of the RPS candidate fraction (Sec. 4.3).

4.1 Galaxy colors

In Fig. 4.1, we show how we define the blue galaxies we used in this work. We fit the distribution of $B - V$ colour with two Gaussians in separate M_V bins. The peak value

of the redder Gaussian was taken as the midpoint of the red sequence, and the scatter was taken as the standard deviation. This was repeated across four magnitude bins, and then we used the line 1-σ below the resultant linear fit to separate red sequence galaxies from blue galaxies. The equation of the derived line is:

$$(M_B - M_V) = -0.037 \times M_V + 0.046 \tag{4.1}$$

Galaxies with a $B - V$ colour bluer than this relation are considered blue. This method is similar to that used in Crossett et al. (2017, 2022).

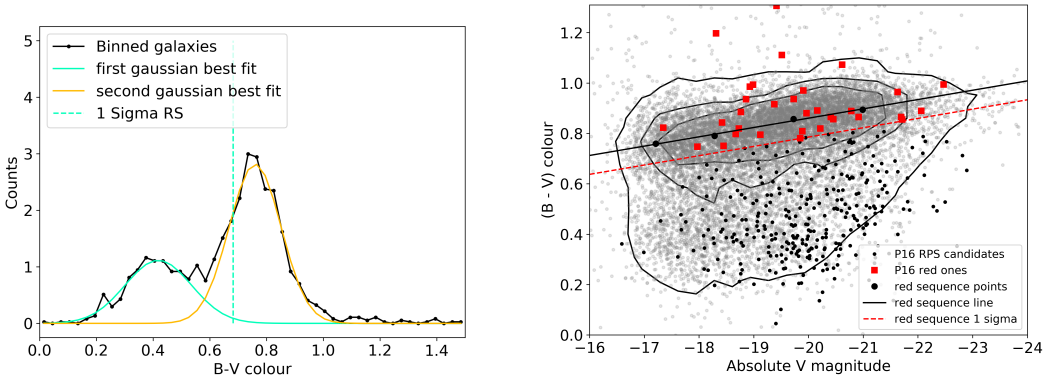

Figure 4.1: Left panel: Two Gaussian fitted to the colour distribution of the OmegaWINGS members. The peak of the yellow Gaussian was used to define the red sequence. The blue dashed line shows 1-σ below the red sequence. Galaxies to the left of that line are defined as blue. Right panel: Colour magnitude diagram of the OmegaWINGS and WINGS members. Large-filled black circles show the Gaussian fit result of the four magnitude bins used in the fitting process. Some P16 candidates (red squares) lay above the 1-σ and are disregarded from our analysis.

4.2 Photometric RPS fractions

To compute the RPS candidate fractions from the photometric galaxy sample, we counted the number of RPS candidates that are blue late-type galaxies within 0.7 R_{200}, $N_{\rm RPS}^{\rm BSp}$ (see justification in Sec. 2.1.1). Then, we measured the total number of blue late-type galaxies in the same area, $N^{\rm BSp}$. To account for the field contamination, we subtracted the expected number of blue late-type galaxies in the field within the same area. The percentage of blue late-type galaxies in the field was estimated following the method used in Fasano et al. (2015). Similar to them, we used a comparison field sam-

ple of galaxies from the Padova-Millennium Galaxy and Group catalogue (PM2GC, Calvi et al., 2011, 2012), which encompasses a spectroscopic sample of galaxies at $0.03 \leq z \leq 0.11$ brighter than $M_B = -18.7$. The PM2GC sample comes from the Millennium Galaxy Catalogue (Liske et al., 2003; Driver et al., 2005), a deep B-band equatorial survey, complete down to $B = 20$ representative of the general field population in the local Universe. Utilising PM2GC data has the benefit that both the imaging instrumentation [Wide Field Camera (WFC) at Isaac Newton Telescope (INT)] and the technique used to determine the morphological types [MORPHOT] are identical for PM2GC and WINGS galaxies. This ensures that the two samples are fully morphologically consistent. We then computed the fraction of blue late-type galaxies brighter than $V = 17.77$ in the field, which is ~ 40 per cent, and we used this value to correct the cluster $N^{\rm BSp}$.

Photometric RPS counts ($N^{\rm BSp}_{\rm RPS}$) were also corrected for field contamination. In the comparison field sample for the WINGS survey, PM2GC, only 6.7 per cent of the blue late-type with no gravitational interaction flags were classified as RPS candidates by P16. Poggianti (in prep) found that 86 per cent of the RPS candidate galaxies identified in clusters are genuine RPS. Therefore, we assume a similar success rate in this sample and consider 14 per cent of the candidates not genuine. A deduction of 0.14 is applied to the photometric fractions, to account for galaxy candidates that may not be undergoing ram-pressure stripping. We had a total of 39.6 blue late-type RPS candidates and 430.3 blue late-type galaxies, after correcting for the field contamination, in the 52 clusters of this sample (19 clusters had their photometric RPS fractions equal to zero). Equation 4.2 defines the field-corrected photometric fractions of RPS candidate galaxies tabulated in Tab. A.1

$$F^{\rm phot}_{\rm RPS} = \frac{N^{\rm BSp}_{\rm RPS}(1 - 0.067 - 0.14)}{N^{\rm BSp}(1 - 0.4)} \tag{4.2}$$

4.3 Spectroscopic RPS fractions

To check if our photometric analysis was leading us to a false result, we also computed the spectroscopic RPS candidates fraction. In this analysis, we consider only confirmed spectroscopic members and clusters with spectroscopic completeness higher than 50 per cent. We have a total of 47 clusters in the spectroscopic sample.

The spectroscopic RPS fractions $F^{\rm spec}_{\rm RPS}$ were calculated by dividing the number of blue late-type RPS member candidates $M^{\rm BSp}_{\rm RPS}$ by the total number of blue late-type

members $M^{\rm BSp}$ in that same aperture of $0.7\,R_{200}$, as described in Eq. 4.3. Overall we had 364 blue late-type members and 30.1 blue late-type RPS candidates (GASP survey success rate-corrected) tabulated in Tab. A.1:

$$F_{\rm RPS}^{\rm spec} = \frac{M_{\rm RPS}^{\rm BSp}(1-0.14)}{M^{\rm BSp}} \tag{4.3}$$

This method is similar to the method applied in V22, with the exception that we restricted the physical radius and only used spectroscopically complete clusters in our analysis.

In Fig. 4.2, we compare the distributions of photometric and spectroscopic RPS candidates fractions. Both distributions reach similar values and are comparable. In fact, the mean RPS candidate fraction of the photometric sample (12 ± 2 per cent) is consistent with the spectroscopic one (11 ± 2 per cent). We computed the binomial confidence intervals following Cameron (2011). The method employed for calculating our confidence intervals is specifically designed for smaller fractions and yields reliable results for sample sizes ranging from small to intermediate. All uncertainties reported in this paper will be presented at a confidence level of c = 0.683, which is equivalent to 1σ. Despite a few outliers, we found that $F_{\rm RPS}^{\rm spec}$ fall close to a $1:1$ ratio with the photometric fractions. The distributions of the photometric and spectroscopic RPS fractions are very similar (see Fig. 4.2).

Our main goal was to see how the RPS fractions compared with cluster dynamical state, so we started by comparing the $F_{\rm RPS}^{\rm spec}$ with the eight different proxies for cluster dynamical state described in Sec. 3.2 and obtained no clear correlation, as can be seen in Fig. 3.2 through the low correlation coefficients given between $F_{\rm RPS}^{\rm spec}$ and the other variables. Fig. 4.3 shows this result in more detail, with X-ray (left) and optical (right) dynamical state diagnostics similar to Fig. 3.5, but this time colour-coded by $F_{\rm RPS}^{\rm spec}$. We use spectroscopic fractions because they do not need correction for the field contamination, as they do not need statistical correction for the field contamination. The lack of correlation between the $F_{\rm RPS}^{\rm spec}$ fractions and the dynamical state of the cluster is still visible. We can even see that the highest RPS fractions sometimes appear in the most relaxed quadrant (bottom left) of the scatter plot on the left panel. We note that the results shown in Fig. 4.3 and Fig. 3.2 do not significantly change when using $F_{\rm RPS}^{\rm phot}$ instead of $F_{\rm RPS}^{\rm spec}$.

In Fig. 4.4, we further study how the (photometric and spectroscopic) RPS fractions vary along the visually-defined dynamical state sequence. Although the spec-

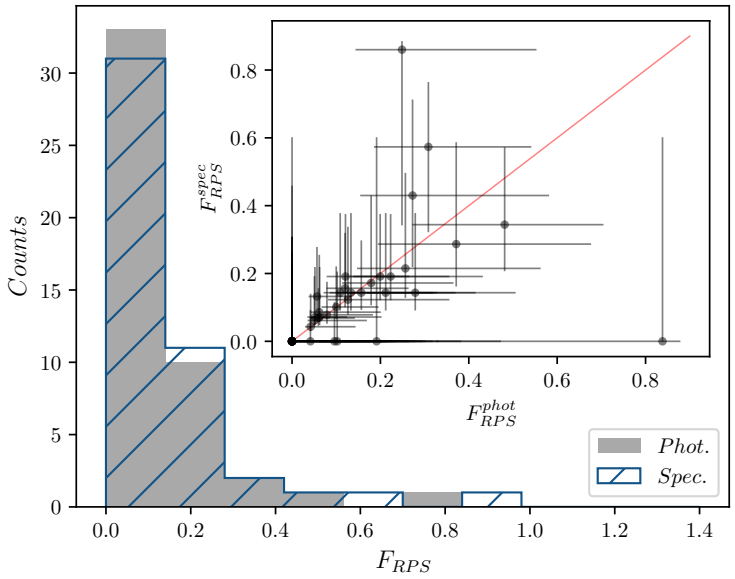

Figure 4.2: Comparison between photometric and spectroscopic RPS candidates fraction distributions. The grey histogram shows the distribution of the photometric RPS candidate fractions, while the blue hashed histogram shows the distribution of the spectroscopic RPS candidate fractions. The subplot in the top right corner compares photometric and spectroscopic RPS fractions for the common clusters in both samples. The 1:1 reference line is shown in red, and the binomial uncertainties are shown as black error bars.

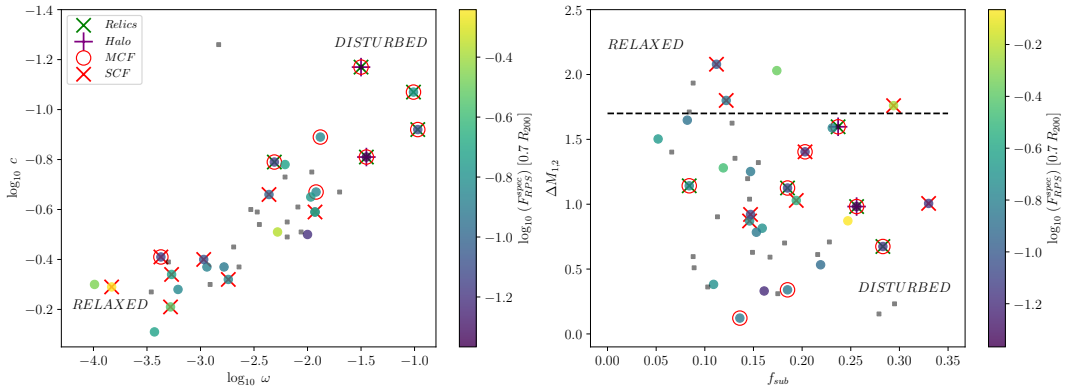

Figure 4.3: The same dynamical state diagnostics as in Fig. 3.5, this time coloured according to the logarithm of the **spectroscopic** fractions of galaxies undergoing ram-pressure stripping. Clusters with $F_{\mathrm{RPS}}^{\mathrm{spec}} = 0$ are shown as black squares. Only clusters that are spectroscopically complete are plotted. The highest RPS candidate fractions very often lie on the more relaxed quadrant.

troscopically complete cluster sample is smaller than the one used for the photometric analysis, the RPS fraction distributions are similar. Interestingly, when using the visual classification for the dynamical state in a sequence, we find a constant RPS candidate fraction from the "pre-merger" state to the "relaxed" and "mildly interacting" ones, and hints of an increase of the RPS candidate fraction for "interacting" clusters, followed by an equally mild decrease of the fraction for the "post-merger" class. The possible RPS fraction enhancement in the interacting class and subsequent decay in the post-merger class could be interpreted as a consequence of either the rapid timescales involved in the stripping process in a post-merging environment or the searched area not covering the radius where the bulk of RPS happens in these violent environments. Unfortunately, the sample is too small to allow drawing any significant conclusion from it. A Kruskal-Wallis H test (Kruskal & Wallis, 1952) showed that there was no statistically significant difference in RPS fractions between the different dynamical state classes.

4.4 Discussion

In this paper, we have studied the influence of cluster buildup on the quenching of galaxies via RPS, using, for the first time, a sizeable homogeneous sample of stripped galaxies in a large sample of clusters. In particular, we computed the incidence of RPS candidates relative to the infalling blue late-type population within a fixed physical radius for 52 clusters with different dynamical states, determined using a variety of X-ray and optical proxies. We found no clear correlation with any of the dynamical state proxies used. The lack of correlation is seen when using photometric data (and correcting for field contamination) as well as when using confirmed spectroscopic members only. However, after visually classifying the sample in a dynamical state sequence, we observe a constant fraction going from "pre-mergers" to "relaxed" and "mildly interacting" clusters, and a possible (mild) enhancement in the RPS candidate fractions of the interacting clusters, which then goes back to the nominal value for the "post-merger" class (see Fig. 4.4). The deviations are not statistically significant, but if they were to be confirmed, they point to an enhancement in the RPS (post-processing) in ongoing cluster mergers, which occur on a fast timescale, but there are many caveats involved, discussed below.

There could be several explanations for the mild RPS increase in the interacting sample with respect to the other classes, in particular, the post-merger bin, which are

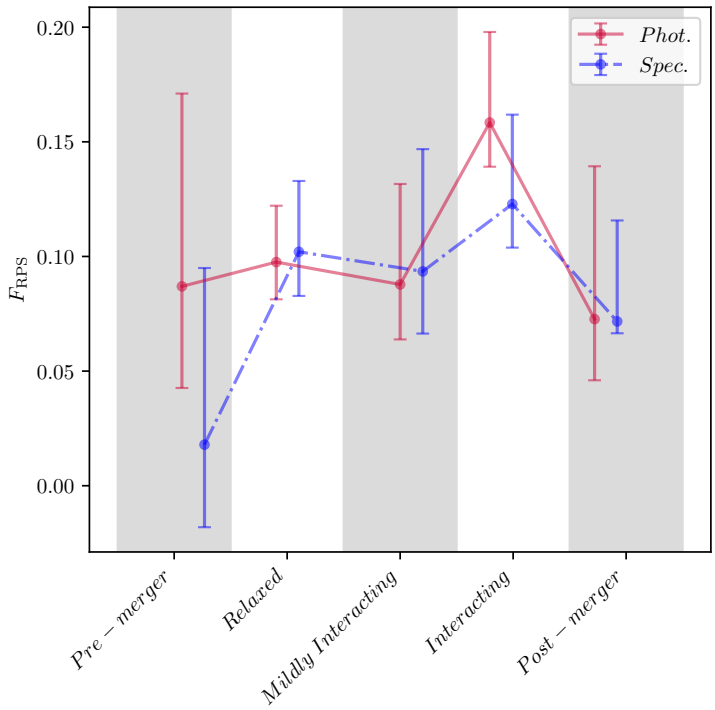

Figure 4.4: Fraction of RPS candidates relative to the infalling population as a function of the dynamical state sequence defined visually (see flowchart). The dashed blue and the solid red lines show the spectroscopic and photometric RPS candidate fractions, respectively. The 1σ binomial confidence intervals are shown. There is a possible enhancement in the RPS fractions in the interacting class, but it is not statistically significant.

associated with the many challenges in the study of galaxy populations in merging clusters, listed and discussed in the following:

Cluster coverage: In significantly disturbed clusters, mergers or post-mergers, much of the action (including RPS) could be happening outside the core of the cluster ($r > 0.7\,R_{200}$), where we do not have homogeneous data coverage. Only in clusters that are merging along the line of sight (LOS) we could see the merger close to the core.

LOS mergers are generally better traced by the optical diagnostics, such as $f_{\rm sub}$ and $\Delta M_{1,2}$. The fact that we do not find a clear correlation between the cluster dynamical state and the RPS candidates incidence using this kind of diagnostics plays against this hypothesis.

Cluster size: To compare the incidence of any galaxy population between clusters, we need to search around the same physical radius (e.g R_{200}). However, in disturbed clusters, the physical size measurement can be unreliable (and has a different meaning), as its often derived from the dynamical mass (i.e. velocity dispersion). A more reliable alternative to estimate cluster mass in these cases is through gravitational lensing, which is beyond the scope of this manuscript.

Cluster mass: Before drawing conclusions about the influence of the cluster dynamical states in the incidence of RPS, it is essential to check for possible correlations with cluster mass. RPS depends on the density of the ICM and is quadratically dependent on the velocity of the galaxies relative to the ICM, and both those quantities are higher in massive clusters, so one can naively expect a higher incidence of RPS galaxies in more massive clusters. However, there are contradictory results in the literature.

In recent work, Roberts et al. (2021a,b) identified jellyfish galaxies in ∼500 low-mass galaxy groups and 29 clusters ($M_{180} \sim 10^{12.5}$ to $\sim 10^{15}\,M_{\odot}$) using radio continuum data. They found a factor of 2 increase in the fraction of stripped galaxies with respect to the star-forming galaxy population from groups to clusters but with significant scatter within the cluster sample.

Wang et al. (2020) used HI-detected galaxies from the Arecibo Legacy Fast ALFA (ALFALFA) survey (Haynes et al., 2018) in 26 X-ray-selected clusters ($M_{200} \sim 3.8 \times 10^{13}$ to $\sim 1.3 \times 10^{15}\,M_{\odot}$) to estimate the ram-pressure strength at different radii of their cluster sample. They found that the RPS strength depends on the cluster mass and the projected phase space diagram position. They also computed the fractions of HI-rich galaxies affected by RPS. Their RPS fractions are higher in the massive clusters ($M_{200} > 2 \times 10^{14}\,M_{\odot}$). They also showed that galaxies could undergo RPS at larger radii in massive clusters, in agreement with other studies (e.g. Jaffé et al., 2018; Gullieuszik

et al., 2020; Pallero et al., 2019, 2022).

In the optical, V22 found no correlation between the fraction of RPS galaxies relative to the infalling population of blue spirals and the cluster velocity dispersion, σ_{cl}, or the cluster X-ray luminosity, L_X. This could, in principle, be affected by interacting clusters with unreliable masses. To account for this, in Fig. 4.5, we investigated whether the spectroscopic fractions of the RPS candidates we have computed show any dependence on the halo mass and X-ray luminosity measured in the 0.1 – 2.4 keV energy band for *ROSAT* data in Ebeling et al. (1996, 1998, 2000) excluding interacting clusters. In fact, we only consider the relaxed and mildly-interacting clusters from our flowchart dynamical state sequence. Even when cleaning the sample, we still do not find a correlation between the incidence of RPS candidates and cluster mass.

In summary, our optical quantification of the incidence of RPS galaxies in clusters does not show the same trends with cluster mass as studies in radio wavelengths. Low-frequency radio continuum can be more sensitive to RPS than the optical, as the non-thermal interstellar medium components appear more affected by RPS (Roberts et al., 2021a,b; Ignesti et al., 2022, 2023). Another explanation for the discrepancy between the wavelengths is that optical selection favours galaxies with star formation in the tail. Our sample selection might underestimate the total number of galaxies. Some galaxies at peak stripping show a lack of star formation in the tail (e.g. Boselli et al., 2016a; Laudari et al., 2022). Additionally, optical wavelengths only allow us to observe galaxies that had time to form new stars from the stripped gas (e.g. Poggianti et al., 2019; Gullieuszik et al., 2020). Our results are in line with Gullieuszik et al. (2020), who used MUSE data from the GASP survey to analyse the dependence of the SFR in the tails of stripped gas on the galaxy and clusters' properties, including cluster mass. They conclude that the interplay between all the parameters involved is complex and that there is no single dominant parameter impacting the observed SFR amount. Their conclusion could be related to our findings on the global RPS candidate fractions.

Cluster members: Regarding the previous point, the disturbed clusters also challenge defining true members of very close pre-mergers. We dealt with this by treating systems that are separated by less than R_{200} as if they were the same, but we expect some contamination from interlopers.

Cluster centres: In relaxed clusters, the X-ray peak, centroids, BCG, and density peak are close to each other. However, during merging events, the galaxy density peak can be very displaced from the X-ray centroid (~ 0.2 Mpc for the bullet cluster, Clowe et al., 2006). In this work, we used the symmetry of the cluster system to determine its

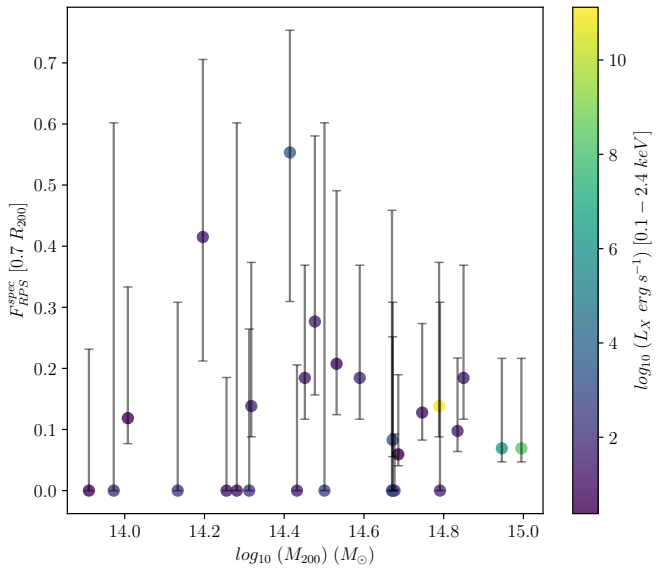

Figure 4.5: Cluster RPS spectroscopic fractions vs. halo masses coloured by the cluster X-ray luminosity measured in the 0.1 – 2.4 keV energy band for *ROSAT* data in Ebeling et al. (1996, 1998, 2000). In this plot, we are showing only the relaxed and mildly-interacting clusters. Massive clusters are not the ones with the highest RPS candidate fractions. The 1σ confidence interval is computed as in Cameron (2011)

centre. We assumed that the midpoint between the two central brightest galaxies in a cluster system represents the system's centre of mass better than the X-ray peak or the BCG.

Galaxy populations: Using HST images for a few intermediate-z clusters, previous studies such as Roman-Oliveira et al. (2019); Owers et al. (2012); Ebeling & Kalita (2019); Rawle et al. (2014) have focused on the absolute number or RPS features strength of stripped galaxies without accounting for the size of this population relative to the infalling blue late-type galaxies or the physical size of the explored region. On the contrary, in our study, we compute for the first time in a homogeneous cluster sample the fraction of galaxies undergoing RPS relative to the infalling population in a fixed aperture, normalised by cluster size. V22 estimated similar RPS candidate fractions using the P16 sample and additional candidates in the same clusters. The main difference with our study is that they did not take into account the cluster size or limited their sample to clusters with spectroscopic completeness > 50 per cent, as we did in this work. Also, we only considered P16 galaxies and not the new candidates since these were searched only among spectroscopic members, and we used photometric and spectroscopic fractions, which would have been difficult to compare otherwise. Additionally, part of their new RPS candidates are unwinding spirals. When the P16 sample was compiled, the unwinding effect of ram-pressure stripping on the spiral arms of galaxies was still unknown (Bellhouse et al., 2021). V22 have found that about 35 per cent of the total population of non-interacting blue late-type cluster galaxies are undergoing RPS. When using only the P16 candidates they obtain $\sim 15-20$ per cent. Despite the different methods, this is close to the spectroscopic and photometric RPS fractions we measure within $0.7R_{200}$, which are $\sim 11-12$ per cent. Given that V22 found new RPS candidates in the same clusters, our fractions can be considered lower limits.

CHAPTER 5

The effect of pre-processing in ram pressure stripping

In previous Chapters (3 and 4; see also Paper I), we investigated the impact of cluster dynamical state on ram-pressure stripping with the goal of finding signatures that can be linked to post-processing due to cluster mergers. We used the largest sample of optically selected RPS candidates in the local Universe from Poggianti et al. (2016, P16 hereafter), located in 71 different clusters. We found a weak enhancement of the fraction of RPS candidates in visually classified interacting clusters, but no clear correlation between the cluster dynamical state diagnostics commonly used in the literature and RPS fractions.

In this Chapter, we further investigate the effect of galaxy pre-processing inside substructures and filaments. To do that, we compute fractions of RPS candidates relative to the infalling population of cluster galaxies in- and outside substructures. We use the same sample of RPS candidates (but only spectroscopically confirmed members) and clusters, with additional RPS candidates from Vulcani et al. (2022, V22 hereafter), a complementary study that searched for additional RPS candidates among confirmed spectroscopic members in the same cluster sample of P16. The addition of (V22) is possible given that we only consider in our analysis spectroscopically confirmed cluster members.

5.1 Substructure identification

To define substructures of galaxies within the clusters, we use the DS+ technique, an enhanced DS test described in Section 3.2.1, to identify substructure member galaxies.

We ran the DS+ test on 66 WINGS clusters with spectroscopic data that had at least 20 members. 41 per cent of the cluster members were assigned to substructures by DS+ for a total of 64 clusters that contained substructures. These clusters were selected based on having spectroscopic data from the WINGS/OmegaWINGS surveys and being common to the datasets of B17 and P16. This analysis was not limited to radius, using all the coverage of the spectroscopic data and very often reaching clustercentric distances larger than 0.7 R_{200}. In this chapter, we use the substructures obtained with a smoothed observed velocity dispersion profile in the non-overlapping mode of DS+ (For a detailed description, see, Section 3.2.1 and B17).

As an example of the substructure analysis, in Fig. 5.1, we show Abell 3880, a galaxy cluster classified as relaxed in Paper I. We show this cluster in particular because four RPS candidates (JO182, JO183, JO181, and JO188) are fairly aligned with the BCG major axis, and some candidates are in substructures. When inspecting the distribution of the RPS candidates in the clusters the appendix B, we noticed that in some other the RPS candidates seemed to align with the BCG major axis, which is a proxy for the direction of the main filamentary structure (e.g., Binggeli, 1982; Chu et al., 2021). The most striking example is perhaps IIZW108, where the jellyfish galaxy (JO206) is infalling from the direction of a filament in addition to head-tail[1] (HTII) (Müller et al., 2021).

Figure 5.2 shows the galaxy cluster IIZW108. The red-filled circles show a small optical substructure near the core of IIZW108 found by DS+ method and the purple-filled circles correspond to a substructure located more in the filament. The ICM is represented by the black contours (X-rays), and the galaxy density is seen as blue contours (tracing the spectroscopic members: crosses). The galaxy density shows an elongated profile towards the southwest, which is also aligned with the slight elongation seen in X-rays and, interestingly, with the BCG major axis. The possible relation between RPS candidates, substructures, and BCG alignment will be investigated in Sec. 6.

[1] A head-tail galaxy is a type of radio galaxy that exhibits a distinctive morphology with a bright "head" and a trailing "tail" of radio emission. This galaxy is generally observed in clusters and indicates the interaction between the galaxy and the surrounding medium. The ram pressure as the galaxy moves through the ICM bends the jets, creating the head-tail appearance.

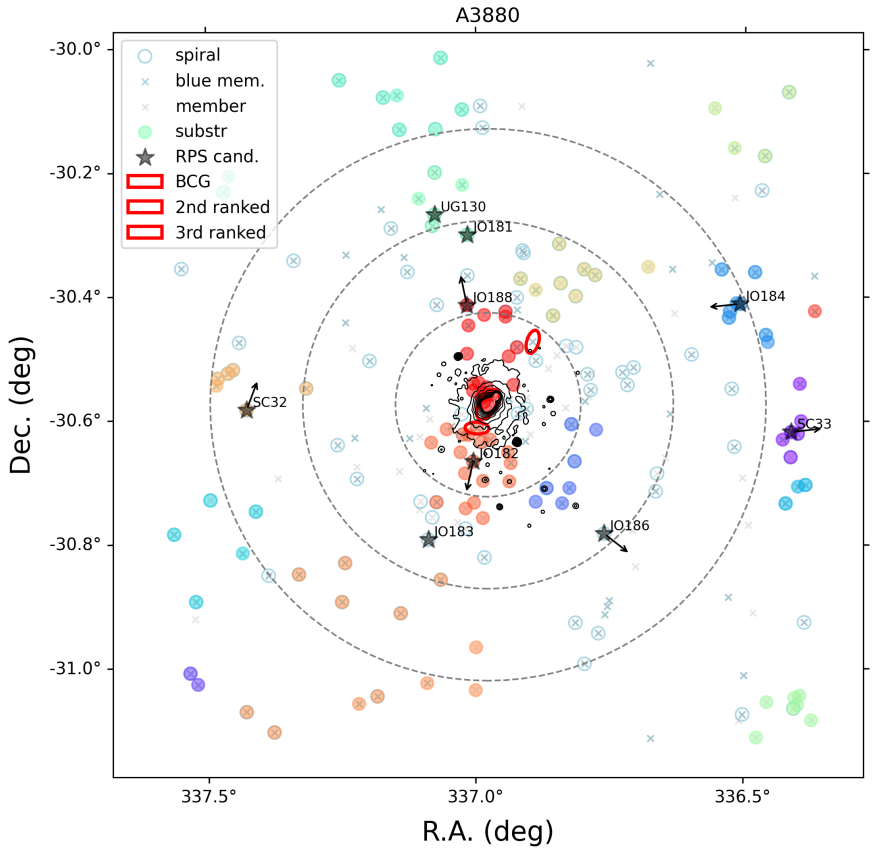

Figure 5.1: Spectroscopic members in the central region of A3880. RPS candidates are shown as filled black stars. The arrows indicate the direction of the tails in the RPS candidates, which, in principle, point in the opposite direction of movement (Salinas et al., 2024). The filled-coloured circles represent the substructures identified in B17. The blue x's and open circles represent blue and spiral galaxies, respectively. Black contours highlight the X-ray emission, and red ellipses show the positions and orientations of the three brightest galaxies. The dashed black circles show 0.5 R_{200}, R_{200}, and 1.5 R_{200}, respectively. In this cluster, 1/4 RPS candidates are outside substructures (UG130 is an unwinding candidate from V22, which is not confirmed to be disturbed by RPS)

5.2 RPS candidate fractions in substructures

The RPS fractions ($F_{\rm RPS}$) were determined in the same fashion as in Chapter 4, dividing the number of blue late-type RPS member candidates by the number of blue late-type members. We computed $F_{\rm RPS}$ for cluster members inside and outside substructures, and excluded the lowest-confidence RPS candidates ($J_{\rm Class} = 1$). In Fig. 5.3, we show these two fractions with their respective 1σ binomial confidence intervals computed

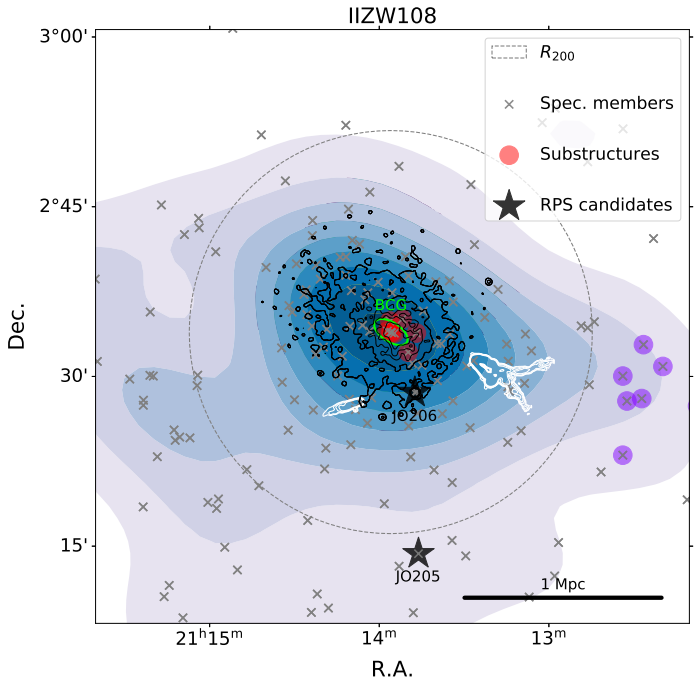

Figure 5.2: Location of the Head-Tail galaxies with respect to the cluster members (grey Xs) and optical substructure (coloured dots). The BCG is represented by a green ellipse (with ellipticity and position angle taken from HyperLEDA), and the density of members is shown as blue contour levels. We show the contours of the radio emission of the head-tail galaxies (white) and of the X-ray emission (black). The jellyfish galaxies are indicated by a black star symbol. Figure from Müller et al. (2021).

following Cameron (2011). The substructure environment hosts a lower fraction of RPS candidates by a factor of ~ 1.5 and with $> 1\sigma$ significance. Of all the RPS candidates with confirmed memberships, $\sim$70% are outside substructures.

This is an important result for understanding the physical processes involved in pre-processing galaxies in substructures before entering the cluster. Analyses regarding the impact of the clustercentric distance, substructure richness, and galaxy stellar masses are essential to further investigate the origin of the RPS fraction suppression in substructures.

5.3 Impact of substructure richness

It is known that more massive halos have larger fractions of quenched galaxies and are gas-poor (e.g. Boselli et al., 2016b; Jaffé et al., 2016; Park et al., 2023). Group rich-

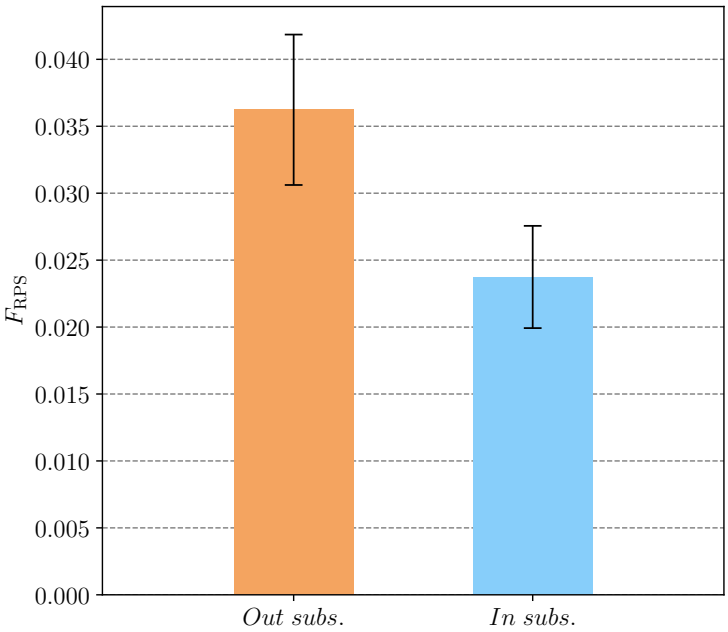

Figure 5.3: Fraction of blue spiral RPS candidates with $J_{\rm Class>1}$ outside (orange bar) and inside (blue bar) substructures. The 1σ binomial confidence intervals computed following Cameron (2011) are shown in black.

ness is related to the halo mass and can significantly affect $F_{\rm RPS}$, as a more massive substructure halo would result in stronger RPS.

The distribution of galaxy richness in the substructures found is shown in the histogram of Figure 5.4. Twenty-five per cent of our substructure sample has more than 12 galaxies. The most massive substructures have 27 galaxies and are located in Abell 3667 and Abell 3716, as seen in appendix B. In Abell 2399, a substructure with a similar number of members had an X-ray counterpart identified in Lourenço et al. (2020).

To search for differences in the RPS fractions with group richness, we divide the sample into two richness bins split by the mean value (= 10 galaxies, indicated by the dashed black line). In fig. 5.4, the poorer bin has 535 blue late-type members and 12 RPS candidates, and the richer bin has 518 and 13, so the F_{RPS} are very similar, as shown in the upper panel. In other words, there is no clear enhancement or suppression of RPS in richer substructures.

Although richer substructures are easier to detect, they also have more contamination by interlopers. We did not consider this caveat in our analysis and will discuss the possible implications later. Moreover, it is important to highlight that while our sample is the largest known sample of RPS candidates when we split into cluster or

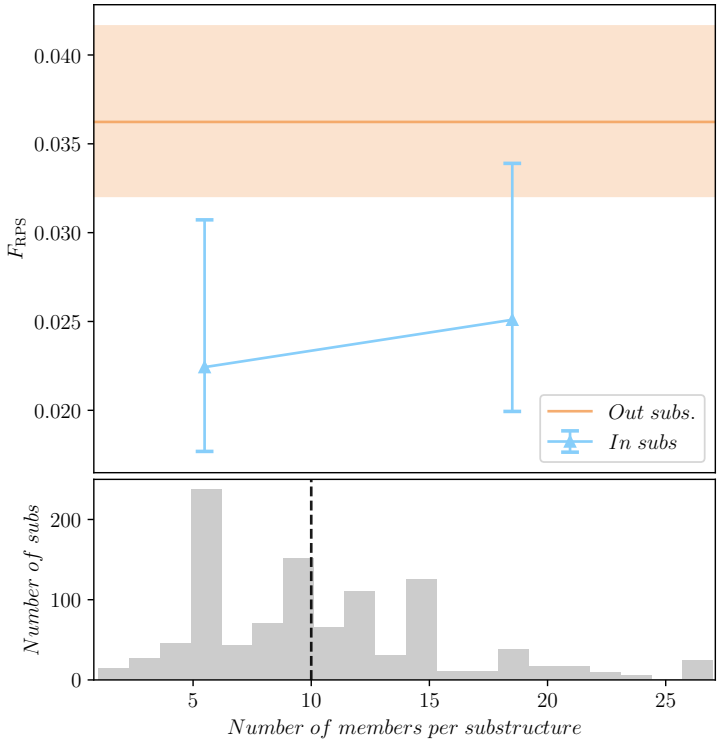

Figure 5.4: Upper panel: Fraction of blue spiral RPS candidates in substructures with less than 10 and more than 10 members. The orange line shows the reference RPS candidate fraction for galaxies outside the substructure. The orange shade represents the binomial confidence interval. Lower panel: Distribution of the number of members in each substructure. The dashed black line shows the mean.

galaxy properties, the statistical uncertainties grow, and it is hard to see any possible signal.

5.4 Dependence on clustercentric distance

Ram pressure stripping increases as a galaxy approaches the cluster centre. Therefore, it is important to analyse how RPS fractions change in different clustercentric distances. In Fig. 5.5, we split our sample into two radial bins according to the mean radius, 0.66 R_{200}, of the galaxies in our sample to compare the impact of the cluster with the impact of the substructure in different radii.

Tab. 5.1 summarises the number counts of RPS candidates and blue late-type galaxies in each radial bin. In both bins, the RPS fraction is smaller inside substructures.

However, in the outer bin, even if there are fewer counts than in the inner bin, the confidence interval bars are smaller than in the inner bin. This can be due to the increase in the purity and completeness of substructure members in the more external clustercentric distance, as discussed in B23.

		$\leq 0.66\,R_{200}$	$> 0.66\,R_{200}$
Inside subs	RPS counts	16	9
	BS counts	398	655
	$F_{\rm RPS}$	$0.04^{+0.012}_{-0.007}$	$0.01^{+0.006}_{-0.003}$
Outside subs	RPS counts	35	20
	BS counts	686	832
	$F_{\rm RPS}$	$0.05^{+0.009}_{-0.007}$	$0.02^{+0.006}_{-0.004}$

Table 5.1: Galaxy counts and RPS candidate fractions in different radial bins inside and outside substructures.

5.5 Dependence on galaxy mass

If RPS is stronger than the anchor force of a galaxy, its Interstellar medium (ISM) is stripped. The anchor force, in turn, depends on the surface density of the ISM and the galaxy's mass. Less massive galaxies should exhibit more RPS features.

In Fig. 5.6, we use the distribution of the RPS candidates shown in the lower panel to split our sample into three mass bins. Tab. 5.2 summarises the number counts of RPS candidates and blue late-type galaxies in each mass bin. There is no significant difference between the fractions inside and outside substructures in the less massive ($logM_* < 9.6$) and more massive ($logM_* \geq 10.2$) bins. Galaxies within the intermediate mass bin ($9.6 \leq logM_* < 10.2$) seem to drive the suppression of RPS fractions inside substructures.

In the lower panel of Fig. 5.6, we can notice that the blue spiral distribution (dashed line) is shifted towards the less massive bin, while the RPS candidates are more centrally peaked in the intermediate mass bin.

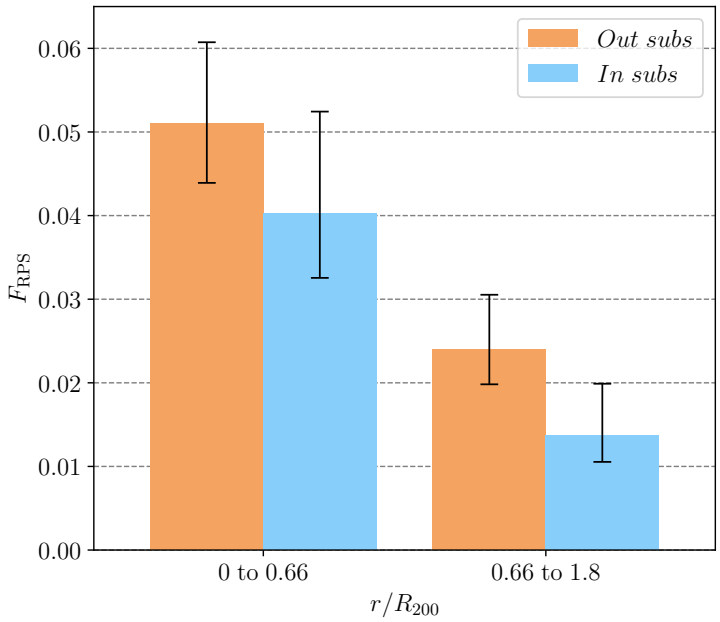

Figure 5.5: Fraction of blue spiral RPS candidates outside and inside substructures in two radial bins $r < 0.66$ and $> 1.2\,R_{200}$).

		$logM_* < 9.6M_\odot$	$9.6 \leq logM_* < 10.2$	$logM_* \geq 10.2$
Inside subs	RPS counts	7	7	11
	BS counts	532	281	240
	$F_{\rm RPS}$	$0.01^{+0.006}_{-0.003}$	$0.02^{+0.013}_{-0.006}$	$0.05^{+0.017}_{-0.01}$
Outside subs	RPS counts	8	32	15
	BS counts	728	485	305
	$F_{\rm RPS}$	$0.01^{+0.005}_{-0.002}$	$0.07^{+0.01}_{-0.009}$	$0.05^{+0.015}_{-0.009}$

Table 5.2: Galaxy counts and RPS candidate fractions in two different galaxy stellar mass bins.

5.6 Galaxy properties

In Fig. 5.7, we investigate whether RPS candidates inside and outside substructures differ. We compare stellar masses, colours, Jclass, and the directions of the stripped

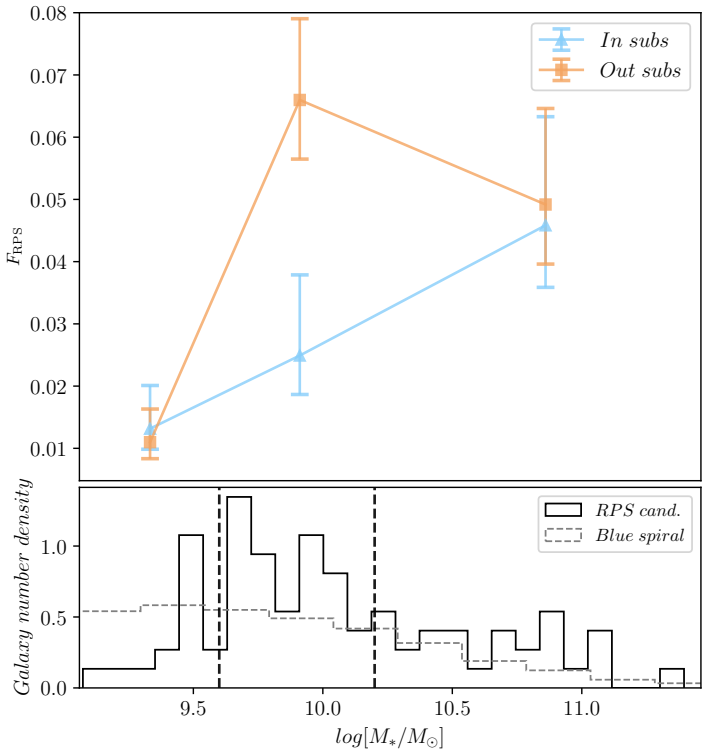

Figure 5.6: Upper panel: Fraction of blue spiral RPS candidates in a massive ($logM_* > 10.13$) and low-mass ($logM_* < 10.13$) galaxy stellar mass bin. As in previous figures, orange shows the fractions of candidates outside substructures and blue inside substructures. Lower panel: Galaxy stellar mass distribution. The dashed black line shows blue spiral galaxies and the solid line shows RPS candidates.

tails.

The first and second panels show that the stellar masses and colours of the RPS candidates inside and outside substructures have no significant difference according to the KS statistics. In the third panel, we analysed the Jclass, which measures how confident the classifier was that the galaxy was undergoing RPS. There is no clear trend between substructures and Jclass.

Finally, we compared tail directions obtained by Salinas et al. (2024). Most RPS candidates have their tails pointing away from the BCG (angles closer to 180°), especially for the candidates out of substructures (orange histogram). This is indicative that the galaxies radially infalling to the cluster are in the first pre-pericentric passage (Smith et al., 2022; Salinas et al., 2024). To further investigate the orbital parameters of the RPS candidates, we split them into several bins of tail angles. Dividing the sample

into four bins allows us to identify galaxies travelling towards or away from the BCG or going in perpendicular directions. The relative difference between the first and the last bins is less pronounced in substructures (blue histogram) than in the outside substructures' histogram. However, if we work with the hypothesis that substructures shield their members, the enhancement in the fourth tail angle bin inside substructures is not expected. We further analysed the fourth bin; six out of nine galaxies are located in substructures with less than ten members. It is important to investigate the impact of substructure masses in this bin. Unfortunately, our sample size does not allow us to restrict the analysis to only large substructures without harming the statistics.

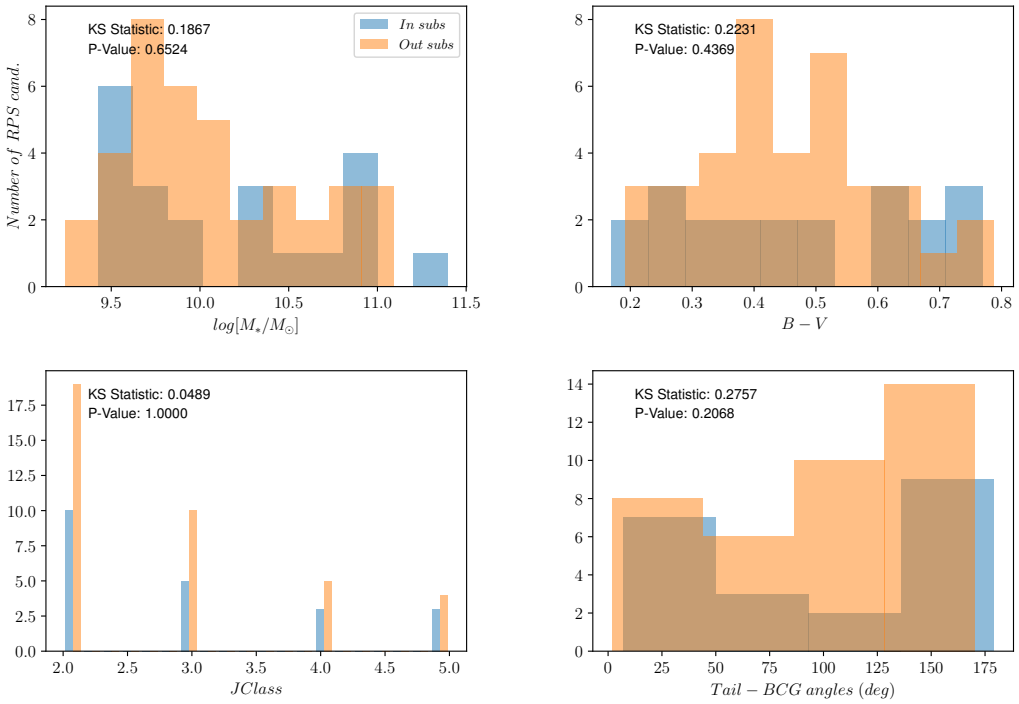

Figure 5.7: Properties of RPS candidates inside and outside substructures. Panels shown from left to right show the distributions of the logarithm of galaxy stellar mass, galaxy colours, Jclasses, and tail angles, respectively. Colour codes are the same as in previous figures.

5.7 Discussion

Our main result shows that RPS candidate fractions are suppressed in substructures. This result is possibly influenced by two distinct effects. One is the effectiveness of RPS inside groups (=substructures). This is reduced with respect to the cluster because of the less dense ICM and lower galaxy velocities in groups. However, the other is the shielding of the galaxies inside groups by the intra-group medium, as these groups infall into clusters. Indeed, Fujita & Goto (2004) show that RPS cannot be fully ignored in simulated subclusters at $z \sim 0.5$, but the overall RPS fractions are lower in subclusters. They offer a different scenario where the tidal force from the main cluster may have galaxies elude the central region of the subcluster where ram pressure stripping is effective.

There is also the simpler hypothesis that, in substructures, the galaxies strip each other gas by tidal stripping. So, the majority of the gas is in the intragroup potential. A future step for this work is to consider the ram pressure stripping from the cluster to the group, considering the gas loss from the substructure and not from the member galaxies. Even before the RPS exert its effects, there will be the tidal force from the cluster potential on the infalling group, further diminishing the gas amount, which can be stripped once the RPS effect starts.

Hess et al. (2022) identified galaxies undergoing RPS that are also part of a substructure that has already passed its pericenter. They conclude that the substructure environment could protect its members' HI content. This substructure shielding effect could be related to the suppression in the RPS fractions we found for our statistical sample. Most substructures identified by DS+ (75%) have less than 12 galaxies. If substructures shield their members from RPS with their IGM, this would be possible only when the substructure is rich enough to retain their cold gas. However, if a substructure is too rich, the intragroup medium (IGM) would heat and mix more easily with the ICM, reducing the shielding efficiency. Also, galaxies in richer substructures have higher velocities, and the IGM medium is denser than in poor substructures. In Fig. 5.4, there is a possible enhancement in the RPS fractions of the richer substructures that could be explained by the IGM properties of rich groups and the group member velocities. Ideally, an analysis in more than two richness bins should be performed. However, our sample size does not allow us to do so.

The clustercentric radius is an important variable to segregate the effects of the cluster and the substructures in the RPS fractions. Boselli et al. (2021), using semi-

analytic models, show that ∼1% of massive infalling galaxies are expected to undergo RPS upon crossing R_{200} of clusters more massive than $M_{Cluster} > 10^{14}\,M_{\odot}$. At a distance of $0.5\,R_{200}$, half of the massive galaxies are currently experiencing RPS. In contrast, low-mass infalling galaxies should initiate their stripping much earlier, with 90% undergoing RPS within. We investigated the impact of clustercentric radius and galaxy mass and attempted to isolate the effect of substructure accretion on RPS. In Fig. 5.5, we show the RPS fraction inside and outside substructures in two radial bins. Unfortunately, the size and extension of our data do not allow us to split the sample further. Even when splitting our sample by radius, we notice that RPS fractions outside substructures are always higher than inside substructures, but not significantly. The closer a substructure is to the cluster centre, the more contamination is expected in its members, as shown in Benavides et al. (2023). This could explain the larger confidence intervals in the internal radial bin ($\leq 0.66\,R_{200}$).

RPS is particularly relevant in galaxy groups for dwarf galaxies (McConnachie et al., 2007). Unfortunately, our sample does not have RPS candidates with $logM_{*} < 9\,M_{\odot}$ to compare RPS fractions in the dwarf galaxy regime. The lower mass bin presents no difference between RPS fractions inside and outside substructures. This may result from the challenges associated with detecting RPS faint features in low-mass galaxies, which can be attributed to their low surface brightness (Steyrleithner et al., 2020). The higher mass bin also shows no significant difference between the RPS fractions inside and outside substructures. The large confidence interval bars do not allow us to conclude about this bin. The intermediate stellar mass bin is the only one driving the observed RPS fraction suppression inside substructures. This suggests that we are unable to see the faint optical RPS signatures in low-mass galaxies. However, we know that low-mass galaxies are more affected by RPS than high-mass galaxies, implying that a) they are also more effectively shielded or b) their HI gas is being stripped, but no star formation is occurring, so we cannot see any optical RPS signatures [2]. Larger galaxy samples and deep radio observations are necessary to understand the significance of this result.

RPS candidate properties could also be different inside and outside substructures. We investigate galaxy stellar mass, colours, Jclasses, and tail angle distributions. The `KS` test showed no difference between the distributions (P-values are all above 0.05). However, the tail angles show an interesting trend. Outside substructures, the tail

[2]We caution that we are talking about optical RPS features which are linked to in situ star formation (Gullieuszik et al., 2020, 2023).

angles are mostly > 90 deg. Very likely, most of the RPS candidates outside substructures are travelling to the cluster centre. This agrees with the finding that most RPS candidates are first in-fallers (Jaffé et al., 2018; Biviano et al., 2024). Oddly, inside substructures, we still find a peak in the RPS counts > 135 deg. We further investigated this bin and found six out of nine galaxies are located in substructures with less than ten members. This could indicate that substructures with few members are inefficient at shielding their members against the ICM. Unfortunately, our counts are too low to analyse this sub-sample further. The effects of rich substructures in the tail angles should be considered when using them to study galaxy orbits. However, we recall that $\sim$40% of the substructure members are spurious according to the simulations, so this likely impacts this result.

CHAPTER 6

Conclusions and future perspectives

This chapter will conclude this thesis by summarising our main findings concerning our research aim of understanding how cluster growth impacts the pre and post-processing of their member galaxies. It will also discuss the value and limitations of our findings and propose ways of improving the results in the future.

6.1 Post-processing due to cluster mergers

Chapter 4 (Paper I) studies the incidence of RPS candidates relative to the infalling population of galaxies in clusters of different dynamical states using the largest and most homogeneous sample of RPS candidates at low redshift from P16 and a variety of cluster dynamical state proxies.

In summary, the main results are:

- We computed the photometric and spectroscopic fractions of RPS candidates relative to the infalling population of blue spiral galaxies in each cluster. The former was carefully corrected by the expected field contamination, while the latter used confirmed cluster members. They both considered the same circular area within the clusters (with a radius of $0.7\,R_{200}$) for homogeneity. Both fractions are in general agreement with some scatter. The mean RPS candidate fraction of both samples is around $11-12$ per cent.

- We found no correlation between RPS candidate fractions and a variety of automatic cluster dynamical state indicators. In particular, we examined eight optical and X-ray indicators, including X-ray concentration and the magnitude gap between the two brightest galaxies.

- We further constructed a "cluster merger sequence" by splitting the sample into five different dynamical state classes (pre-merger, relaxed, interacting, interacting and post-merger) following a visual dynamical state classification flowchart based on optical, X-ray, and radio data. When doing this, we found hints of an RPS candidate fraction enhancement in the interacting class, followed by a decay in the post-merger bin. The results, however, are driven by a limited number of interacting and post-merger clusters (five and five) and are not statistically significant.

- We found no apparent correlation between RPS candidate fractions and cluster mass or X-ray luminosity, even when excluding the disturbed clusters from our sample. This could be associated with the small radius coverage of our analysis or the complexity of the RPS process.

A few studies of individual interacting clusters found elevated numbers of galaxies' RPS features. These studies, together with theoretical predictions, built a common understanding that collisions between clusters would increase the fractions of galaxies undergoing RPS. This work is the first attempt to quantify the effect of the cluster dynamical stage in RPS in a homogeneous way using a large cluster sample. Overall, we find hints of a possible RPS enhancement in interacting clusters. The low confidence in our results is due to the inevitably low-number statistics (despite using the largest homogeneous sample available) and the complexity of cluster growth. In particular, the limited coverage of cluster observations and the nature of the optical selection of RPS galaxies, which requires star formation in the striped tails.

Our study, with its methods and special considerations, can serve as a guide for future studies using even larger samples of RPS candidates currently being assembled (see e.g. the citizen science project "Fishing for jellyfish galaxies"[1]), and also wider multi-wavelength cluster coverage, such as the upcoming WEAVE (Jin et al., 2023) and CHANCES (Haines et al., 2023) wide-field cluster spectroscopic surveys and the eROSITA X-ray mission (Merloni et al., 2012).

[1] https://www.zooniverse.org/projects/cbellhouse/fishing-for-jellyfish-galaxies

6.2 Pre-processing in infalling groups

In Chapter 5 (Paper II), we investigated the relationship between RPS and pre-processing in groups. We used the largest optical sample of RPS candidates in the local Universe by merging the catalogues from P16 and V22, and a catalogue of identified galaxy substructures in the WINGS clusters.

We summarise and detail our main findings as follows:

- We found that RPS candidate fractions to the infalling population are suppressed inside recently in-fallen groups.
- RPS fractions are suppressed in the substructure environment by 1.8-σ, irrespective of clustercentric distance.
- The RPS fraction for galaxies inside substructures does not correlate with the richness (number of members) of the substructures.
- Substructures in the inner clustercentric distances have higher RPS candidate fractions than the ones in the outer radii. The same happens with candidates outside substructures. Therefore, even if substructures shield galaxies from being ram pressure stripped, the intracluster medium takes over at small clustercentric distances because of the higher gas density.
- When splitting the sample into three galaxy stellar mass bins, we found the RPS candidate fraction suppression to be driven by the intermediate mass bin ($9.6 \leq logM_* < 10.2$).
- We found no differences in colour, stellar masses, and Jclasses of RPS candidate's inside and outside substructures. However, the stripped debris tails tend to have relative tail angles to the BCG > 90 degrees in the sample of candidates outside substructures. This indicates that most of these galaxies are entering the cluster for the first time. In substructures, the tail direction may be influenced by interactions within the substructure environment.

In summary, our analysis shows that subgroups that recently entered galaxy clusters prevent blue spirals from showing ram pressure stripping optical features. This shielding effect predicted by some theoretical studies (Roediger et al., 2015a,b) and hinted by observations of single clusters (Hess et al., 2022) was observed for the first time in a statistical sample in this thesis. However, despite having the largest sample

of RPS candidates available from the literature, the statistical uncertainties and limitations of the dataset did not allow us to robustly explore possible correlations with galaxy and group properties. Future surveys covering wider areas would improve our results and possibly clarify which physical mechanisms are involved in this shielding effect.

6.3 Future perspectives

The WINGS and OmegaWINGS surveys filled a significant information gap in our understanding of the properties and evolution of galaxies within local clusters. WINGS provides wide-field photometric and spectroscopic data, ensuring morphological classifications and measurements of stellar population ages, metallicities, and star formation histories. It also facilitates comparisons with distant clusters and addresses the lack of detailed data on nearby clusters.

P16 and V22 are the first homogeneous statistical samples of optical RPS candidate galaxies in the local Universe. Thanks to these systematic searches, we know that the jellyfish galaxies with the longest gas tails reside very near the cluster cores, are moving at very high speeds, and are in the first infall into the cluster in highly radial orbits (Jaffé et al., 2018). Also, from these studies, we know that stripping galaxies have enhanced star formation rates at any given mass (Vulcani et al., 2018). Paper I and Paper II are pilot studies for future avenues in the era of large surveys and datasets coming ahead.

6.3.1 Towards constructing larger samples

Larger samples of galaxies undergoing environmental transformations, such as RPS, are needed. The complex morphologies of ram pressure stripping candidates make them difficult to detect with automatic analysis. The human eye is still the best tool for identifying signs of disturbances and trailing material. With citizen science projects, we extend the catalogues of these galaxies to aid in understanding the complex interactions which produce the RPS features (Walmsley et al., 2022, 2023, Bellhouse et al. in prep). Future wide-field imaging surveys, such as the LSST (Ivezić et al., 2019), might utilise citizen science to study RPS phenomena out to the cluster outskirts. This approach would significantly increase the number of galaxies observed to be undergoing visible RPS. These bigger samples combined with the environment characteri-

sation provided by wider cluster multi-object spectroscopic surveys such as 4MOST (de Jong et al., 2019) and one of its extragalactic community surveys, CHANCES, will allow this study to be reproduced considering the regions where RPS is more likely to be influenced by cluster mergers, the infall region.

The eROSITA X-ray telescope, with its large 1-degree FOV, has conducted the most extensive survey of galaxy clusters to date and will provide a catalogue of over 60,000 galaxy clusters and groups from its first two years of the all-sky survey. This survey will not only increase our cluster and group samples but also aid in the understanding of the large-scale structure, such as X-ray filaments interconnecting clusters. Another X-ray mission scheduled for 2034, Athena, with its unprecedented spectral resolution[2], will allow us to characterise the velocity of the X-ray-emitting gas in substructures while moving through the ICM (Ettori et al., 2013). We will be able to tell with high precision if the galaxies and gas in substructures are moving at the same velocities, imposing important physical constraints on the ram pressure affecting infalling groups.

Currently, advances in the studies of cold gas in satellite galaxies are mostly made in the nearby universe. H I deep imaging surveys with wide-field cameras are ideal for identifying galaxies undergoing an RPS event. However, H I and H_2 studies are just beginning to obtain and analyse statistical samples, and significant contributions from future large-area surveys such as ASKAP, MeerKAT, and WALLABY are expected. Especially SKA, which will provide radio continuum and line observations at unprecedented sensitivity and angular resolutions for hundreds of thousands of galaxies in nearby and high redshift clusters. These developments will provide massive data sets for a better understanding of gas dynamics and galaxy evolution through comprehensive statistical analyses.

6.3.2 Understanding the role of filaments in the pre-processing of galaxies

As already explained in Sec. 1.3.4, filaments of galaxies, which account for half the cosmic web's mass (Cautun et al., 2014), significantly influence galaxy pre-processing,

[2]The high statistical precision of the redshift measurements with Athena will enable mapping of the radial components of the bulk motions due to recent mergers in nearby (z∼0.1) clusters of galaxies for the first time. At a spatial resolution of 0.1 R_{500}, velocities of 10 km/s can be detected at the cluster centre, and 50 km/s at 0.25 R_{500} at 3-σ (Ettori et al., 2013).

making galaxies redder (Chen et al., 2017; Luber et al., 2019), more quiescent (Martínez et al., 2016; Kuutma et al., 2017), and more massive than field galaxies (Alpaslan et al., 2016; Chen et al., 2017). Identifying these filaments in surveys is challenging due to biases and observational errors. However, studies show that galaxies align along the major axis of the BCG, indicating that clusters and their BCGs grow aligned with cosmic filaments. This alignment also affects quenching patterns, with higher quenching fractions along the BCG's major axis (Martín-Navarro et al., 2021; Ando et al., 2023; Karp et al., 2023; Stott, 2022). The quenching is possibly linked to the shape of the intracluster medium, with galaxies along the major axis experiencing more RPS. These findings are supported by observational and simulation data across different redshifts.

Within the dataset explored in this thesis (Sec. 2), we found cases such as IIZW108 (mildly interacting) and A3880 (relaxed), shown in Sec. 5.1, where RPS is intensified in the direction of the BCG major axis. To verify if this effect appears in a statistical sample, we stack all the relaxed and mildly interacting clusters of Paper I to measure fractions of RPS candidates according to the BCG major axis. Relaxed clusters are more suited to this purpose since they are less affected by miscentring. In the left panel of Fig. 6.1, we show the stacked clusters aligned according to their BCG major axis and the distribution of blue late-type galaxies and RPS candidates. We only show spectroscopically confirmed blue late-type members in relaxed and mildly interacting clusters. In the right panel, we observe a possible enhancement of RPS candidate fractions in the minor axis direction. However, a larger sample is necessary to confirm this result.

An analysis performed on the same dataset by Vicente Salinas in private communication shows that the directions of the stripped tails do not show any preferential direction with respect to the BCG major axis. The disadvantage of using the BCG major axis as a proxy to the main filaments is that the number of connecting inter-cluster filaments is higher than two (around six in Kotecha et al. (2022)). Also, filaments very often have complex shapes. These two factors could be responsible for blurring out the signal of RPS candidate fractions in the direction of the BCG minor axis. Using filament finders such as `DISPERSE` out to a large clustercentric distance would possibly improve this result.

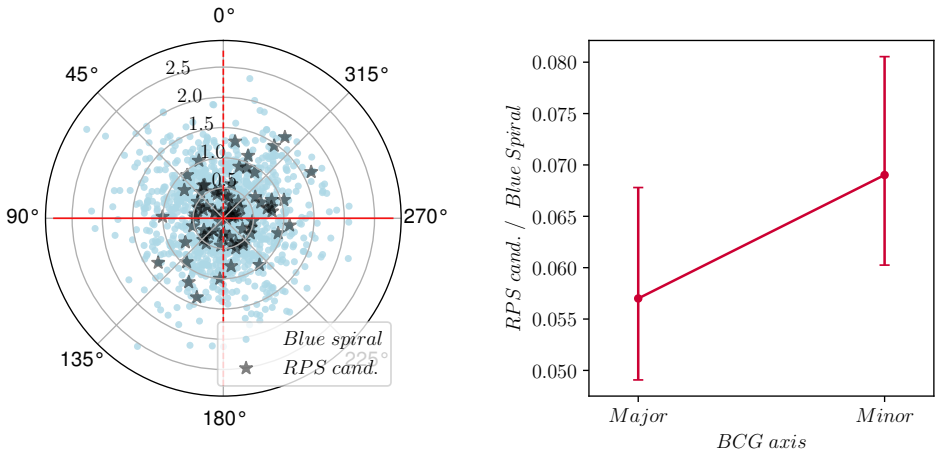

Figure 6.1: RPS anisotropy. The left panel shows the stacked cluster sample aligned to the BCG major axis. Blue spiral members are shown as light blue circles, and RPS candidates are shown as black stars. The dashed red line shows the BCG major axis position, and the solid red line shows the minor axis position. The right panel shows the fractions of RPS candidates among the blue spiral members.

6.3.3 Continuous environmental tracers

When studying RPS in satellite galaxies, the environment is usually described by distinguishing between galaxy groups and clusters, which underestimates the continuous nature of cosmic environments. Traditional binary classifications do not consider that environmental factors like halo mass, local density, and proximity to cosmic filaments vary continuously. This calls for physically motivated descriptors that convey the inherent intricacy of these environments. In preliminary work, we investigate the effects of continuous tracers on different populations of galaxies.

An interesting result shown in Fig. 6.2 is that spiral galaxies tend to be displaced to regions of higher local density in disturbed clusters compared to a control sample of relaxed clusters. The comparison used only member galaxies within $0.7\,R_{200}$. Spirals are less bound to the clusters than ellipticals and hence could be more affected in a cluster-cluster interaction. The displacement of the late-type population would also apply to jellyfish since they are a sub-population of spirals. This could explain why some focused studies claimed to have found an enhanced number of RPS candidates in the central parts of merging clusters. This analysis should be reproduced with the different dynamical state classifications presented in Sec. 3. Also, expanding the analysed radius and increasing the sample could significantly enhance the differences we

found.

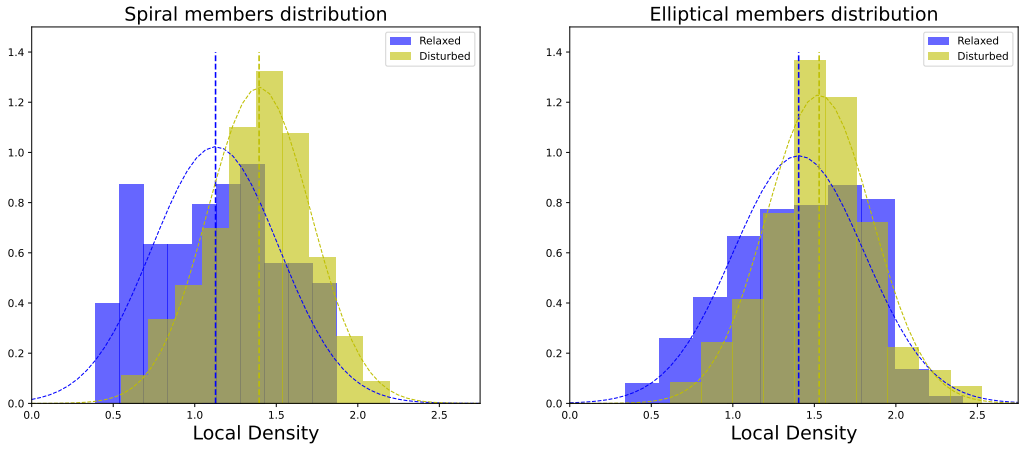

Figure 6.2: Stacking of the spiral members of disturbed and relaxed clusters from our sample flowchart class 2 and 5, respectively. The distribution of the spirals in disturbed clusters is skewed towards the high-density regions.

6.3.4 Discovery of large intra-cluster stripped debris

In the second semester of 2022, we obtained deep DECam data (Prop. ID: 2022B-791264) for a cluster from my PhD sample and serendipitously discovered an unprecedentedly wide blue structure at a projected distance of 293 kpc from the cluster centre. This structure, composed of several collimated blue stripes, suggests intense ram-pressure stripping of multiple galaxies simultaneously. The blue stripes have several associated UV-emitting knots, indicating ongoing star formation and making it essential to confirm their nature and origin. One year later, we followed up on this object with IMACS at the Magellan telescope (prop. ID: CN2023B-61) to investigate the nature and origin of the blue stripes.

In the near future, we will analyse the IMACS long-slit data and confirm if the entire length of the blue stripes and all the associated star-forming knots are at the same redshift as the galaxy cluster and possibly in the same redshift of a substructure identified by DS+ to confirm if such a wide feature is a consequence of a strong ram-pressure stripping event that possibly happened in several galaxies at a similar time. Also, we will investigate if the source of ionization is star formation through the widely used Baldwin, Phillips & Terlevich (BPT, Baldwin et al., 1981) diagram.

Extended ionized gas (EIG) regions have already been found in some nearby clus-

ters at $z < 0.02$ (e.g. Gavazzi et al., 2001; Kenney & Koopmann, 1999; Yagi et al., 2007; Sun et al., 2007) and in more distant clusters at $z \sim 0.4$ (e.g. Yagi et al., 2015). The most similar case to the blue stripes in the literature is an EIG region reported in A1367. This feature showing large Hα trails and orphan clouds was studied by Yagi et al. (2017), who linked it to a blue high-velocity infalling group. So far, none of the reported EIGs has such a collimated and wide morphology as the blue stripes observed in the optical in A133.

If the blue stripes are gravitationally bound, they might be the ancestors of the population of cluster dwarf galaxies. If not, they will scatter their stars over the ICM, increasing the intracluster light (ICL) in the cluster centre. The magnificent optical trails observed in the blue stripes suggest that significant ICM enrichment might result from the ram-pressure stripping of infalling groups. The formation of the ICL is not fully understood, and the rare (short-lived) EIG could shed some light on the ICL build-up enigma. Two jellyfish-like galaxies with associated blue optical trails of stripped debris are observed in the NW part of the cluster (Fig. 6.3), travelling in the same direction as the blue stripes themselves, highlighting that the core of this fairly relaxed cluster is undergoing a great deal of transformation.

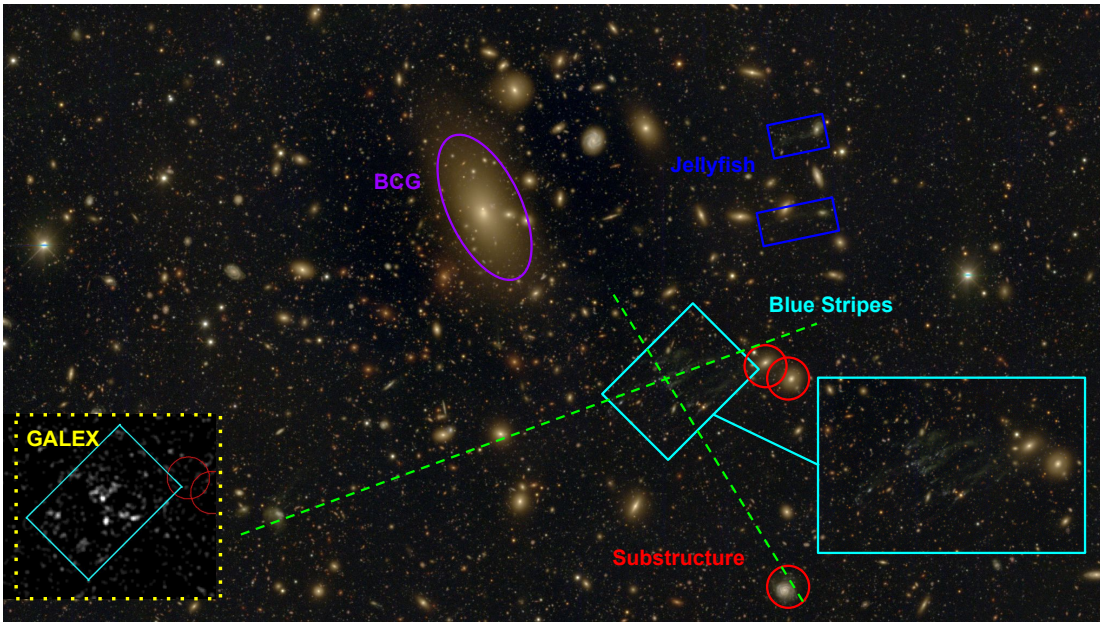

Figure 6.3: Proprietary DECam data 3-colour optical image. The blue stripes are visible inside the cyan rectangle in the composite image, along with a near-ultraviolet image from GALEX and a zoomed-in cutout of the coloured image. Red open circles show the substructure identified by the modified DS test. Two jellyfish galaxies travelling in the same direction of the blue stripes, at a projected distance of 326 kpc, are inside the dark blue rectangles. These strong ram-pressure stripped cases highlight that this cluster core is undergoing a great deal of galaxy transformation. The green traced lines show where we will place the gratings.

Appendix A

Centres for computing fractions and visual dynamical state sequence (flowchart).

In this appendix, we explore the challenges and methodologies for determining the centres of merging galaxy clusters. We detail cases of complex galaxy clusters, highlighting how midpoints between brightest and central galaxies and X-ray emission peaks are consistently used to define the cluster centres with a visual dynamical state sequence flowchart.

A.1 BCGs and centers

Merging clusters often have several X-ray surface brightness peaks, each possibly associated with a local BCG. Their gas morphology can be highly irregular, and their surface brightness is often low in the X-ray, causing the centre determination to be very challenging. In major mergers, the BCG can be significantly displaced from the X-ray peak.

Also, the determination of BCGs is not always so evident. In most cases, we used Fasano et al. (2010)'s BCG, which was located near the X-ray centre. The clusters where

Fasano et al. (2010) and this work disagree about the BCGs are only five: Abell 3560, Abell 3158, Abell 1736, Abell 1631a, and Zwicky 8852. After inspecting the images, we found that for A1631a and A3158, the BCG indicated by Fasano et al. (2010) was not located in the centre of the X-ray emission, whereas the one identified in this work was. The BCGs this work identified in A3560, A3158, A1736, and Z8852 are in the list of cD galaxies, Tab.2, of Fasano et al. (2010). Their coordinates are listed in Tab. A.1. In these cases, we adopted this work's BCG as the centre to be consistent with the flowchart in Fig. 3.3. The BCG identified by Fasano et al. (2010) and this work for RX1022 is the same (WINGSJ005822.88+265152.6), although it is not the bright galaxy associated with the main X-ray concentration (WINGSJ102209.99+383123.8). We used the latter bright galaxy as a centre to be consistent with our flowchart. A similar case happened in two other clusters. In A2415, we had to replace the BCG (WINGSJ220526.12-054431.1) with the galaxy WINGSJ220538.62-053532.0 located at the centre of the X-ray emission. The other case, A2399, is a very complex merging system identified as a bullet-like cluster by Lourenço et al. (2020). This work identified more than one central bright galaxy associated with the X-ray emission. We opted to use the galaxy WINGSJ215729.43-074744.1 as the centre.

Below, we list and describe the most challenging clusters for centre determination.

Abell 168: This post-merger system has a very irregular and faint X-ray emission. Previous works identified cold fronts (Hallman & Markevitch, 2004) and radio relics (Dwarakanath et al., 2018). The radio relics in this cluster are very asymmetrical. After careful inspection of the X-ray and optical images, we chose as the centre the midpoint between the BCG WINGS J011457.58+002551.1, which is associated with the X-ray peak, and the seventh brightest member galaxy (WINGSJ011515.77+001248.6), which seems to be the brightest galaxy associated with the southern X-ray clump centre.

Abell 3376: This system is one of the most extreme cases of post-merger in our sample. It has two megaparsec-sized arc-shaped radio relics (Bagchi et al., 2006), and its X-ray emission is very asymmetric (Akamatsu et al., 2012; Urdampilleta et al., 2018). Simulations (Machado & Lima Neto, 2013) and observations (Durret et al., 2013; Monteiro-Oliveira et al., 2017b) suggest that this system results from the collision between two clusters with a mass ratio 3–6:1. We used the midpoint between the BCG (WINGSJ060041.09-400240.4) and the bright galaxy (WINGSJ060217.27-395634.2) as the system centre.

Abell 754: Displaying X-ray shocks and radio relics (Macario et al., 2011), cold fronts (Ghizzardi et al., 2010), and a halo (Kass & Wasserman, 1995; Bacchi et al., 2003),

this system is yet another case of a post-merger in the plane of the sky. The distribution of galaxies is quite complex (Fabricant et al., 1986; Zabludoff & Zaritsky, 1995). The two main concentrations of galaxies correspond to the two components of diffuse radio emission (Bacchi et al., 2003; Inoue et al., 2016). To compute the centre, we used the midpoint between WINGSJ090832.39-093747.3 and WINGSJ090919.21-094158.9 bright elliptical galaxies.

Abell 3667: Abell 3667 is a bright X-ray source (5.1×10^{44}erg s^{-1}; Ebeling et al., 1996), and evidence of merger activity has been observed with various X-ray instruments, e.g., *ROSAT* (Knopp et al., 1996), *Chandra* (Vikhlinin et al., 2001; Mazzotta et al., 2002), *XMM*-Newton (Briel et al., 2004), Suzaku (Nakazawa et al., 2009), and also in other wavelengths, e.g., radio (Rottgering et al., 1997). The central cluster hosts an X-ray mushroom-shaped feature, probably resulting from the disrupted cool core of a subcluster that passed its centre 1 Gyr ago (Sarazin et al., 2016; Roettiger et al., 1999). Abell 3667 is also one of our sample's most complex interacting systems. It has optical substructures, a cold front, and interesting diffuse radio features such as double relics and an unpolarised bridge associated with a merging event (Rottgering et al., 1997). We used as its centre the computed midpoint between the BCG (WINGSJ201227.32-564936.3) and the galaxy WINGSJ201050.55-564024.5.

Abell 3528: This double system (Raychaudhury et al., 1991) is composed of a northern and southern cluster, A3528-N and A3528-S, respectively, each of them with well-centred BCGs separated by 13.3 arcmin ($\sim 0.45R_{200}$) in projection and a slight velocity difference (~ 357 km/s). Both components are cool core and relaxed (Andrade-Santos et al., 2017; Lopes et al., 2018; Laganá et al., 2019). Optical (Bardelli et al., 2001; Baldi et al., 2001) and radio observations (Reid et al., 1998; Venturi et al., 2001) indicate this is a pre-merger system close to virial equilibrium in the central regions of its components. We used the midpoint of the northern (WINGSJ125422.23-290046.8) and southern (WINGSJ125441.01-291339.5) X-ray concentrations BCGs as the system centre.

Abell 3716: Analysing X-ray data from *Chandra*, *XMM*-Newton, and *ROSAT* (Andrade-Santos et al., 2015) concluded that A3716 is a double cluster separated in projection by 400 kpc. This system shows bi-modality in spatial distribution and position-velocity diagram (Lopes et al., 2018). Bilton et al. (2019) surmised that the cluster pair is in an early stage of merger by studying its kinematics, which corroborates with a dynamical analysis performed by Andrade-Santos et al. (2015) that shows that this system is probably gravitationally bound and will undergo core passage in

500 ± 200 Myr. We calculate the system's centre as the midpoint between the BCG of the northern X-ray concentration (WINGSJ205156.94-523746.8) and the southern X-ray concentration (WINGSJ205209.55-524745.4).

Abell 3530 and Abell 3532: This cluster pair is part of the Shapley supercluster and is separated by 22.8 arcmin ($0.95R_{200}$). The BCG of A3530 is the galaxy WINGSJ125535.99-302051.3, and the BCG of A3532 is WINGSJ125721.97-302149.1. According to Lakhchaura et al. (2013) the two clusters are approaching each other for the first time.

A.2 Dynamical states, centers and fractions

Table A.1: P16 clusters that cover 0.7 R_{200}

Cluster	*Chandra*	*XMM-Newton*	Spec. complete	SCF	MCF	Relic	Halo	Flowchart	RA_{fc} (J2000)	DEC_{fc} (J2000)	F_{RPS}^{phot}	F_{RPS}^{spec}
A85	yes	yes	yes	c	a			3	10.46	-9.30	0.06	0.07
A133	yes	yes	yes	l				3	15.67	-21.88	0.31	0.57
A147	no	no	no						17.05	2.19	0.07	
A151	no	yes	yes					2	17.21	-15.41	0.06	0.13
A160	yes	yes	yes					3	18.25	15.49	0.05	0.06
A168	no	yes	yes		e	f		5	18.78	0.32	0.12	0.16
A193	yes	no	yes					2	21.28	8.70	0.00	0.00
A500	no	yes	yes					3	69.72	-22.11	0.22	0.19
A602	no	yes	yes					4	118.36	29.36	0.00	0.00
A754	yes	yes	yes		a	f	f	5	137.23	-9.66	0.00	0.00
A957x	yes	no	yes					3	153.41	-0.93	0.26	0.21
A1069	no	yes	yes					4	159.93	-8.69	0.00	0.00
A1291	no	no	yes						173.10	55.97	0.00	0.00
A1631a	no	no	yes						193.33	-15.53	0.21	0.14
A1668	yes	no	yes					3	195.94	19.27	0.37	0.29
A1795	yes	yes	yes	k				3	207.22	26.59	0.13	0.14
A1831	yes	yes	yes					3	209.81	27.98	0.19	0.00
A1983	no	yes	yes					2	223.23	16.70	0.13	0.12
A1991	yes	yes	yes					2	223.63	18.64	0.20	0.19
A2107	yes	no	yes					2	234.91	21.78	0.00	0.00
A2124	yes	yes	yes					2	236.25	36.11	0.27	0.43
A2149	no	no	yes						240.37	53.95	0.25	0.86
A2169	no	no	yes						243.49	49.19	0.00	0.00
A2382	no	no	yes						327.98	-15.71	0.04	0.00
A2399	no	yes	yes		g			4	329.37	-7.80	0.16	0.14
A2415	yes	yes	yes					4	331.41	-5.59	0.48	0.34
A2457	yes	no	yes					3	338.92	1.48	0.00	0.00
A2593	yes	no	yes						351.08	14.65	0.10	0.00
A2626	yes	yes	yes	i				3	354.13	21.15	0.12	0.19

APPENDIX A. CENTRES FOR COMPUTING FRACTIONS AND VISUAL DYNAMICAL STATE SEQUENCE (FLOWCHART).

Cluster	*Chandra*	*XMM-Newton*	Spec. complete	SCF	MCF	Relic	Halo	Flowchart	RA_{fc} (J2000)	DEC_{fc} (J2000)	F_{RPS}^{phot}	F_{RPS}^{spec}
A2657	yes	yes	yes					3	356.24	9.19	0.00	0.00
A2717	yes	yes	yes					2	0.80	-35.94	0.00	0.00
A2734	yes	yes	yes					2	2.84	-28.85	0.84	0.00
A3128	yes	yes	yes					3	52.46	-52.58	0.00	0.00
A3158	yes	yes	yes		m			4	55.72	-53.63	0.28	0.14
A3266	yes	yes	yes		a	n	n	5	67.81	-61.45	0.04	0.04
A3376	yes	yes	yes		j	f		5	90.37	-39.99	0.08	0.08
A3490	no	yes	no					3	176.34	-34.43	0.47	
A3528	yes	yes	yes					1	193.63	-29.12	0.00	0.00
A3530/32	yes	yes	yes					1	194.12	-30.36	0.18	0.17
A3556	no	no	yes						201.03	-31.67	0.00	0.00
A3558	yes	yes	yes	b				3	201.99	-31.50	0.05	0.07
A3560	yes	yes	yes	d				3	203.18	-33.14	0.10	0.10
A3667	yes	yes	yes		a	f		5	302.91	-56.75	0.06	0.07
A3716	yes	yes	yes					1	313.01	-52.71	0.10	0.00
A3809	yes	no	yes					3	326.75	-43.90	0.00	0.00
A3880	yes	no	yes					2	336.98	-30.58	0.11	0.14
A4059	yes	yes	yes	h				3	359.25	-34.76	0.06	0.09
RX1022	yes	yes	no					3	155.54	38.52	0.00	
RX1740	no	yes	yes					2	265.13	35.65	0.00	
MKW3s	yes	yes	yes					2	230.47	7.71	0.00	0.00
Z2844	no	yes	yes					2	150.65	32.71	0.00	0.00
IIZW108	yes	no	yes					3	318.48	2.57	0.00	0.00

[a] Ghizzardi et al. (2010)

[b] Rossetti et al. (2007)

[c] Ichinohe et al. (2015)

[d] Venturi et al. (2013)

[e] Hallman & Markevitch (2004)

[f] van Weeren et al. (2019, and references therein)

[g] Mitsuishi et al. (2018)

[h] Laganá et al. (2010)

[i] Ignesti et al. (2018)

[j] Urdampilleta et al. (2018)

[k] Walker et al. (2014)

[l] Randall et al. (2010)

[m] Wang et al. (2010)

[n] Riseley et al. (2022)

APPENDIX B

Cluster gallery

In this appendix, we show clusters from our sample (Sec. 2) with X-ray data either from *Chandra* or *XMM*-Newton, along with the spectroscopic members and RPS candidates with their tail directions identified by Salinas et al. (submitted) and substructures identified with the DS+ method.

Figure B.1: RPS candidates are shown as filled black stars. The arrows indicate the direction of the tails in the RPS candidates, which, in principle, point in the opposite direction of movement (Salinas et al. submitted). The filled-coloured circles represent the substructures identified in B17. The blue x's and open circles represent blue and spiral galaxies, respectively. Black contours highlight the X-ray emission from ***Chandra***, and red ellipses show the positions and orientations of the three brightest galaxies. The dashed black circles show 0.5 R_{200}, R_{200}, and 1.5 R_{200}, respectively.

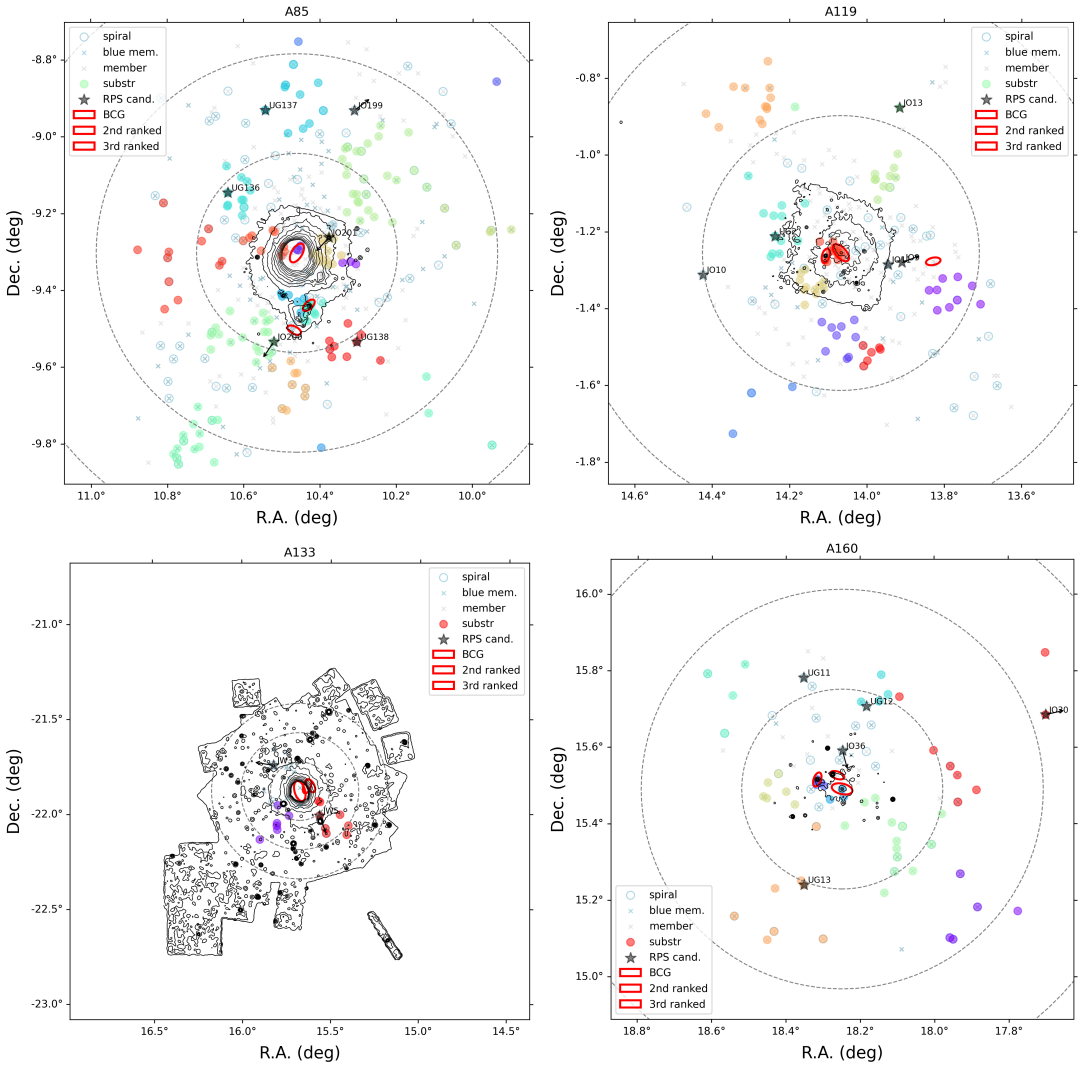

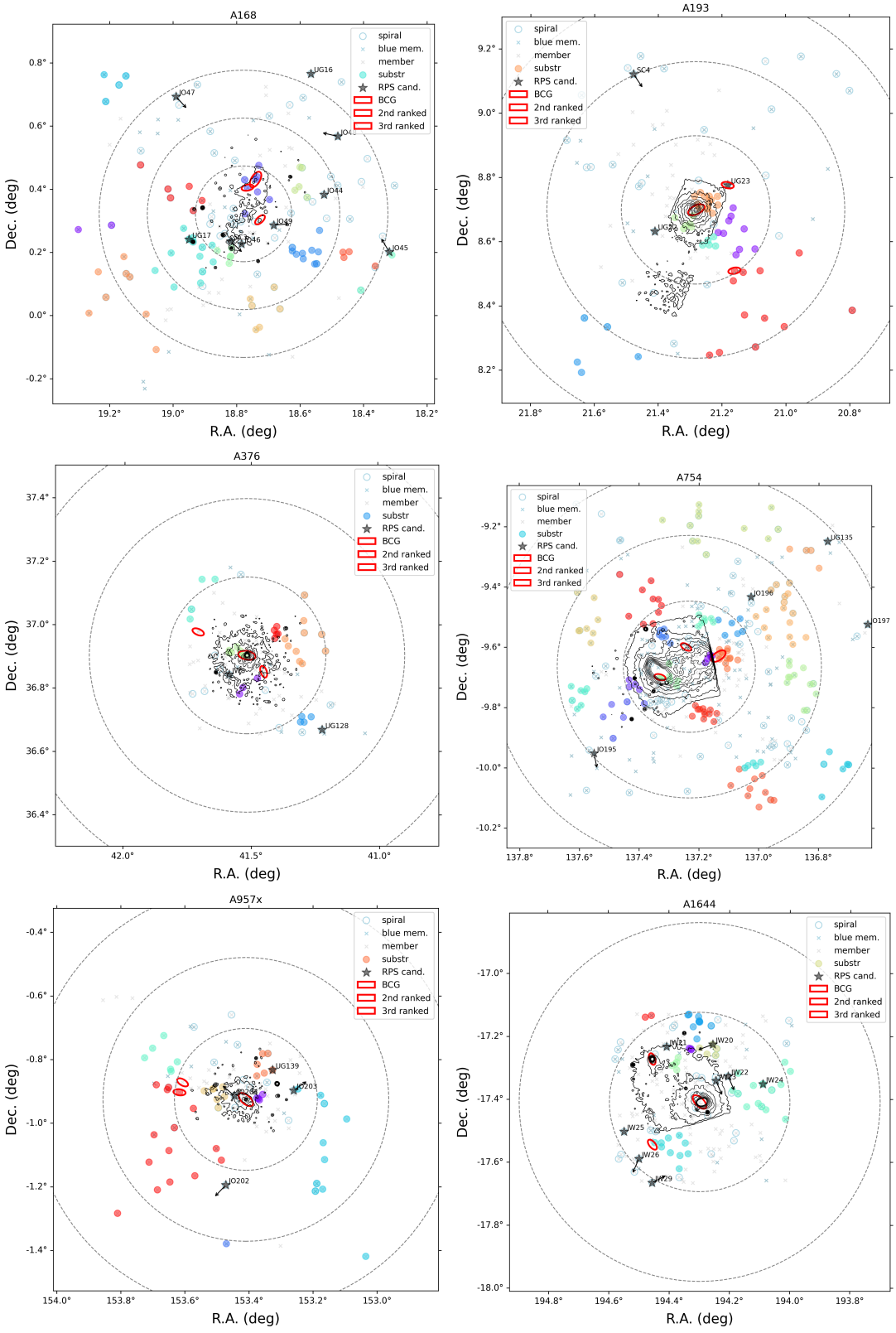
A168
A193
A376
A754
A957x
A1644
spiral
blue mem.
member
substr
RPS cand.
BCG
2nd ranked
3rd ranked
Dec. (deg)
R.A. (deg)

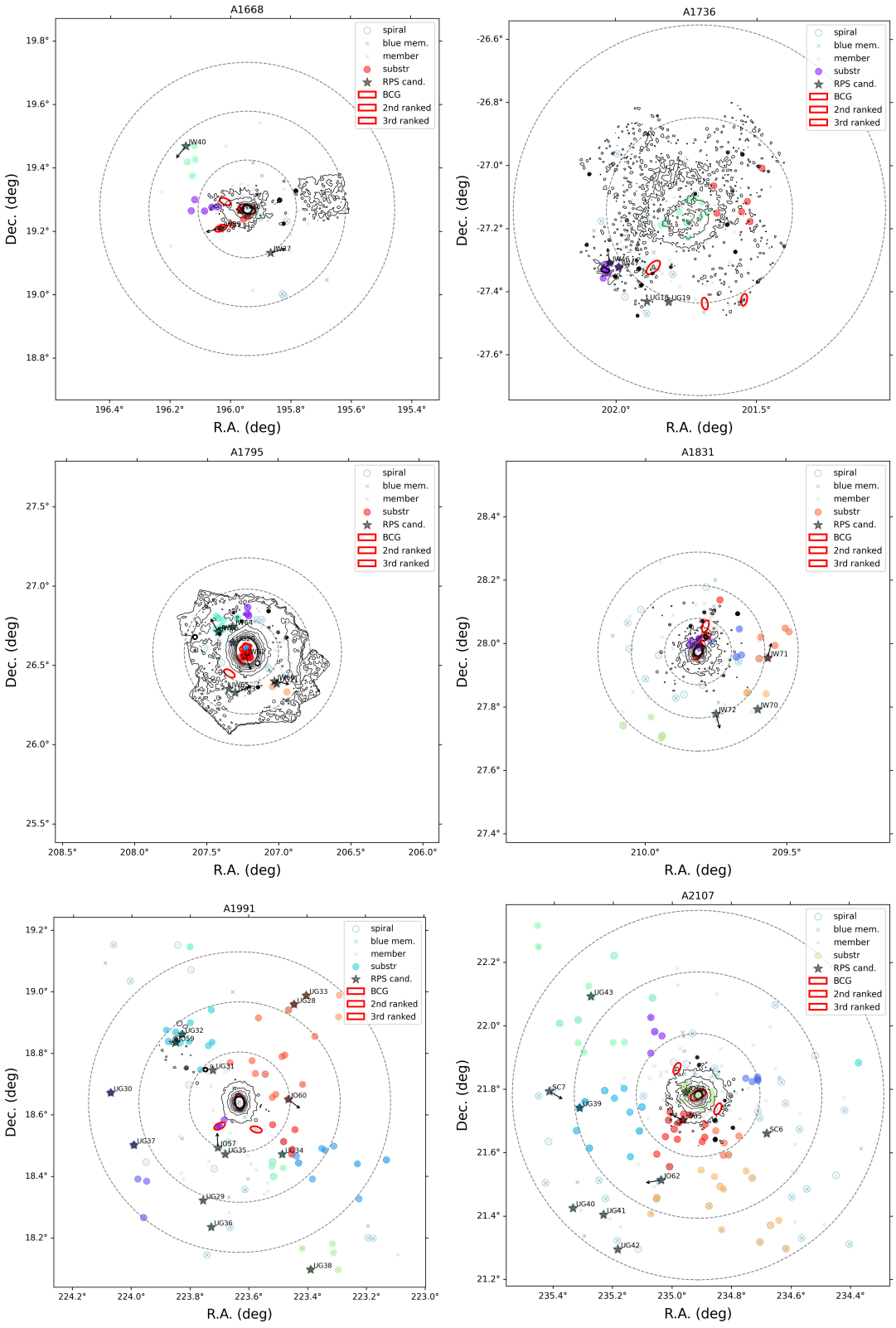
A1668
A1736
A1795
A1831
A1991
A2107
spiral
blue mem.
member
substr
RPS cand.
BCG
2nd ranked
3rd ranked
Dec. (deg)
R.A. (deg)

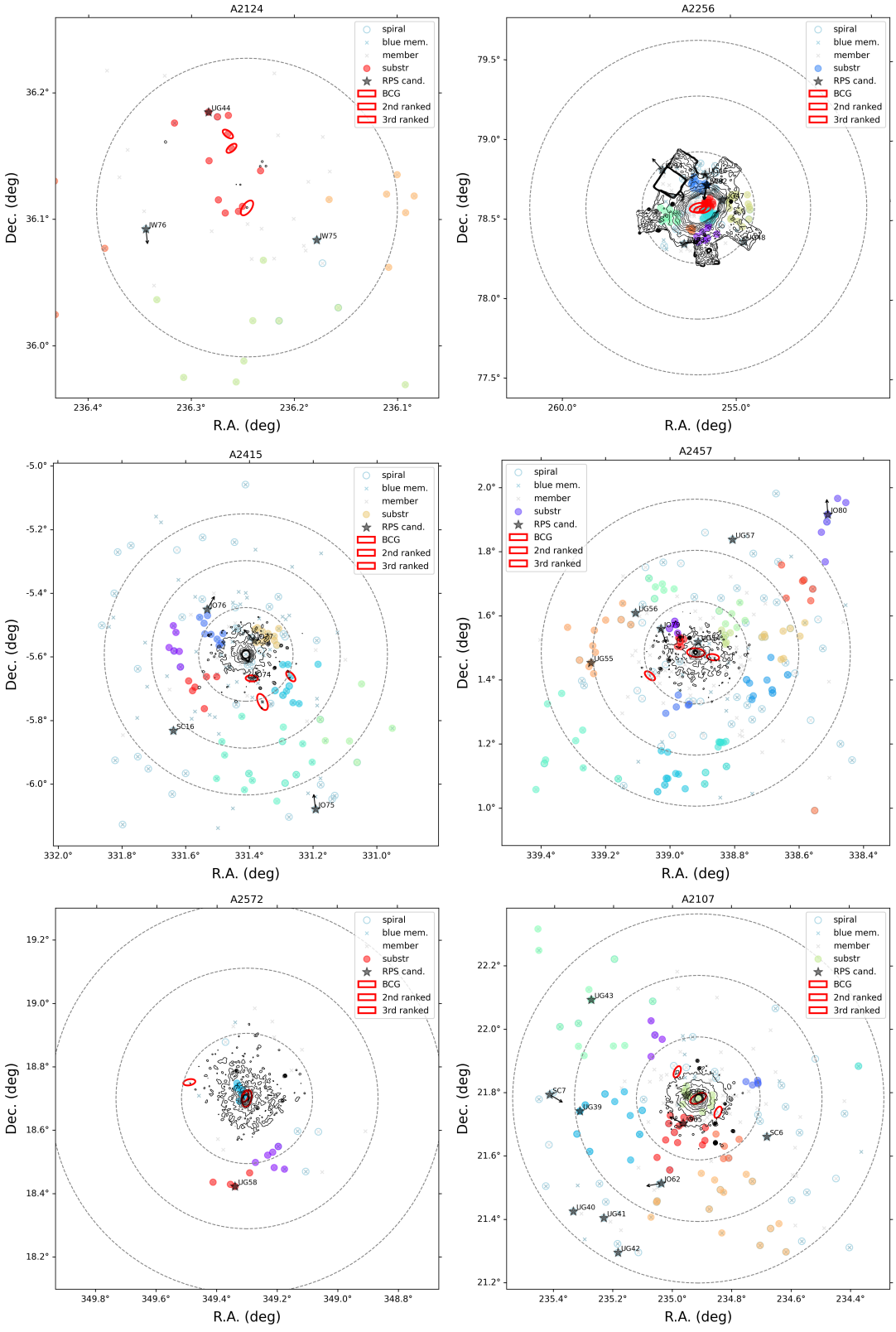
A2124
A2256
A2415
A2457
A2572
A2107
spiral
blue mem.
member
substr
RPS cand.
BCG
2nd ranked
3rd ranked
Dec. (deg)
R.A. (deg)

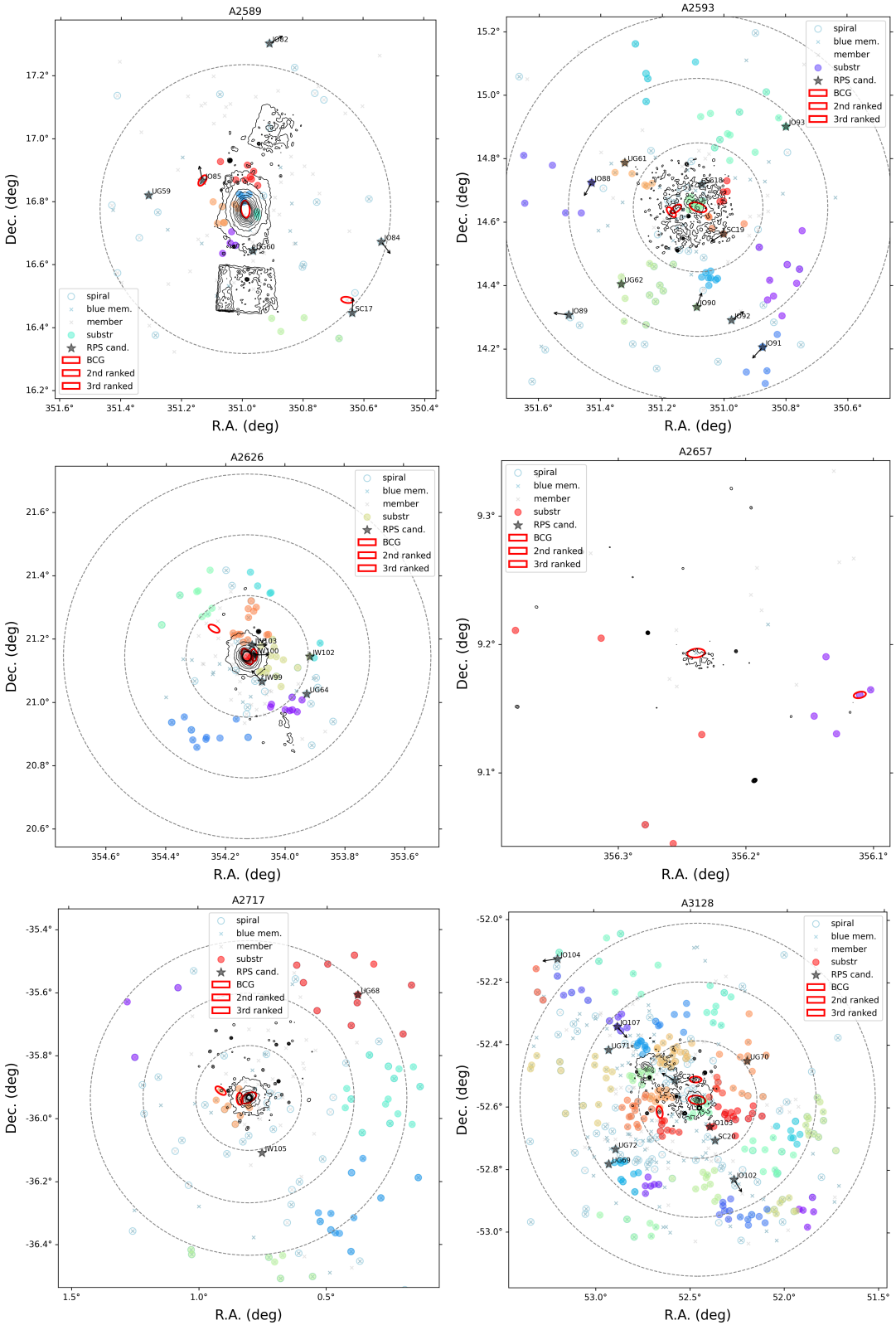
A2589
A2593
A2626
A2657
A2717
A3128
spiral
blue mem.
member
substr
RPS cand.
BCG
2nd ranked
3rd ranked
Dec. (deg)
R.A. (deg)

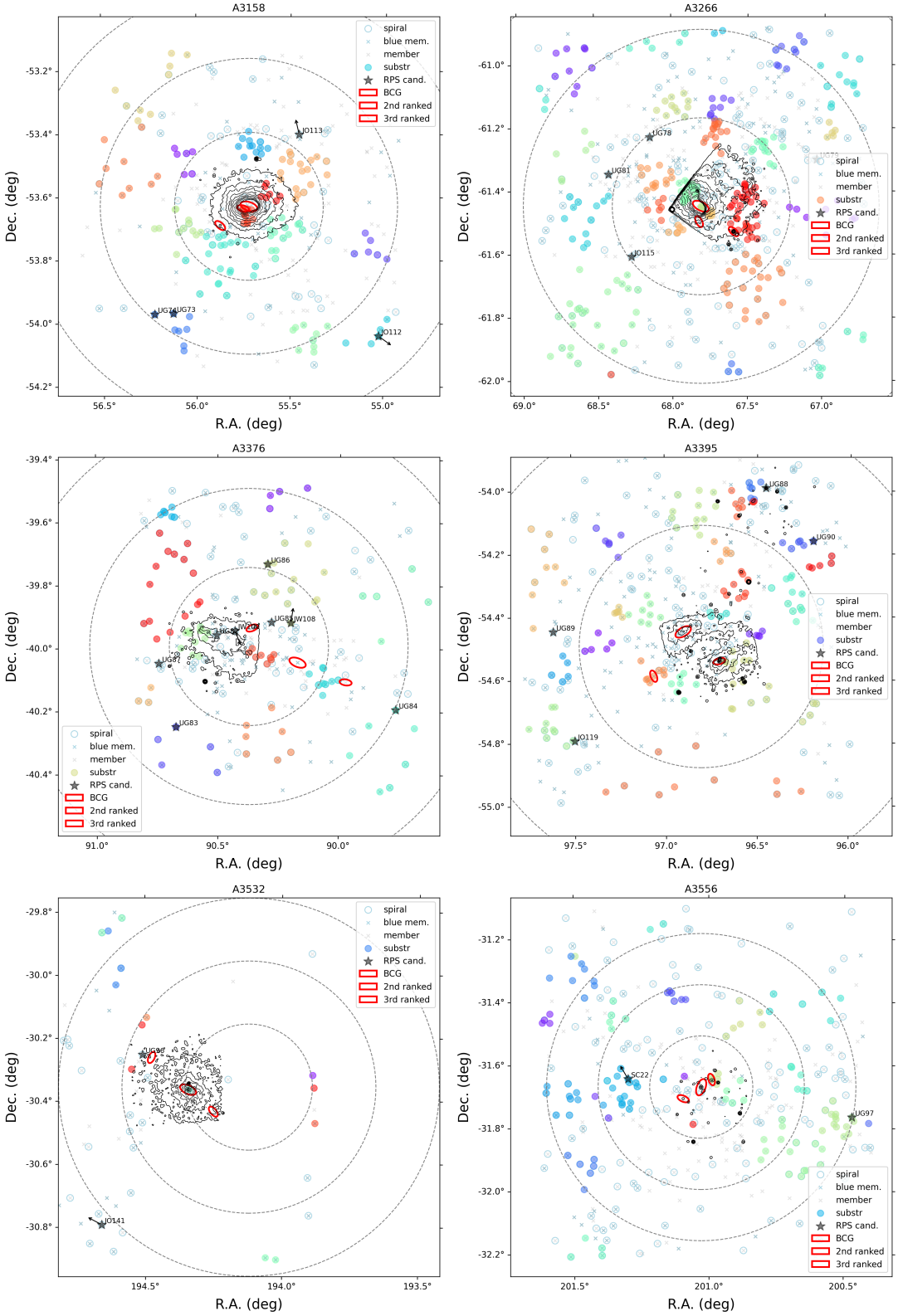
A3158
A3266
A3376
A3395
A3532
A3556
Dec. (deg)
R.A. (deg)
spiral
blue mem.
member
substr
RPS cand.
BCG
2nd ranked
3rd ranked
JO113
JO112
UG74
UG73
UG78
UG81
JO115
UG86
UG85
IW108
UG84
UG83
UG88
UG90
UG89
JO119
UG96
JO141
SC22
UG97

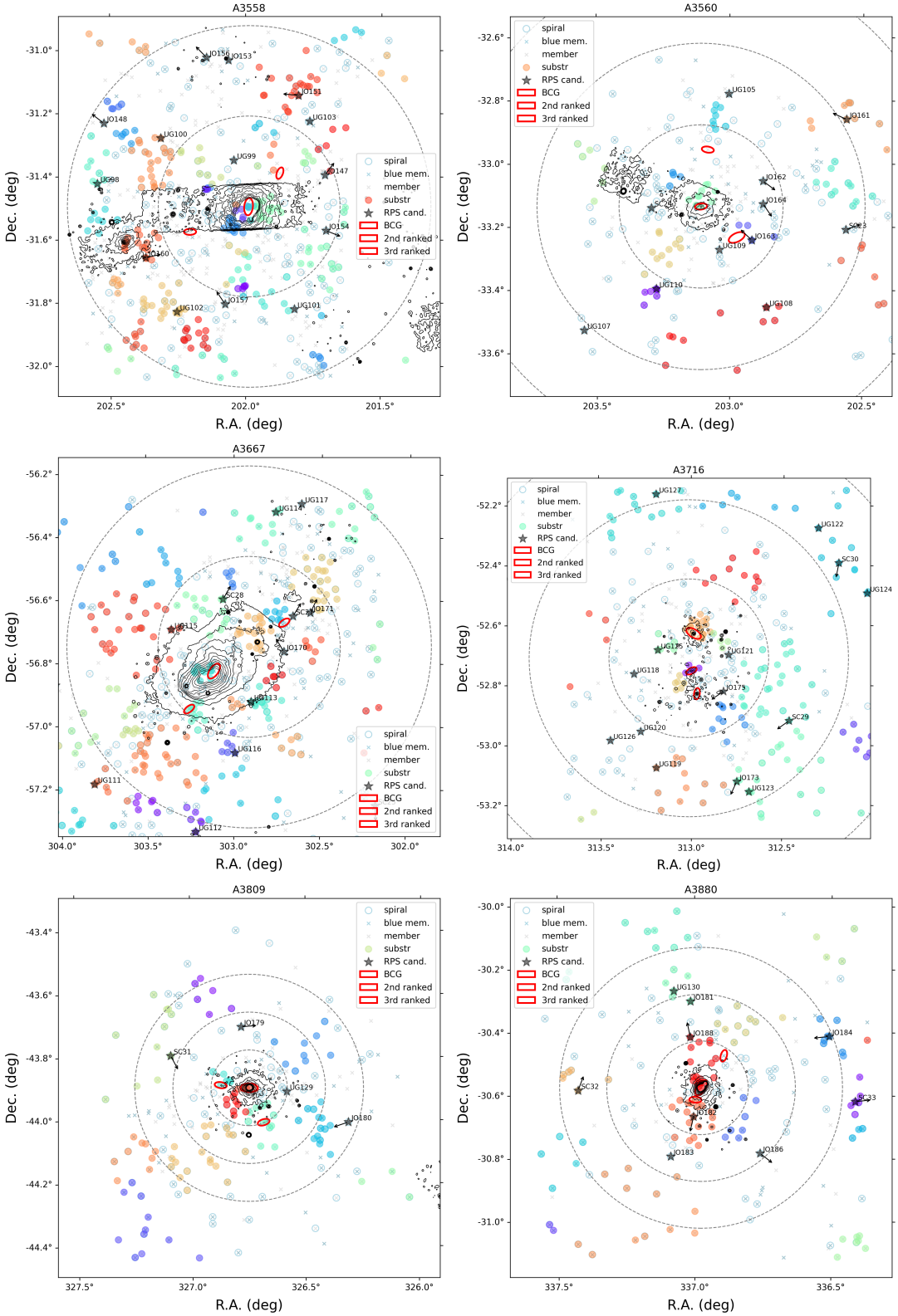
A3558
A3560
A3667
A3716
A3809
A3880
spiral
blue mem.
member
substr
RPS cand.
BCG
2nd ranked
3rd ranked
Dec. (deg)
R.A. (deg)

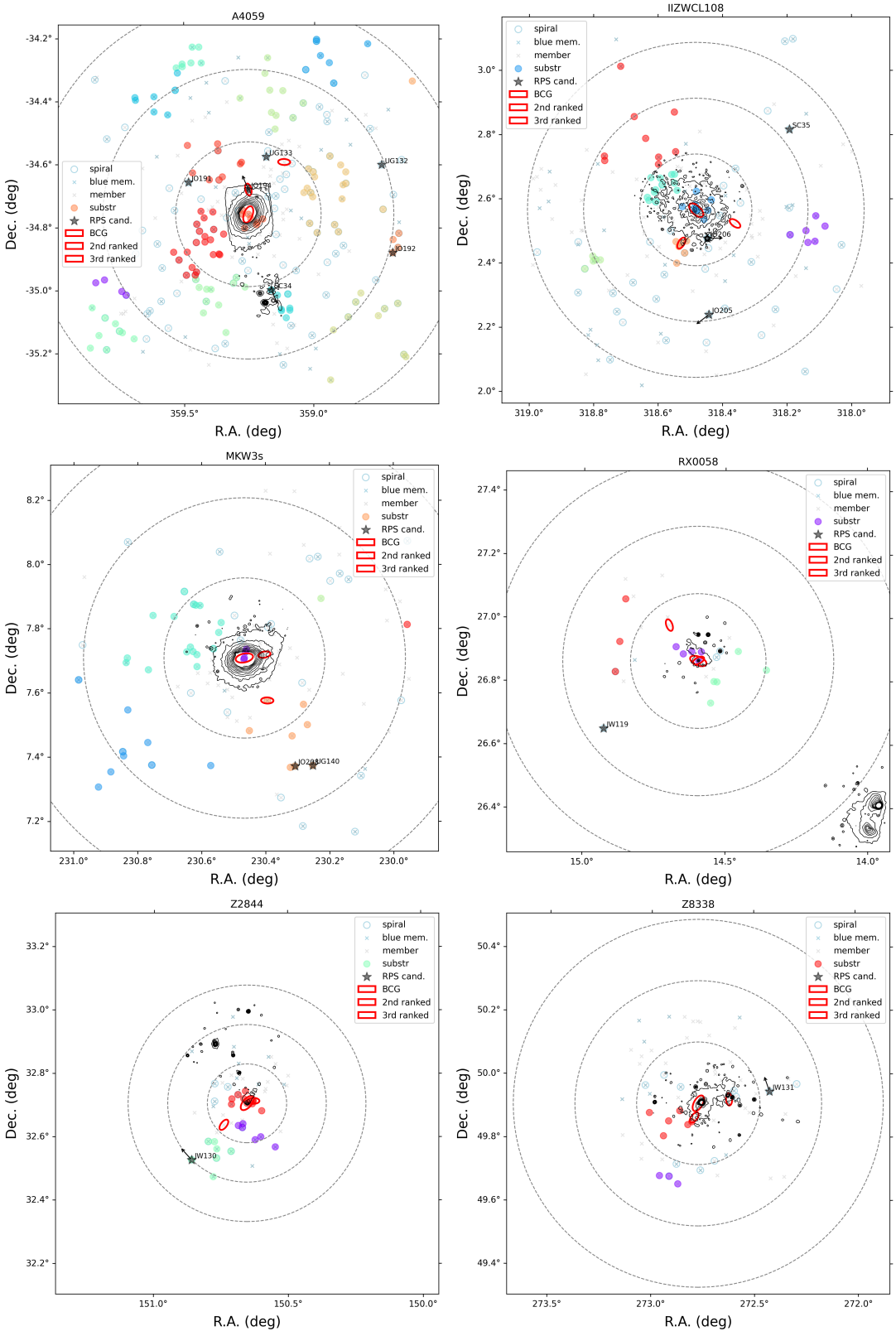
A4059
IIZWCL108
MKW3s
RX0058
Z2844
Z8338
spiral
blue mem.
member
substr
RPS cand.
BCG
2nd ranked
3rd ranked
Dec. (deg)
R.A. (deg)
UG133
UG132
JO191
JO192
JO206
JO205
SC35
JW119
JW130
JW131
UG140

Figure B.2: RPS candidates are shown as filled black stars. The arrows indicate the direction of the tails in the RPS candidates, which, in principle, point in the opposite direction of movement (Salinas et al. submitted). The filled-coloured circles represent the substructures identified in B17. The blue x's and open circles represent blue and spiral galaxies, respectively. Black contours highlight the X-ray emission from ***XMM-Newton***, and red ellipses show the positions and orientations of the three brightest galaxies. The dashed black circles show 0.5 R_{200}, R_{200}, and 1.5 R_{200}, respectively.

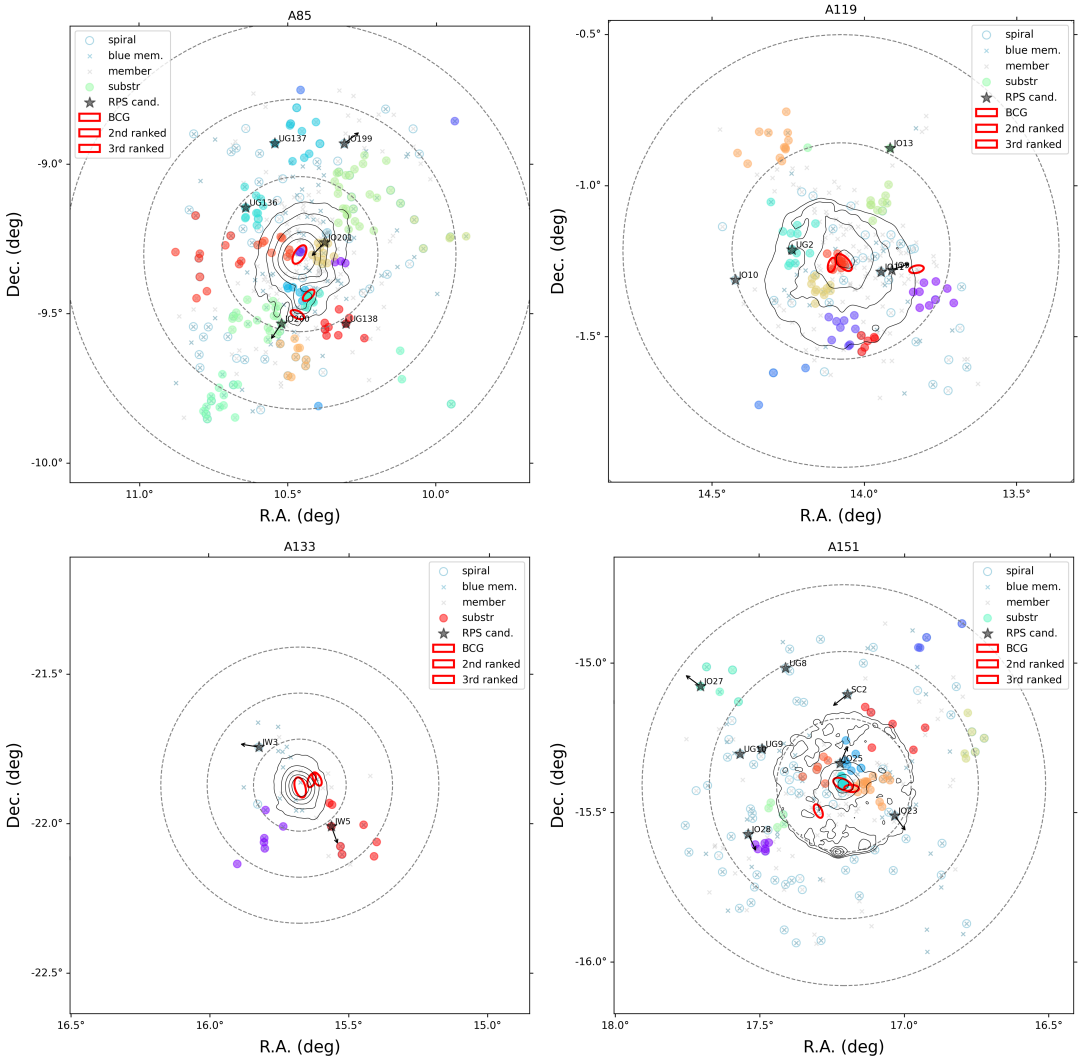

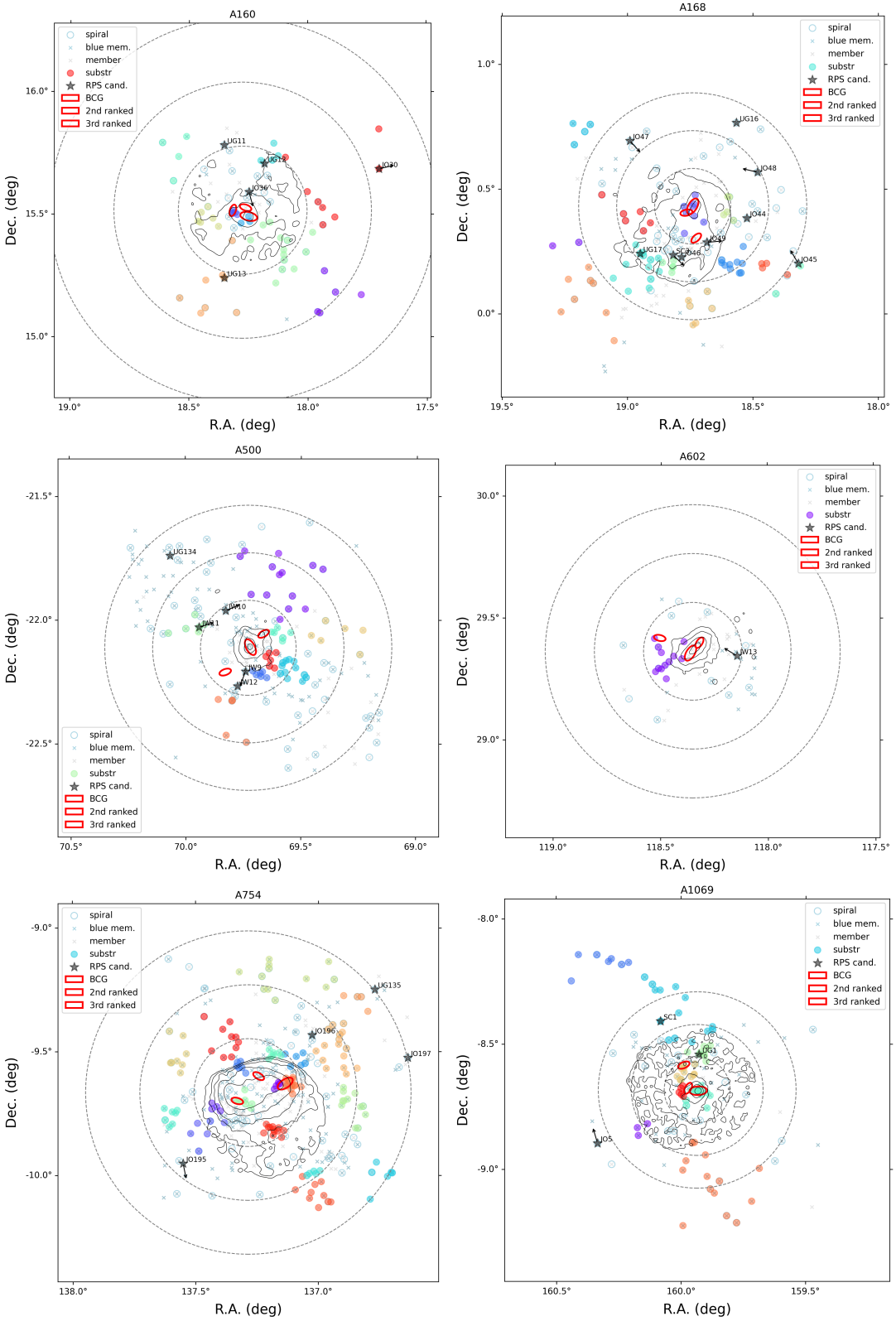
A160
A168
A500
A602
A754
A1069
spiral
blue mem.
member
substr
RPS cand.
BCG
2nd ranked
3rd ranked
Dec. (deg)
R.A. (deg)

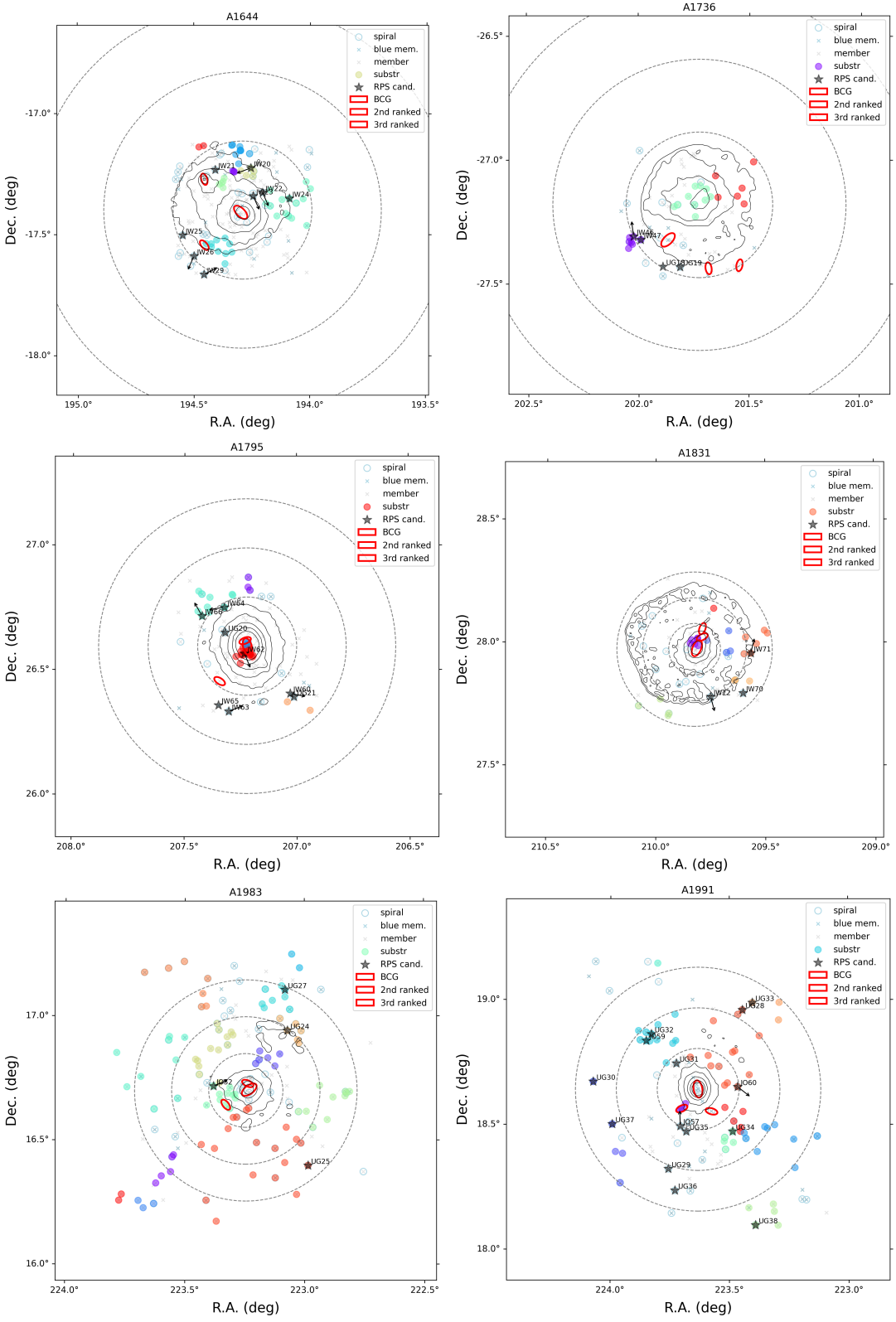
A1644
A1736
A1795
A1831
A1983
A1991
spiral
blue mem.
member
substr
RPS cand.
BCG
2nd ranked
3rd ranked
Dec. (deg)
R.A. (deg)

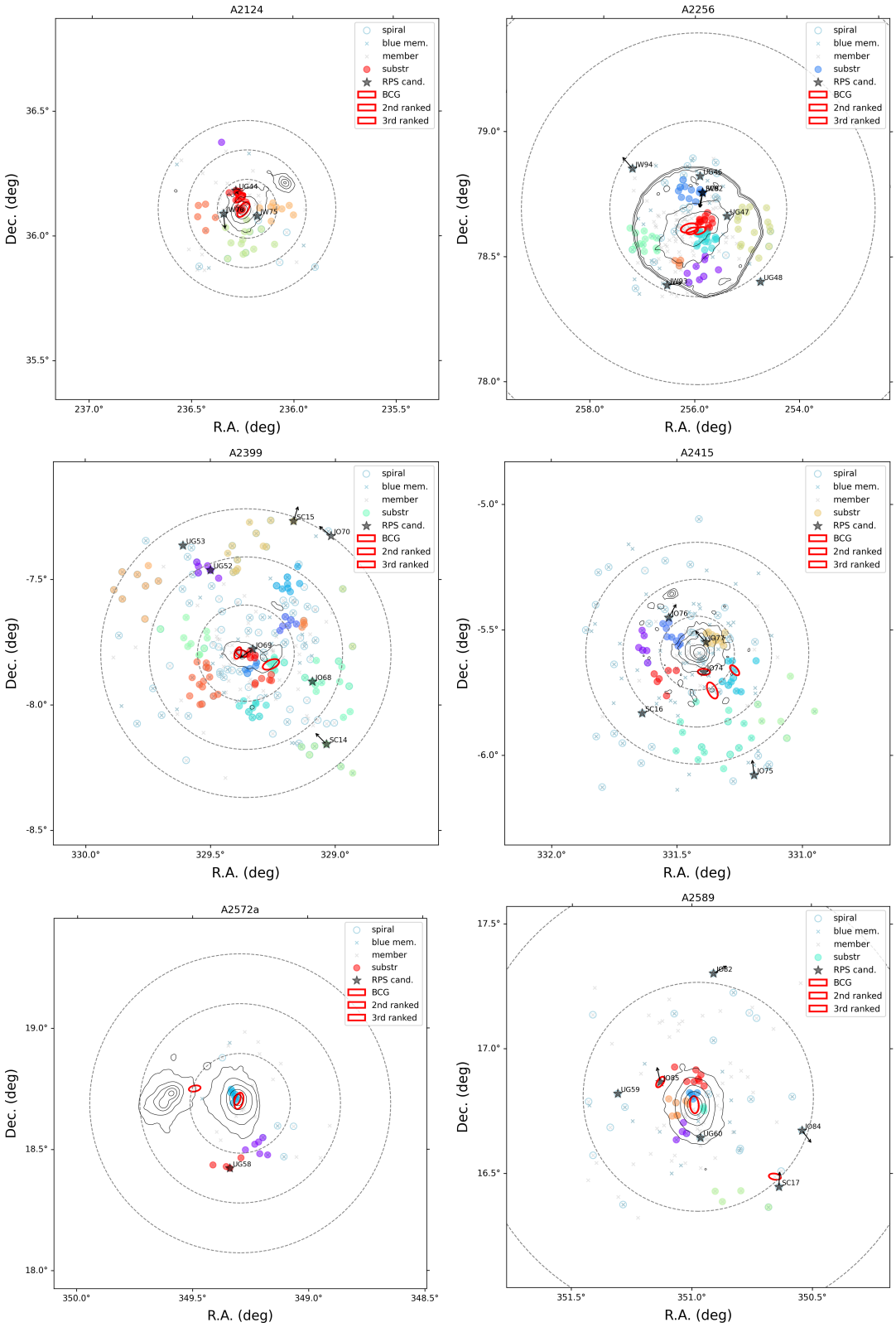
A2124
A2256
A2399
A2415
A2572a
A2589
spiral
blue mem.
member
substr
RPS cand.
BCG
2nd ranked
3rd ranked
Dec. (deg)
R.A. (deg)
UG44
UW76
UW75
UW94
UG46
UG47
UG48
UW93
SC15
UO70
UG53
UG52
UO69
UO68
SC14
UO76
UO77
UO74
SC16
UO75
UG58
UO82
UO85
UG59
UG60
UO84
SC17

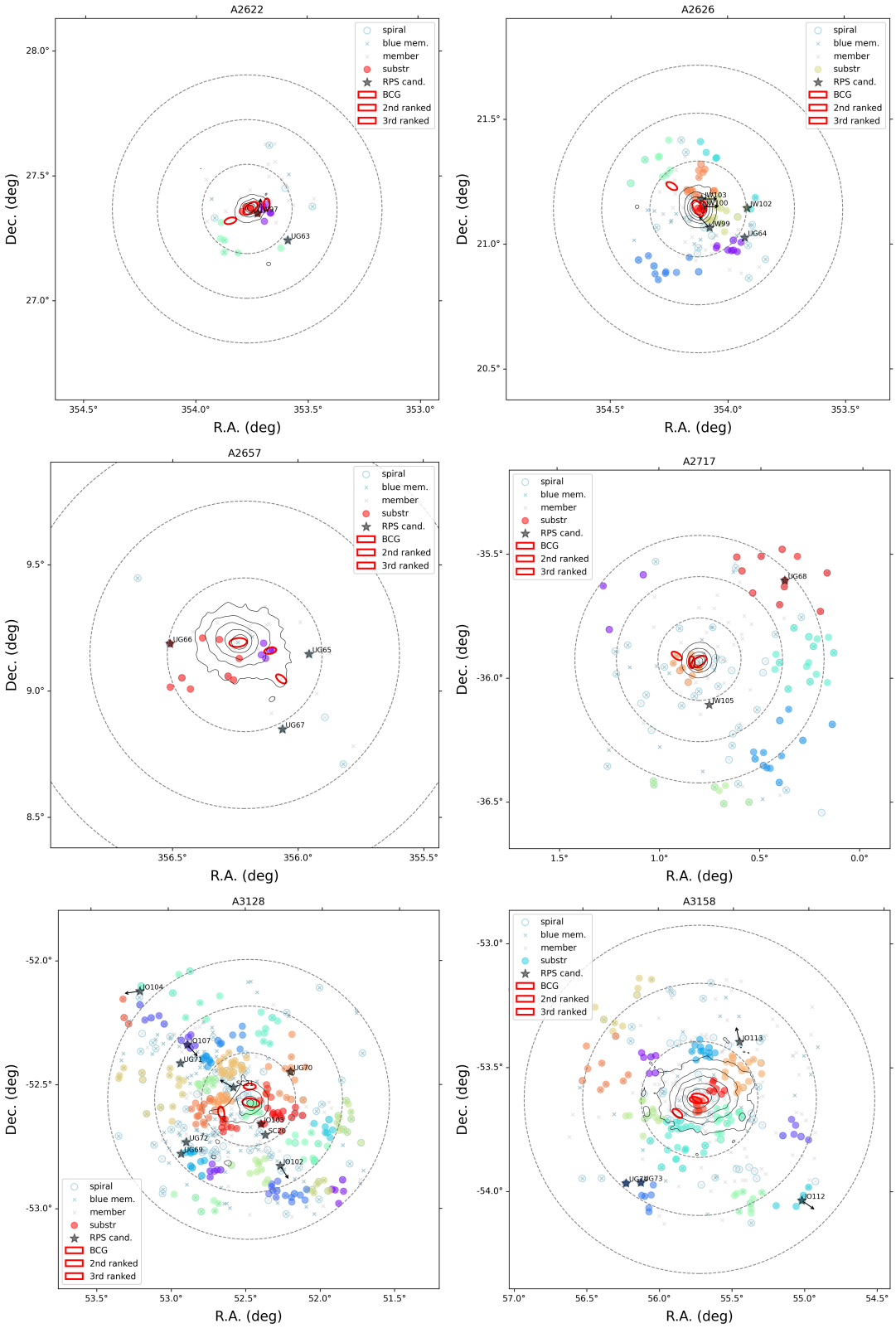
A2622
A2626
A2657
A2717
A3128
A3158
spiral
blue mem.
member
substr
RPS cand.
BCG
2nd ranked
3rd ranked
Dec. (deg)
R.A. (deg)

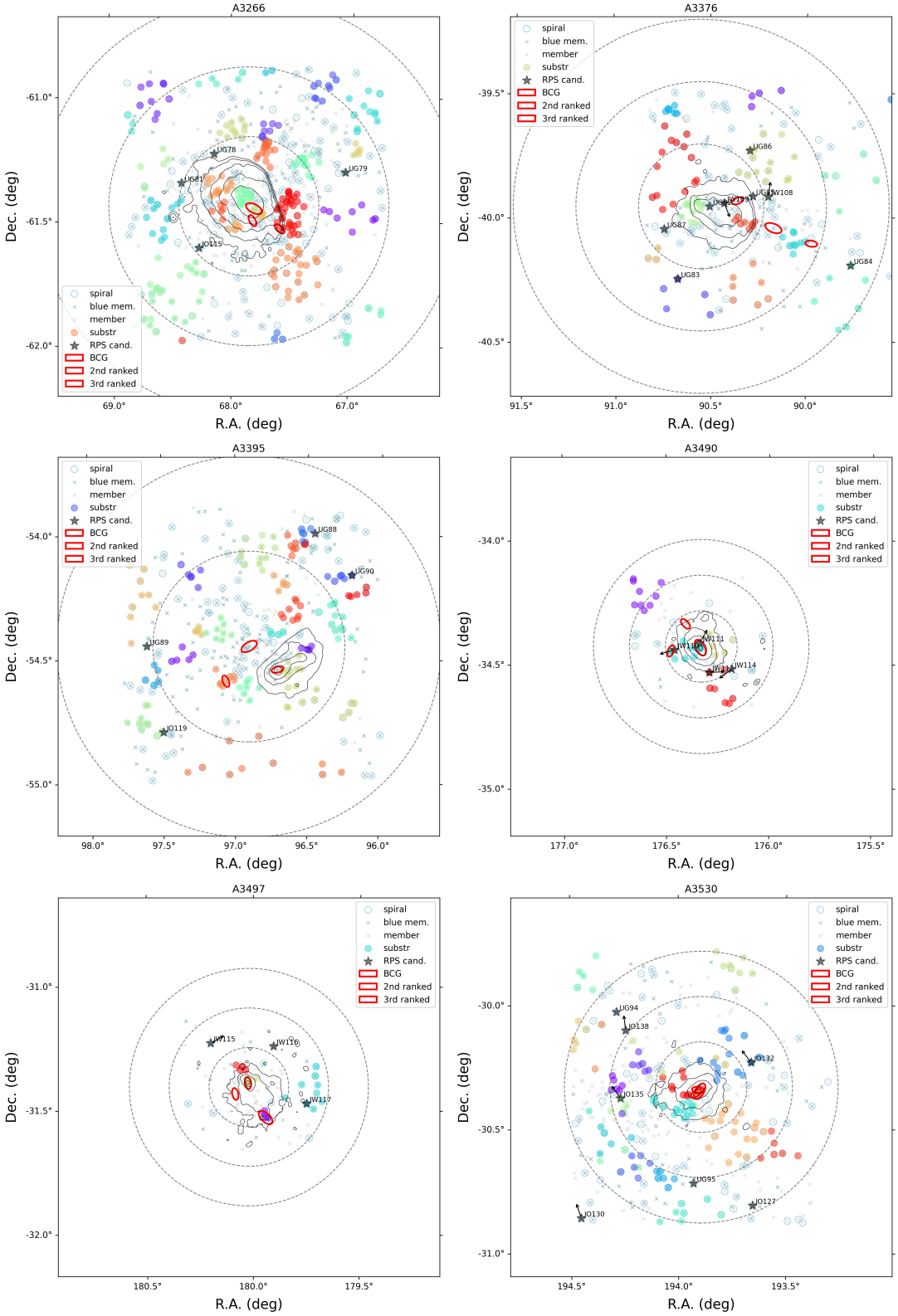
A3266
A3376
A3395
A3490
A3497
A3530
spiral
blue mem.
member
substr
RPS cand.
BCG
2nd ranked
3rd ranked
Dec. (deg)
R.A. (deg)
-61.0°
-61.5°
-62.0°
69.0°
68.0°
67.0°
-39.5°
-40.0°
-40.5°
91.5°
91.0°
90.5°
90.0°
-54.0°
-54.5°
-55.0°
98.0°
97.5°
97.0°
96.5°
96.0°
-34.0°
-34.5°
-35.0°
177.0°
176.5°
176.0°
175.5°
-31.0°
-31.5°
-32.0°
180.5°
180.0°
179.5°
-30.0°
-30.5°
-31.0°
194.5°
194.0°
193.5°
UG78
UG79
UG81
JO115
UG86
UG87
UG83
UG84
UG88
UG90
UG89
JO119
JW111
JW113
JW114
JW115
JW116
JW117
UG94
JO138
JO132
JO135
UG95
JO127
JO130

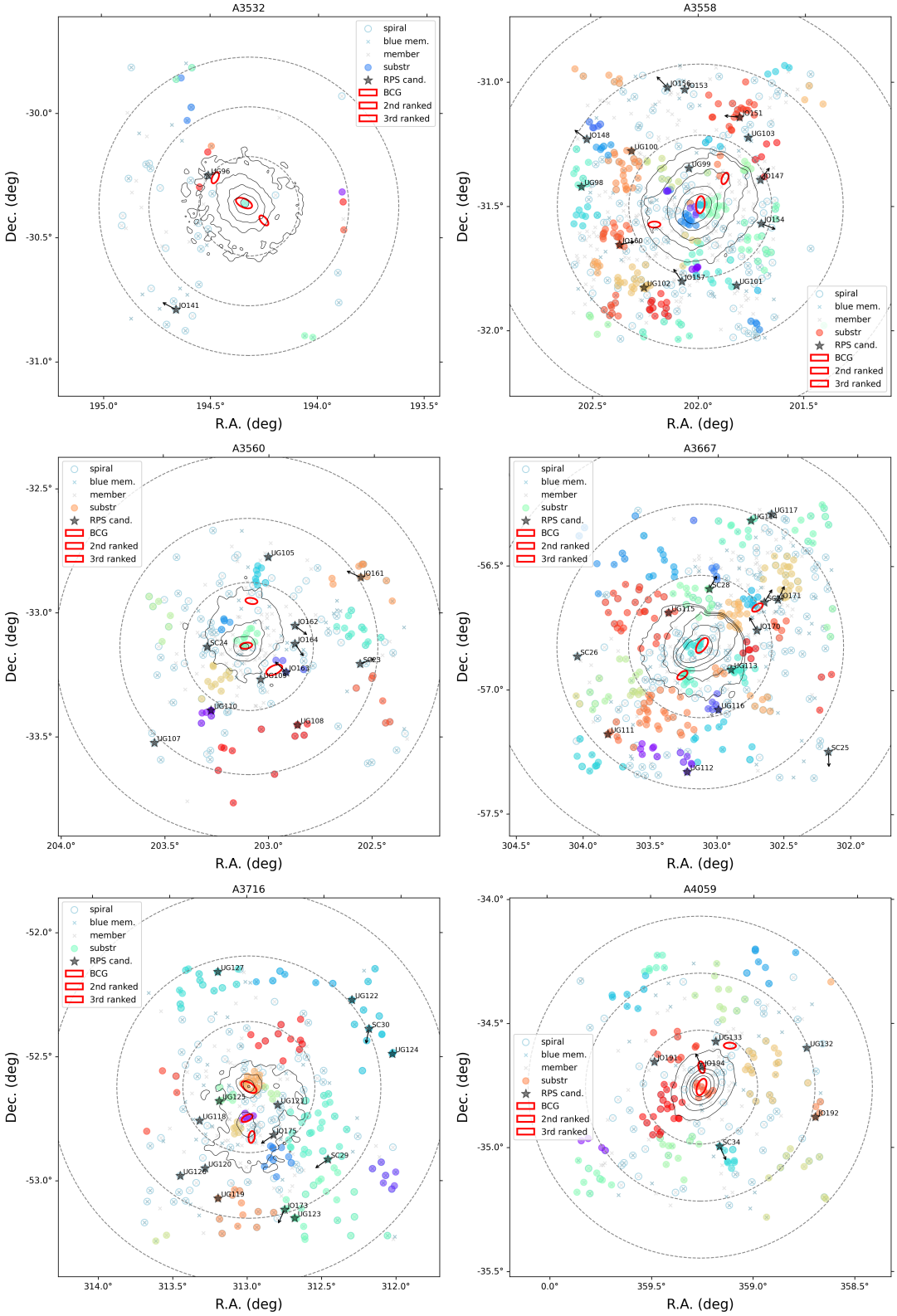
A3532
A3558
A3560
A3667
A3716
A4059
spiral
blue mem.
member
substr
RPS cand.
BCG
2nd ranked
3rd ranked
Dec. (deg)
R.A. (deg)

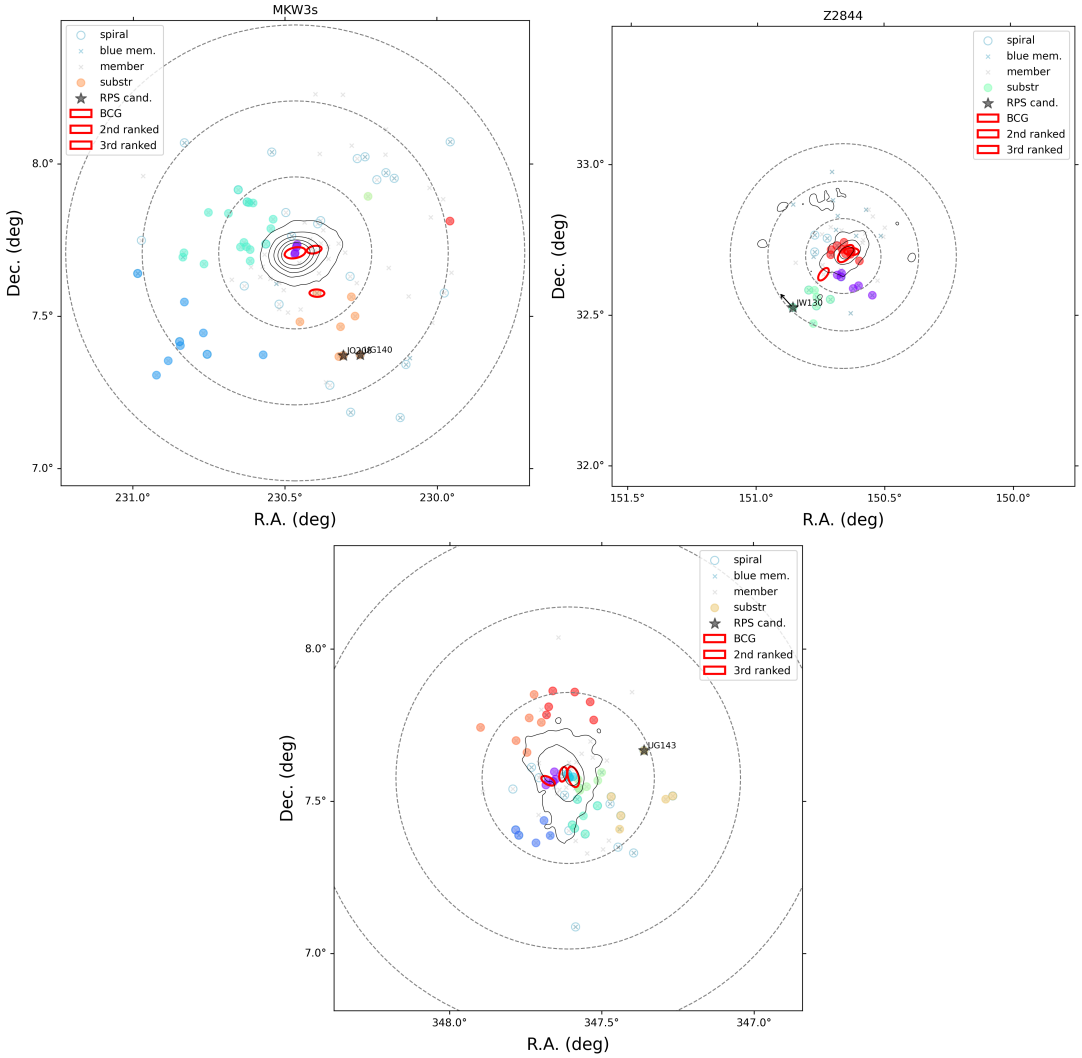
MKW3s
Z2844
spiral
blue mem.
member
substr
RPS cand.
BCG
2nd ranked
3rd ranked
Dec. (deg)
R.A. (deg)
8.0°
7.5°
7.0°
231.0°
230.5°
230.0°
33.0°
32.5°
32.0°
151.5°
151.0°
150.5°
150.0°
IW139
IG140
IG143
348.0°
347.5°
347.0°

APPENDIX C

List of publications and telescope proposals

Publications

- Soares-Santos et al. *The Electromagnetic Counterpart of the Binary Neutron Star Merger LIGO/Virgo GW170817. I. Discovery of the Optical Counterpart Using the Dark Energy Camera*. The Astrophysical Journal, v. 848, p. L16, 2017.
- Cowperthwaite et al. *The Electromagnetic Counterpart of the Binary Neutron Star Merger LIGO/Virgo GW170817. II. UV, Optical, and Near-infrared Light Curves and Comparison to Kilonova Models*. The Astrophysical Journal, v. 848, p. L17, 2017.
- Abbott et al. *Multi-messenger Observations of a Binary Neutron Star Merger*. The Astrophysical Journal, v. 848, p. L12, 2017.
- Abbott et al. *A gravitational-wave standard siren measurement of the Hubble constant*. NATURE, v. 551, p. 85-88, 2017.
- Soares-Santos et al. *VizieR Online Data Catalog: Counterpart of GW170817. I. DECam obs. (Soares-Santos+, 2017)*.
- **Lourenço, A. C. C.** et al. *The dynamical state of A2399: A bullet-like cluster*. MNRAS 2020. v. 498, p. 835-849.
- Campitiello, M. G. et al. *GASP XXXIV: Unfolding the Thermal Side of Ram Pressure Stripping in the Jellyfish Galaxy JO201*. ApJ, v. 911, p. 144, 2021.

- Müller et al. *Two Striking Head-tail galaxies in the galaxy cluster IIZW108: insights into transition to turbulence, magnetic fields, and particle re-acceleration*. MNRAS, v. 508, p. 5326-5344, 2021.
- Zaratiski, D. et al. *An enigmatic 380 kpc long linear collimated galactic tail*. MNRAS, v. 524, p. 1431-1437, 2023.
- **Lourenço, A. C. C.** et al. *The effect of cluster dynamical state on ram-pressure stripping*. MNRAS, v. 526, p. 4831-4847, 2023.
- Kelkar, K., Jaffe, Y., **Lourenço, A. C. C.** et al. *Post-processing of galaxies due to major cluster mergers I. hints from galaxy colours and morphologies*. A & A, v. 680, p. 54-69, 2023.
- Piraino, F., Jaffe, Y., **Lourenço, A. C. C.** et al. Pre- and post-processing of cluster galaxies out to 5×R200: The extreme case of A2670. MNRAS, v. 528, p. 919-936, 2024.
- Biviano, A., Poggianti, B., Jaffe, Y., **Lourenço, A. C. C.** et al. *The radial orbits of ram-pressure-stripped galaxies in clusters*. ApJ, v. 965, p. 117, 2024.
- Kim, D. et al. *Distribution of ongoing and post-merging galaxies in nearby galaxy clusters.* A & A, v. 966, p. 124-141, 2024.
- Salinas, V. et al. *Reconstructing the journey of cluster galaxies through jellyfish galaxy tails* (Submitted to MNRAS).
- Crossett, J. et al. *Identification of ram pressure stripping features in galaxies using citizen science* (Submitted to A&A).
- **Lourenço, A. C. C.** et al. *The role of ram pressure stripping on galaxy pre-processing*. (In prep.).

Proceedings

- **Lourenço, A. C. C.**, & Jaffé, Y. L. (2021). *Jellyfish galaxies in violent neighbourhoods*. Extragalactic Spectroscopic Surveys: Past, Present and Future of Galaxy Evolution (GALSPEC2021), Online. Zenodo. https://doi.org/10.5281/zenodo.4721530.
- **Lourenço, A. C. C.** *Is ram pressure enhanced by cluster mergers?*. Galaxy Cluster Formation 2021 (GCF2021), Online. Zenodo. https://doi.org/10.5281/zenodo.5022208.

Telescope Allocated Time as P.I.

- Lourenço, A. C. C. et al. DECAM @ CTIO (ID: 2022B-791264 - 4 half nights).
- Lourenço, A. C. C. et al. IMACS @ LCO (ID: CN2023B-61 - 1 night).

Telescope Allocated Time as Co-I.

- Lopes. P. et al. DECam @ CTIO (ID: 2017B-0904 - 2 half nights)
- Jaffé, Y. et al. T80 @ CTIO (ID: 2020B - 10 nights).

– Kelkar, K. et al. DECAM @ CTIO (ID: 2022A-975778 - 1 night).
– Crossett, J. et al. IMACS @ LCO (ID: CN2022B- - 2 half nights).
– Mueller, A. et al. VLA (ID: 22B-067 - 311 hours).

Bibliography

, 1864, A General Catalogue of Nebulae and Clusters of Stars: Arranged in Order of Right Ascension and Reduced to the Common Epoch 1860.0. Taylor & Francis

Ahn C. P. et al., 2014, ApJS, 211, 17

Akamatsu H., Takizawa M., Nakazawa K., Fukazawa Y., Ishisaki Y., Ohashi T., 2012, PASJ, 64, 67

Alam S. et al., 2015, ApJS, 219, 12

Alpaslan M. et al., 2016, MNRAS, 457, 2287

Ando M., Shimasaku K., Ito K., 2023, MNRAS, 519, 13

Andrade-Santos F. et al., 2017, ApJ, 843, 76

Andrade-Santos F. et al., 2015, ApJ, 803, 108

Arnaud K., Smith R., Siemiginowska A., 2011, Handbook of X-ray Astronomy

Ascasibar Y., Markevitch M., 2006, ApJ, 650, 102

Bacchi M., Feretti L., Giovannini G., Govoni F., 2003, A&A, 400, 465

Bagchi J., Durret F., Neto G. B. L., Paul S., 2006, Science, 314, 791

Baldi A., Bardelli S., Zucca E., 2001, MNRAS, 324, 509

Baldwin J. A., Phillips M. M., Terlevich R., 1981, PASP, 93, 5

Bardelli S., Zucca E., Baldi A., 2001, MNRAS, 320, 387

Bekki K., 2009, MNRAS, 399, 2221

Bellhouse C. et al., 2021, MNRAS, 500, 1285

Benavides J. A., Biviano A., Abadi M. G., 2023, A&A, 669, A147

Benavides J. A., Sales L. V., Abadi M. G., 2020, Monthly Notices of the Royal Astronomical Society, 498, 3852

Bilton L. E., Hunt M., Pimbblet K. A., Roediger E., 2019, MNRAS, 490, 5017

Binggeli B., 1982, A&A, 107, 338

Birnboim Y., Keshet U., Hernquist L., 2010, MNRAS, 408, 199

Biviano A. et al., 2017, A&A, 607, A81

Biviano A., Poggianti B. M., Jaffé Y., Lourenço A. C., Pizzuti L., Moretti A., Vulcani B., 2024, ApJ, 965, 117

Boselli A. et al., 2016a, A&A, 587, A68

Boselli A., Fossati M., Sun M., 2021, arXiv e-prints, arXiv:2109.13614

Boselli A., Gavazzi G., 2006, PASP, 118, 517

Boselli A. et al., 2016b, A&A, 596, A11

Botteon A., Gastaldello F., Brunetti G., 2018, MNRAS, 476, 5591

Briel U. G., Finoguenov A., Henry J. P., 2004, A&A, 426, 1

Brunetti G., Jones T. W., 2014, International Journal of Modern Physics D, 23, 1430007

Buote D. A., Tsai J. C., 1995, ApJ, 452, 522

Byrd G., Valtonen M., 1990, ApJ, 350, 89

Calvi R., Poggianti B. M., Fasano G., Vulcani B., 2012, MNRAS, 419, L14

Calvi R., Poggianti B. M., Vulcani B., 2011, MNRAS, 416, 727

Cameron E., 2011, PASA, 28, 128

Campitiello M. G. et al., 2022, A&A, 665, A117

Cassano R. et al., 2013, ApJ, 777, 141

Cassano R., Ettori S., Giacintucci S., Brunetti G., Markevitch M., Venturi T., Gitti M., 2010, ApJ, 721, L82

Cautun M., van de Weygaert R., Jones B. J. T., Frenk C. S., 2014, MNRAS, 441, 2923

Cava A. et al., 2009, A&A, 495, 707

Chen Y., Reiprich T. H., Böhringer H., Ikebe Y., Zhang Y. Y., 2007, A&A, 466, 805

Chen Y.-C. et al., 2017, MNRAS, 466, 1880

Choque-Challapa N., Smith R., Candlish G., Peletier R., Shin J., 2019, MNRAS, 490, 3654

Chu A., Durret F., Márquez I., 2021, A&A, 649, A42

Chu A., Sarron F., Durret F., Márquez I., 2022, A&A, 666, A54

Cialone G., De Petris M., Sembolini F., Yepes G., Baldi A. S., Rasia E., 2018, MNRAS, 477, 139

Clowe D., Bradač M., Gonzalez A. H., Markevitch M., Randall S. W., Jones C., Zaritsky D., 2006, ApJ, 648, L109

Cohen S. A., Hickox R. C., Wegner G. A., Einasto M., Vennik J., 2014, ApJ, 783, 136

Conselice C. J., 2003, ApJS, 147, 1

Contreras-Santos A. et al., 2022, MNRAS, 511, 2897

Cortese L., Catinella B., Smith R., 2021, PASA, 38, e035

Cowie L. L., Songaila A., 1977, Nature, 266, 501

Crossett J. P. et al., 2022, A&A, 663, A2

Crossett J. P., Pimbblet K. A., Jones D. H., Brown M. J. I., Stott J. P., 2017, MNRAS, 464, 480

Dariush A., Khosroshahi H. G., Ponman T. J., Pearce F., Raychaudhury S., Hartley W., 2007, MNRAS, 382, 433

de Jong R. S. et al., 2019, The Messenger, 175, 3

De Luca F., De Petris M., Yepes G., Cui W., Knebe A., Rasia E., 2021, MNRAS, 504, 5383

De Lucia G., Weinmann S., Poggianti B. M., Aragón-Salamanca A., Zaritsky D., 2012, MNRAS, 423, 1277

di Nella H., Sylos Labini F., 1997, Astrophysical Letters and Communications, 36, 33

Diaferio A., 1999, MNRAS, 309, 610

Domainko W. et al., 2006, A&A, 452, 795

Dressler A., 1980, ApJ, 236, 351

Dressler A., Shectman S. A., 1988, AJ, 95, 985

Dreyer J., 1908, A New General Catalogue of Nebulae and Clusters of Stars: Being the Catalogue of the Late Sir John F.W. Herschel, Revised, Corrected, and Enlarged

Driver S. P., Liske J., Cross N. J. G., De Propris R., Allen P. D., 2005, MNRAS, 360, 81

Durret F., Chiche S., Lobo C., Jauzac M., 2021, A&A, 648, A63

Durret F., Perrot C., Lima Neto G. B., Adami C., Bertin E., Bagchi J., 2013, A&A, 560, A78

Dwarakanath K. S., Parekh V., Kale R., George L. T., 2018, MNRAS, 477, 957

Ebeling H., Edge A. C., Allen S. W., Crawford C. S., Fabian A. C., Huchra J. P., 2000, MNRAS, 318, 333

Ebeling H., Edge A. C., Bohringer H., Allen S. W., Crawford C. S., Fabian A. C., Voges W., Huchra J. P., 1998, MNRAS, 301, 881

Ebeling H., Kalita B. S., 2019, ApJ, 882, 127

Ebeling H., Stephenson L. N., Edge A. C., 2014, ApJ, 781, L40

Ebeling H., Voges W., Bohringer H., Edge A. C., Huchra J. P., Briel U. G., 1996, MNRAS, 281, 799

Einasto M. et al., 2010, A&A, 522, A92

Ettori S. et al., 2013, arXiv e-prints, arXiv:1306.2322

Fabian A. C., 2012, ARA&A, 50, 455

Fabricant D., Beers T. C., Geller M. J., Gorenstein P., Huchra J. P., Kurtz M. J., 1986, ApJ, 308, 530

Fasano G. et al., 2010, MNRAS, 404, 1490

Fasano G. et al., 2006, A&A, 445, 805

Fasano G. et al., 2015, MNRAS, 449, 3927

Fasano G. et al., 2012, MNRAS, 420, 926

Flin P., Krywult J., 2006, A&A, 450, 9

Fraknoi A., Morrison D., Wolff S., 2016, Astronomy, Open Textbook Library. OpenStax

Friedmann A., 1922, Zeitschrift fur Physik, 10, 377

Fujita Y., 1998, ApJ, 509, 587

Fujita Y., Goto T., 2004, PASJ, 56, 621

Fujita Y., Nagashima M., 1999, ApJ, 516, 619

Fumagalli M., Fossati M., Hau G. K. T., Gavazzi G., Bower R., Sun M., Boselli A., 2014, MNRAS, 445, 4335

Furusawa H. et al., 2018, PASJ, 70, S3

Gavazzi G., Boselli A., Mayer L., Iglesias-Paramo J., Vílchez J. M., Carrasco L., 2001, ApJ, 563, L23

Gebhardt K., Pryor C., Williams T. B., Hesser J. E., 1994, AJ, 107, 2067

Geller M. J., Beers T. C., 1982, PASP, 94, 421

Ghizzardi S., De Grandi S., Molendi S., 2013, Astronomische Nachrichten, 334, 422

Ghizzardi S., Rossetti M., Molendi S., 2010, A&A, 516, A32

Giovanelli R., Haynes M. P., 1985, ApJ, 292, 404

Gnedin O. Y., 2003, ApJ, 582, 141

Gozaliasl G. et al., 2014, A&A, 566, A140

Gregersen E., 2017, https://www.britannica.com/biography/Charles-Messier., Accessed: 2024-4-3

Gu L. et al., 2019, Nature Astronomy, 3, 838

Gullieuszik M. et al., 2023, ApJ, 945, 54

Gullieuszik M. et al., 2015, A&A, 581, A41

Gullieuszik M. et al., 2020, ApJ, 899, 13

Gunn J. E., Gott I., J. Richard, 1972, ApJ, 176, 1

Ha J.-H., Ryu D., Kang H., 2018, ApJ, 857, 26

Haines C. et al., 2023, The Messenger, 190, 31

Haines C. P. et al., 2015, ApJ, 806, 101

Hallman E. J., Markevitch M., 2004, ApJ, 610, L81

Hallman E. J., Skillman S. W., Jeltema T. E., Smith B. D., O'Shea B. W., Burns J. O., Norman M. L., 2010, ApJ, 725, 1053

Haynes M. P. et al., 2018, ApJ, 861, 49

Herschel J., Dreyer J., 2018, A Supplement to Sir John Herschel's General Catalogue of Nebulae and Clusters of Stars. Creative Media Partners, LLC

Hess K. M., Kotulla R., Chen H., Carignan C., Gallagher J. S., Jarrett T. H., Kraan-Korteweg R. C., 2022, A&A, 668, A184

Hou A., Parker L. C., Harris W. E., 2014, MNRAS, 442, 406

Hubble E. P., 1926, ApJ, 64, 321

Hubble E. P., 1936, Realm of the Nebulae

Hudson D. S., Mittal R., Reiprich T. H., Nulsen P. E. J., Andernach H., Sarazin C. L., 2010, A&A, 513, A37

Hwang H. S., Lee M. G., 2009, MNRAS, 397, 2111

Ichinohe Y., Werner N., Simionescu A., Allen S. W., Canning R. E. A., Ehlert S., Mernier F., Takahashi T., 2015, MNRAS, 448, 2971

Ignesti A., Gitti M., Brunetti G., O'Sullivan E., Sarazin C., Wong K., 2018, A&A, 610, A89

Ignesti A. et al., 2023, arXiv e-prints, arXiv:2305.19941

Ignesti A. et al., 2022, ApJ, 937, 58

Inoue S., Hayashida K., Ueda S., Nagino R., Tsunemi H., Koyama K., 2016, PASJ, 68, S23

Ivezić Ž. et al., 2019, ApJ, 873, 111

Jaffé Y. L. et al., 2018, MNRAS, 476, 4753

Jaffé Y. L., Poggianti B. M., Verheijen M. A. W., Deshev B. Z., van Gorkom J. H., 2013, MNRAS, 431, 2111

Jaffé Y. L., Smith R., Candlish G. N., Poggianti B. M., Sheen Y.-K., Verheijen M. A. W., 2015, MNRAS, 448, 1715

Jaffé Y. L. et al., 2016, MNRAS, 461, 1202

Jakiel R., 2019, The obsessive comet hunter, https://www.astronomy.com/science/the-obsessive-comet-hunter/., Accessed: 2024-4-4

Jeltema T. E., Hallman E. J., Burns J. O., Motl P. M., 2008, ApJ, 681, 167

Jin S. et al., 2023, MNRAS

Jones L. R., Ponman T. J., Horton A., Babul A., Ebeling H., Burke D. J., 2003, MNRAS, 343, 627

Kapferer W., Sluka C., Schindler S., Ferrari C., Ziegler B., 2009, A&A, 499, 87

Karp J. S. M., Lange J. U., Wechsler R. H., 2023, ApJ, 949, L13

Kass R. E., Wasserman L., 1995, Journal of the American Statistical Association, 90, 928

Katayama H., Hayashida K., Takahara F., Fujita Y., 2003, ApJ, 585, 687

Keel W. C., Kennicutt J., R. C., Hummel E., van der Hulst J. M., 1985, AJ, 90, 708

Kelkar K. et al., 2020, arXiv e-prints, arXiv:2002.08610

Kenney J. D. P., Koopmann R. A., 1999, AJ, 117, 181

Kennicutt J., R. C., 1983, ApJ, 272, 54

Kennicutt J., Robert C., Keel W. C., van der Hulst J. M., Hummel E., Roettiger K. A., 1987, AJ, 93, 1011

Knopp G. P., Henry J. P., Briel U. G., 1996, ApJ, 472, 125

Kolcu T., Crossett J. P., Bellhouse C., McGee S., 2022, MNRAS, 515, 5877

Komiyama Y. et al., 2018, PASJ, 70, S2

Koopmann R. A., Kenney J. D. P., 2004, ApJ, 613, 866

Kotecha S. et al., 2022, MNRAS, 512, 926

Kruskal W. H., Wallis W. A., 1952, Journal of the American Statistical Association, 47, 583

Kuchner U. et al., 2022, MNRAS, 510, 581

Kuutma T., Tamm A., Tempel E., 2017, A&A, 600, L6

Laganá T. F., Andrade-Santos F., Lima Neto G. B., 2010, A&A, 511, A15

Laganá T. F., Durret F., Lopes P. A. A., 2019, MNRAS, 484, 2807

Lakhchaura K., Singh K. P., Saikia D. J., Hunstead R. W., 2013, ApJ, 767, 91

Larson R. B., Tinsley B. M., Caldwell C. N., 1980, ApJ, 237, 692

Laudari S. et al., 2022, MNRAS, 509, 3938

Leavitt H. S., Pickering E. C., 1912, Harvard College Observatory Circular, 173, 1

Lemaître G., 1927, Annales de la Société Scientifique de Bruxelles, 47, 49

Lemaître G., 1931, Nature, 127, 706

Libeskind N. I. et al., 2018, MNRAS, 473, 1195

Liske J., Lemon D. J., Driver S. P., Cross N. J. G., Couch W. J., 2003, MNRAS, 344, 307

Lopes P. A. A., Ribeiro A. L. B., Brambila D., 2024, MNRAS, 527, L19

Lopes P. A. A., Trevisan M., Laganá T. F., Durret F., Ribeiro A. L. B., Rembold S. B., 2018, MNRAS, 478, 5473

Lourenço A. C. C. et al., 2023, MNRAS, 526, 4831

Lourenço A. C. C. et al., 2020, MNRAS, 498, 835

Luber N., van Gorkom J. H., Hess K. M., Pisano D. J., Fernández X., Momjian E., 2019, AJ, 157, 254

Ma C. J., Ebeling H., Marshall P., Schrabback T., 2010, MNRAS, 406, 121

Macario G., Markevitch M., Giacintucci S., Brunetti G., Venturi T., Murray S. S., 2011, ApJ, 728, 82

Machado R. E. G., Lima Neto G. B., 2013, MNRAS, 430, 3249

Mann A. W., Ebeling H., 2012, MNRAS, 420, 2120

Markevitch M. et al., 2000, ApJ, 541, 542

Markevitch M., Vikhlinin A., 2007, Phys. Rep., 443, 1

Martig M., Bournaud F., Teyssier R., Dekel A., 2009, ApJ, 707, 250

Martín-Navarro I., Pillepich A., Nelson D., Rodriguez-Gomez V., Donnari M., Hernquist L., Springel V., 2021, Nature, 594, 187

Martínez H. J., Muriel H., Coenda V., 2016, MNRAS, 455, 127

Mazzotta P., Fusco-Femiano R., Vikhlinin A., 2002, ApJ, 569, L31

McConnachie A. W., Venn K. A., Irwin M. J., Young L. M., Geehan J. J., 2007, ApJ, 671, L33

McGee S. L., Balogh M. L., Bower R. G., Font A. S., McCarthy I. G., 2009, MNRAS, 400, 937

McPartland C., Ebeling H., Roediger E., Blumenthal K., 2016, MNRAS, 455, 2994

Merloni A. et al., 2012, arXiv e-prints, arXiv:1209.3114

Merritt D., 1984, ApJ, 276, 26

Messier C., 1781, Catalogue des Nébuleuses et des Amas d'Étoiles (Catalog of Nebulae and Star Clusters), Connoissance des Temps ou des Mouvements Célestes, for 1784, p. 227-267

Messier C., Niles P., 1981, The Messier Catalogue of Charles Messier. Auriga

Mihos J. C., 2004, in Mulchaey J. S., Dressler A., Oemler A., eds, Clusters of Galaxies: Probes of Cosmological Structure and Galaxy Evolution, p. 277

Miller R. H., 1986, A&A, 167, 41

Mitsuishi I., Babazaki Y., Ota N., Sasaki S., Böhringer H., Chon G., Pratt G. W., 2018, PASJ, 70, 112

Miyazaki S. et al., 2018, PASJ, 70, S1

Mohr J. J., Fabricant D. G., Geller M. J., 1993, ApJ, 413, 492

Molendi S., Pizzolato F., 2001, ApJ, 560, 194

Monteiro-Oliveira R., Cypriano E. S., Machado R. E. G., Lima Neto G. B., Ribeiro A. L. B., Sodré L., Dupke R., 2017a, MNRAS, 466, 2614

Monteiro-Oliveira R., Doubrawa L., Machado R. E. G., Lima Neto G. B., Castejon M., Cypriano E. S., 2020, arXiv e-prints, arXiv:2004.13662

Monteiro-Oliveira R., Lima Neto G. B., Cypriano E. S., Machado R. E. G., Capelato H. V., Laganá T. F., Durret F., Bagchi J., 2017b, MNRAS, 468, 4566

Moore B., Katz N., Lake G., Dressler A., Oemler A., 1996, Nature, 379, 613

Moore B., Lake G., Katz N., 1998, ApJ, 495, 139

Moore B., Lake G., Quinn T., Stadel J., 1999, MNRAS, 304, 465

Moore S., 2015, Journal of the British Astronomical Association, 125, 173

Morell D. F., Ribeiro A. L. B., de Carvalho R. R., Rembold S. B., Lopes P. A. A., Costa A. P., 2020, MNRAS, 494, 3317

Moretti A. et al., 2017, A&A, 599, A81

Moretti A. et al., 2014, A&A, 564, A138

Müller A. et al., 2021, MNRAS, 508, 5326

Munari E., Biviano A., Borgani S., Murante G., Fabjan D., 2013, MNRAS, 430, 2638

Nakazawa K. et al., 2009, PASJ, 61, 339

Navarro J. F., Frenk C. S., White S. D. M., 1997, ApJ, 490, 493

Nelson D. et al., 2019, Computational Astrophysics and Cosmology, 6, 2

Niederste-Ostholt M., Strauss M. A., Dong F., Koester B. P., McKay T. A., 2010, MNRAS, 405, 2023

Nulsen P. E. J., 1982, MNRAS, 198, 1007

Okamoto T., Nagashima M., 2001, ApJ, 547, 109

Olave-Rojas D. E., Cerulo P., Araya-Araya P., Olave-Rojas D. A., 2023, MNRAS, 519, 4171

Oman K. A., Bahé Y. M., Healy J., Hess K. M., Hudson M. J., Verheijen M. A. W., 2021, MNRAS, 501, 5073

Owers M. S., Couch W. J., Nulsen P. E. J., Rand all S. W., 2012, ApJ, 750, L23

Owers M. S., Nulsen P. E. J., Couch W. J., Markevitch M., 2009, ApJ, 704, 1349

Paccagnella A. et al., 2017, ApJ, 838, 148

Pallero D., Gómez F. A., Padilla N. D., Bahé Y. M., Vega-Martínez C. A., Torres-Flores S., 2022, MNRAS, 511, 3210

Pallero D., Gómez F. A., Padilla N. D., Torres-Flores S., Demarco R., Cerulo P., Olave-Rojas D., 2019, MNRAS, 488, 847

Park S.-M., Chun K., Shin J., Jeong H., Lee J. H., Pak M., Smith R., Kim J.-W., 2023, ApJ, 954, 98

Peebles P. J. E., 1993, Principles of Physical Cosmology

Peng Y., Maiolino R., Cochrane R., 2015, Nature, 521, 192

Pisani A., 1993, MNRAS, 265, 706

Poggianti B. M., 1997, A&AS, 122, 399

Poggianti B. M. et al., 2016, AJ, 151, 78

Poggianti B. M. et al., 2019, MNRAS, 482, 4466

Poggianti B. M. et al., 2017a, Nature, 548, 304

Poggianti B. M. et al., 2017b, ApJ, 844, 48

Poole G. B., Fardal M. A., Babul A., McCarthy I. G., Quinn T., Wadsley J., 2006, MNRAS, 373, 881

Postman M. et al., 2012, ApJS, 199, 25

Press W. H., Schechter P., 1974, ApJ, 187, 425

Puglisi A. et al., 2021, Nature Astronomy, 5, 319

Quilis V., Moore B., Bower R., 2000, Science, 288, 1617

Ramella M. et al., 2007, A&A, 470, 39

Randall S. W., Clarke T. E., Nulsen P. E. J., Owers M. S., Sarazin C. L., Forman W. R., Murray S. S., 2010, ApJ, 722, 825

Raouf M., Smith R., Khosroshahi H. G., Dariush A. A., Driver S., Ko J., Hwang H. S., 2019, ApJ, 887, 264

Rasia E., Borgani S., Ettori S., Mazzotta P., Meneghetti M., 2013, ApJ, 776, 39

Rawle T. D. et al., 2014, MNRAS, 442, 196

Raychaudhury S., Fabian A. C., Edge A. C., Jones C., Forman W., 1991, MNRAS, 248, 101

Reid A. D., Hunstead R. W., Pierre M. M., 1998, MNRAS, 296, 531

Ribeiro A. L. B., de Carvalho R. R., Trevisan M., Capelato H. V., La Barbera F., Lopes P. A. A., Schilling A. C., 2013a, MNRAS, 434, 784

Ribeiro A. L. B., de Carvalho R. R., Trevisan M., Capelato H. V., La Barbera F., Lopes P. A. A., Schilling A. C., 2013b, MNRAS, 434, 784

Riseley C. J. et al., 2022, Monthly Notices of the Royal Astronomical Society, 515, 1871

Roberts I. D., Parker L. C., Hlavacek-Larrondo J., 2018, MNRAS, 475, 4704

Roberts I. D. et al., 2021a, A&A, 650, A111

Roberts I. D., van Weeren R. J., McGee S. L., Botteon A., Ignesti A., Rottgering H. J. A., 2021b, A&A, 652, A153

Roediger E., Brüggen M., Simionescu A., Böhringer H., Churazov E., Forman W. R., 2011, MNRAS, 413, 2057

Roediger E. et al., 2015a, ApJ, 806, 103

Roediger E. et al., 2015b, ApJ, 806, 104

Roettiger K., Burns J. O., Stone J. M., 1999, ApJ, 518, 603

Roman-Oliveira F. V., Chies-Santos A. L., Rodríguez del Pino B., Aragón-Salamanca A., Gray M. E., Bamford S. P., 2019, MNRAS, 484, 892

Rossetti M., Ghizzardi S., Molendi S., Finoguenov A., 2007, A&A, 463, 839

Rottgering H. J. A., Wieringa M. H., Hunstead R. W., Ekers R. D., 1997, MNRAS, 290, 577

Ruggiero R., Machado R. E. G., Roman-Oliveira F. V., Chies-Santos A. L., Lima Neto G. B., Doubrawa L., Rodríguez del Pino B., 2019, MNRAS, 484, 906

Salinas V. et al., 2024, MNRAS

Samuel J., Pardasani B., Wetzel A., Santistevan I., Boylan-Kolchin M., Moreno J., Faucher-Giguère C.-A., 2023, MNRAS, 525, 3849

Sanderson A. J. R., Edge A. C., Smith G. P., 2009, MNRAS, 398, 1698

Sarazin C. L., 2002, in Astrophysics and Space Science Library, Vol. 272, Feretti L., Gioia I. M., Giovannini G., eds, *Merging Processes in Galaxy Clusters*, p. 1

Sarazin C. L., Finoguenov A., Wik D. R., Clarke T. E., 2016, arXiv e-prints, arXiv:1606.07433

Sarkar A. et al., 2022, ApJ, 935, L23

Schneider P., 2007, Extragalactic Astronomy and Cosmology: An Introduction. Springer Berlin Heidelberg

Scrucca L., Fop M., Murphy T. B., Raftery A. E., 2016, The R Journal, 8, 289

Shapley H., Curtis H. D., 1921, Bulletin of the National Research Council, 2, 171

Sharov A., Novikov I., 1993, Edwin Hubble, The Discoverer of the Big Bang Universe. Cambridge University Press

Simionescu A., Werner N., Forman W. R., Miller E. D., Takei Y., Böhringer H., Churazov E., Nulsen P. E. J., 2010, MNRAS, 405, 91

Smith R., Calderón-Castillo P., Shin J., Raouf M., Ko J., 2022, AJ, 164, 95

Smith R. et al., 2023, MNRAS, 525, 4685

Smith R. J. et al., 2010, MNRAS, 408, 1417

Spitzer J., Lyman, Baade W., 1951, ApJ, 113, 413

Steyrleithner P., Hensler G., Boselli A., 2020, MNRAS, 494, 1114

Stott J. P., 2022, MNRAS, 511, 2659

Stoyan R., 2015, Dunlop S., ed, Great Comet of 1744. Cambridge University Press, p. 96–100

Stroe A. et al., 2015, MNRAS, 450, 646

Stroe A., Sobral D., Röttgering H. J. A., van Weeren R. J., 2014, MNRAS, 438, 1377

Sun M., Donahue M., Voit G. M., 2007, ApJ, 671, 190

Sun M., Jones C., Forman W., Nulsen P. E. J., Donahue M., Voit G. M., 2006, ApJ, 637, L81

Taylor J. E., Babul A., 2004, Monthly Notices of the Royal Astronomical Society, 348, 811

Tittley E. R., Henriksen M., 2005, ApJ, 618, 227

Urdampilleta I., Akamatsu H., Mernier F., Kaastra J. S., de Plaa J., Ohashi T., Ishisaki Y., Kawahara H., 2018, A&A, 618, A74

Vaezzadeh I. et al., 2022, MNRAS, 514, 518

Valluri M., 1993, ApJ, 408, 57

Valluri M., Jog C. J., 1990, ApJ, 357, 367

van Weeren R. J., de Gasperin F., Akamatsu H., Brüggen M., Feretti L., Kang H., Stroe A., Zandanel F., 2019, Space Sci. Rev., 215, 16

Varela J. et al., 2009, A&A, 497, 667

Venturi T., Bardelli S., Zambelli G., Morganti R., Hunstead R. W., 2001, MNRAS, 324, 1131

Venturi T., Rossetti M., Bardelli S., Giacintucci S., Dallacasa D., Cornacchia M., Kantharia N. G., 2013, A&A, 558, A146

Vijayaraghavan R., Ricker P. M., 2013, MNRAS, 435, 2713

Vikhlinin A., Markevitch M., Murray S. S., 2001, ApJ, 551, 160

Voller R., 2021, Hubble, Humason and the Big Bang: The Race to Uncover the Expanding Universe, Springer Praxis Books. Springer International Publishing

Vulcani B., Poggianti B. M., Finn R. A., Rudnick G., Desai V., Bamford S., 2010, ApJ, 710, L1

Vulcani B. et al., 2018, ApJ, 866, L25

Vulcani B., Poggianti B. M., Smith R., Moretti A., Jaffé Y. L., Gullieuszik M., Fritz J., Bellhouse C., 2022, ApJ, 927, 91

Walch S. K., Whitworth A. P., Bisbas T., Wünsch R., Hubber D., 2012, MNRAS, 427, 625

Walker S. A., Fabian A. C., Kosec P., 2014, MNRAS, 445, 3444

Walmsley M. et al., 2023, MNRAS, 526, 4768

Walmsley M. et al., 2022, MNRAS, 509, 3966

Wang J., Xu W., Lee B., Du M., Overzier R., Shao L., 2020, ApJ, 903, 103

Wang Y., Xu H., Gu L., Gu J., Qin Z., Wang J., Zhang Z., Wu X.-P., 2010, MNRAS, 403, 1909

West M. J., Oemler J., Augustus, Dekel A., 1988, ApJ, 327, 1

Wetzel A. R., Tinker J. L., Conroy C., van den Bosch F. C., 2013, MNRAS, 432, 336

Yagi M., Gu L., Koyama Y., Nakata F., Kodama T., Hattori T., Yoshida M., 2015, AJ, 149, 36

Yagi M., Komiyama Y., Yoshida M., Furusawa H., Kashikawa N., Koyama Y., Okamura S., 2007, ApJ, 660, 1209

Yagi M., Yoshida M., Gavazzi G., Komiyama Y., Kashikawa N., Okamura S., 2017, ApJ, 839, 65

Yu H., Diaferio A., Serra A. L., Baldi M., 2018, ApJ, 860, 118

Yuan Z. S., Han J. L., 2020, MNRAS, 497, 5485

Yuan Z. S., Han J. L., Wen Z. L., 2022, MNRAS, 513, 3013

Zabludoff A. I., Zaritsky D., 1995, ApJ, 447, L21

Zabludoff A. I., Zaritsky D., Lin H., Tucker D., Hashimoto Y., Shectman S. A., Oemler A., Kirshner R. P., 1996, ApJ, 466, 104

Zenteno A. et al., 2020, MNRAS, 495, 705

Zinger E., Dekel A., Birnboim Y., Nagai D., Lau E., Kravtsov A. V., 2018, MNRAS, 476, 56

ZuHone J. A., 2011, ApJ, 728, 54